-- Final Report --

January 20, 1989 to January 19, 1991

NEAR FIELD INTERACTION OF MICROWAVE SIGNALS WITH A BOUNDED PLASMA PLUME

Grant No. NCC3-127

Submitted to

Dr. Afroz Zaman
National Aeronautics and Space Administration
Lewis Research Center
Cleveland, OH 44135

Prepared by

H. Ling, G. A. Hallock, H. Kim and B. W. Birkner

Department of Electrical and Computer Engineering
The University of Texas at Austin
Austin, TX 78712-1084

January 1991

Table of Contents

1. PROJECT SUMMARY

PROJECT OVERVIEW:

The contract "Near Field Interaction of Microwave Signals with a Bounded Plasma Plume" (under Cooperative Agreement NCC3-127) was awarded to the University of Texas at Austin in January 1989. The objective of the project is to study the effect of the arcjet thruster plume on the performance of an on-board satellite reflector antenna. The total amount awarded, $50,000 + $50,000 = $100,000, covers the two-year period from January 20, 1989 to January 19, 1991.

Technical Monitor: Dr. Afroz Zaman
M.S. 54-8
NASA Lewis Research Center
21000 Brookpark Road
Cleveland, OH 44135
Tel: (216)-433-3415
FAX: (216)-433-6371

Principal Investigators: Dr. Hao Ling and Dr. Gary A. Hallock
Department of Electrical and Computer Engineering
The University of Texas at Austin
Austin, TX 78712-1084
Tel: (512)-471-1710 (H.L.)
(512)-471-4965 (G.A.H.)
FAX: (512)-471-5445

Other Investigators: Mr. Hyeongdong Kim and Mr. Bjorn Birkner
Graduate Students

This final report covers the two-year period from Janurary 20, 1989 to January 19, 1991, with special emphasis on the work performed during the second year.

PUBLICATIONS AND PRESENTATIONS

[1] H. Ling, G. A. Hallock, H. Kim and B. W. Birkner, "Near field interaction of microwave signals with a bounded plasma plume," Semiannual Report, NASA Grant NCC3-127, Aug. 1989.

[2] H. Ling, G. A. Hallock, H. Kim, B. W. Birkner and A. Zaman, "Reflector performance degradation due to an arcjet plume," 13th Allerton Symposium on Antenna Applications, Monticello, IL, 22 pp., Sept. 1989.

[3] B. W. Birkner, G. A. Hallock, H. Ling and H. Kim, "Satellite communication degradation from an arcjet plasma," poster paper, 31st Annual Meeting of the American Physical Society, Division of Plasma Physics, Nov. 1989 (Bulletin of the American Physical Society, vol. 34, No. 9, p. 2083, Oct. 1989).

[4] H. Kim and H. Ling, "Scattering by an inhomogeneous penetrable cylinder of arbitrary shape using ray tracing," National Radio Science Meeting, p. 71, Boulder, CO, Jan. 1990.

[5] H. Ling, G. A. Hallock, H. Kim and B. W. Birkner, "Near field interaction of microwave signals with a bounded plasma plume," Annual Report, NASA Grant NCC3-127, Jan. 1990.

[6] H. Ling, H. Kim, G. A. Hallock, B. W. Birkner and A. Zaman, "Effect of arcjet plume on satellite reflector performance," International IEEE AP-S Symposium, pp. 1876-1879, Dallas, TX, May 1990.

[7] B. W. Birkner, G. A. Hallock, H. Kim and H. Ling, "Arcjet plasma plume effect on a microwave reflector antenna," poster paper, 8th Topical Conference on High Temperature Plasma Diagnostics, May 1990.

[8] B. W. Birkner, "Modeling of a low-power arcjet thruster plasma plume for geometrical optics ray tracing," M.S. thesis, Univ. of Texas at Austin, August 1990.

[9] B. W. Birkner, G. A. Hallock, H. Kim and H. Ling, "Arcjet plasma plume effect on a microwave reflector antenna," *Rev. Sci. Instr.*, vol. 61, pp. 2978-2980, October 1990.

[10] H. Ling, H. Kim, G. A. Hallock, B. W. Birkner and A. Zaman, "Effect of arcjet plume on satellite reflector performance," submitted to *IEEE Trans. Antennas Propagat.*, January 1991.

[11] H. Kim and H. Ling, "High frequency electromagnetic scattering from an inhomogeneous dielectric object by ray tracing," to be presented at the International IEEE AP-S Symposium, Ontario, Canada, June 1991.

[12] H. Kim and H. Ling, "High frequency electromagnetic scattering from an inhomogeneous dielectric object by ray tracing," to be submitted to *IEEE Trans. Antennas Propagat.*

TRAVEL

(1) Drs. Ling and Hallock visited NASA Lewis Research Center on February 3, 1989 for a kick-off meeting on the project. They each presented an one-hour talk on the plasma modeling and antenna aspects of the project.

(2) Dr. Zaman visited the University of Texas at Austin on August 25, 1989 for an interim review of the project. She also toured the microwave and plasma fusion facilities.

(3) Drs. Ling and Hallock visited NASA Lewis Research Center on February 16, 1990 to report the progress and discuss future directions of the project.

(4) Drs. Ling and Hallock visited NASA Lewis Research Center on July 30, 1990 to report on the project and discuss the experimental aspects with Mr. Bjorn Birkner, who participated in the summer graduate student program.

FIRST-YEAR ACCOMPLISHMENTS

(1) Plasma modeling has been carried out. Electron density data supplied by NASA on the arcjet plume has been used for an in-depth modeling of the spatial plume profile as a function of arcjet power and mixture ratio. Spatial permittivity distribution of the plume based on the cold plasma model has been derived for the microwave propagation modeling.

(2) The finite temperature effect in the arcjet plume have been studied and found to be negligible for the range of operating conditions encountered in laboratory arcjets.

(3) A two-dimensional ray-tracing code for an arbitrary inhomogeneous plasma has been developed. It will calculate the ray path as well as the phase, amplitude and polarization of the associated ray optics field.

(4) The numerical results from the 2-D ray tracing algorithm have been compared to exact solutions available for several special media, e.g., Maxwell's fisheye and a quadratically varying ionosphere. Good agreement is obtained given enough precision in the numerical calculations.

(5) A two-dimensional reflector pattern computation code has been implemented. A ray-tube integration scheme is used to calculate the far field from the ray optics field transmitted through the plume. The far field performance degradation of reflectors in the presence of the plume has been calculated in 2-D. It is found that in addition to gain loss, beam broadening and sidelobe deterioration, a significant beam squint can occur due to refraction of ray paths in the plume.

(6) In order to determine the lower frequency bound of validity of the ray approach, the scattering of a plane wave by an inhomogeneous circular cylinder was formulated using ray optics. The ray results were compared to (i) a special medium where the exact solution to this problem exists, and (ii) a layered cylinder model where again the exact solution can be found. The agreement between the ray results and the exact solutions is excellent when the cylinder radius is above 3 free-space wavelengths.

(7) A three-dimensional ray-tracing code has being developed. The 3-D calculation of field amplitude is significantly more complicated than the 2-D version. In addition, the rotation of the polarization vector due to the non-planar nature of the ray path is properly taken into account. Preliminary results of the 3-D implementation have been verified by the exact results available in Maxwell's fisheye.

(8) A three-dimensional reflector pattern computation code has been implemented. A ray-tube integration scheme is used to calculate the far field from the ray optics field transmitted through the plume. The far field performance degradation of reflectors in the presence of the plume has been calculated in 3-D. Reflector performance degradation such as beam squint, beam broadening, sidelobe deterioration and cross polarization can be evaluated quantitatively.

(9) Plans for possible experimental validation of the numerical modeling has been initiated. Both near field and far field measurement setups are under investigation. We are also looking into using microwave interferometer for non-invasive plume diagnostics.

SECOND-YEAR ACCOMPLISHMENTS

(1) Collisional effects in the arcjet plasma which can result in wave attenuation were investigated. They were found to be negligible for the range of operating conditions encountered in the laboratory arcjet plume.

(2) Using the ray modeling codes developed in the first year, 3-D reflector performance degradation information such as gain loss, pointing error, sidelobe levels and cross polarization have been tabulated for different plume-to-reflector configurations. It was found that the plume effect on the reflector performance is strongly dependent on the position of the reflector with respect to the arcjet thruster.

(3) Plans for experimental validation of the numerical ray modeling were initiated at the end of the first year. It was decided that reflector far-field measurements would be diffcult to realize in the laboratory, especially in view of the vacuum environment necessary for arcjet operation. A near-field experiment has therefore been further pursued. Since the plume effect is expected to be small, wall reflection inside the vacuum facility is an important consideration. Vacuum compatible absorbers were considered for damping out wall reflections. (Several sheets of Eccosorb FDS were purchased for testing.) In addition, the software time-gating feature of the HP8510 network analyzer was extensively investigated. By making measurements over a broad frequency range and Fourier transforming to the time domain, software gating can be applied in the time domain to eliminate the reflection signals. Measurements of a dielectric (paraffin) lens were made in the laboratory and the results demonstrated that this concept can be applied with good accuracy.

(4) Our graduate student, Bjorn Birkner, participated in the NASA summer program. He interacted closely with both the propulsion group and the antenna group and utilized the in-house facility at NASA to set up microwave experiments similar to those performed at Texas. The feasibility of the plume/reflector near-field experiment using NASA's vacuum facility was further investigated. Measurement accuracy and aliasing errors from the software time-gating concept were also considered in more detail. At the end of the summer, he assisted Dr. Zaman in putting together a detailed cost estimate of carrying out the experiment.

(5) Further development in the ray modeling code has been carried out, with the aim of supporting the experimental effort. First, the 3-D near-field calculation has been implemented, in order to simulated the experimental setup. Next, the variable step size feature in the ray tracing routines was implemented to improve the efficiency of the ray code. This capability would allow larger reflectors to be modeled. Finally, the effect of a sharp plume boundary has been investigated in order to (i) simulate experiments carried out in a non-vacuum environment, such as measuring the scattering pattern from a dielectric lens, and (ii) model sharp plume boundaries which may occur in high power arcjets. Preliminary results showed good agreement when compared with exact solutions for simple scatterers.

(6) In parallel with the experimental effort, an independent validation of the 3-D ray tracing code has been carried out. The scattering from an inhomogeneous sphere was considered. The series expansion solution to the scattering from a multi-layered sphere was implemented to approximate the exact solution to the problem. The agreement between the ray results and the reference solution is quite good when the sphere diameter is above 6 wavelengths, especially in the forward scattering region. This confirms the validity of the ray calculation and further supports our earlier results on the reflector performance prediction.

CONCLUSIONS AND RECOMMENDATIONS

(1) From measurement data and theoretical calculations made on the arcjet plasma, we find that higher order effects such as anisotropy due to the earth's magnetic field, finite plasma temperature and attenuation due to collisions are small for low-power arcjets (~ 1 kW). A simple collisionless cold plasma model should be adequate in describing the plume plasma.

(2) Electromagnetic modeling using the approximate ray theory has been verified against various exact solutions for both two- and three-dimensional scatterers. We find that the ray theory is accurate as long as the size of the plume scatterer is on the order of 5 wavelengths or greater. The accuracy of the ray theory is particularly good in the forward scattering region (i.e., the transmitted field through the plume). In the reflector antenna study, we are mainly interested in this region.

(3) The far-field patterns of the reflector in the presence of the plume have been computed for different reflector-to-plume configurations and the resulting performance degradation have been tabulated. As the arcjet power is increased, a gradual degradation of the reflector pattern is observed. The most significant and interesting effect is a beam squinting phenomenon where the antenna mainbeam tends to tilt away from the plume region. Associated with this phenomenon are antenna gain loss and pointing error. The amount of degradation in the antenna performance is also found to be strongly dependent on the specific plume-to-reflector configuration. Finally, for low-power arcjets in the 1-kW class, the plume effect on the antenna performance is almost negligible.

(4) Experimental verification of the results predicted by the ray theory may be difficult and costly. A near-field measurement performed inside a vacuum facility is probably the most feasible option, as oppose to carrying out a far field test. Since an anechoic vacuum chamber is difficult to achieve, additional signal processing techniques such as time-gating are needed to prevent wall reflections from contaminating the measurement.

(5) The computer modeling capabilities developed in this work can be applied to predict the plume impact on microwave links in more realistic antenna and arcjet configurations, such as those found on the AT&T TELSTAR-4 communication satellite.

2 Plasma Modeling

As a medium for the propagation of electromagnetic waves, a plasma is refractive, lossy, dispersive, nonlinear, and inhomogeneous (and additionally resonant, anisotropic, and non-reciprocal if magnetized).

2.1 Wave Propagation

Wave propagation is governed by Maxwell's equations. Combining Ampere's and Faraday's laws yields the wave equation

$$\nabla \times (\nabla \times \vec{E}) + \frac{\partial}{\partial t}(\mu_0 \vec{J} + \epsilon_0 \mu_0 \frac{\partial \vec{E}}{\partial t}) = 0$$

Assuming:

1. Linearity (wave fields sufficiently small so current is a linear function of electric field)

2. Medium is homogeneous in space and time

can Fourier analyze the fields and currents

$$\vec{E}(\vec{x}, t) = \int \vec{E}(\vec{k}, \omega) e^{i(\vec{k} \cdot \vec{x} - \omega t)} d^3\vec{k} d\omega$$

and write an Ohm's law expression for each Fourier mode

$$\vec{J}(\vec{k}, \omega) = \bar{\sigma}(\vec{k}, \omega) \cdot \vec{E}(\vec{k}, \omega)$$

where $\bar{\sigma}$ is the conductivity tensor.

The plasma does not satisfy the spatial uniformity assumption. However, if gradients are sufficiently small then locally the above analysis can be applied. An eikonel or geometrical optics approximation can be used.

For a single Fourier mode the wave equation yields

$$\vec{k} \times (\vec{k} \times \vec{E}) + i\omega(\mu_0 \bar{\sigma} \cdot \vec{E} - \epsilon_0 \mu_0 i\omega \vec{E}) = 0$$

$$(\vec{k}\vec{k} - k^2 I + \omega^2 \mu_0 \bar{\epsilon}) \cdot \vec{E} = 0$$

where I is the unit dyad and $\bar{\epsilon}$ the dielectric tensor

$$\bar{\epsilon} = (\epsilon_0 I + \frac{i}{\omega} \bar{\sigma})$$

The plasma properties may be equivalently specified by $\bar{\epsilon}$ or $\bar{\sigma}$. For a nontrivial solution for $\vec{E}$

$$det(\vec{k}\vec{k} - k^2 I + \omega^2 \mu_0 \bar{\epsilon}) = 0$$

which is the dispersion relation, relating $\vec{k}$ and ω for different waves. Its solution also gives the wave polarization.

If the plasma is not immersed in a magnetic field it can usually be treated as an isotropic medium. Then

$$\bar{\sigma} = \sigma I$$

$$\bar{\epsilon} = \epsilon I$$

where σ and ϵ are the scalar conductivity and permittivity. The determinant reduces to

$$det(\vec{k}\vec{k} - k^2 I + \omega^2 \mu_0 \bar{\epsilon}) = (-k^2 + \omega^2 \mu_0 \epsilon)^2 (\omega^2 \mu_0 \epsilon)$$

which is equal to zero if

$$\omega^2 \mu_0 \epsilon - k^2 = 0$$

or

$$\omega^2 \mu_0 \epsilon = 0$$

The first equation represents a solution with transverse polarization of the electric field ($\vec{k} \cdot \vec{E} = 0$) while the second is a longitudinal solution ($\vec{k} \times \vec{E} = 0$).

The transverse solution

$$k = \frac{\omega}{c} \sqrt{\epsilon_r}$$

can be expressed in terms of the index of refraction of the medium ($v_p = \omega/k$)

$$N = \frac{c}{v_p} = \sqrt{\epsilon_r}$$

and is of interest here.

The longitudinal wave dispersion relation is $\epsilon = 0$, which can have a nontrivial solution in a plasma.

2.2 Plasma Analysis

We consider an infinite, uniform, unmagnetized Lorentz plasma. The Lorentz model assumes

1. Electrons interact with each other only through collective spacecharge forces.
2. Ions and neutrals can be regarded as a continuous stationary fluid through which the electrons move with viscous friction

We analyze the motion of individual representative particles, ignoring the statistical correlations in the electrons position and velocity.

In addition, we ignore thermal particle motion ($T_e = T_i = 0$), which is valid when $v_{th} \ll c$ and $v_p \sim c$ (cold plasma). We therefore assume the only particle motion comes from the wave fields. This is governed by the Lorentz equation.

2.2.1 Collisionless Model

The electron motion is given by

$$m\frac{d\vec{v}}{dt} = q(\vec{E} + \vec{v} \times \vec{B})$$

The wave fields are related by

$$\frac{E}{H} = \sqrt{\frac{\mu_0}{\epsilon}}$$

which gives

$$\frac{F_E}{F_B} = \frac{qE}{qvB} = \frac{v_p}{v} \sim \frac{c}{v}$$

Therefore the wave's magnetic force on the plasma can be neglected, and the Lorentz equation reduces to

$$m\frac{d\vec{v}}{dt} = q\vec{E}$$

In the Fourier analysis $\vec{v}$ is harmonic

$$-i\omega m\vec{v} = q\vec{E}$$

$$\vec{v} = \frac{qi}{\omega m}\vec{E}$$

The current density is given by

$$\vec{J} = qn\vec{v}$$

$$\vec{J} = \frac{e^2 ni}{\omega m_e}\vec{E}$$

which gives the plasma conductivity ($\vec{J} = \sigma\vec{E}$)

$$\sigma = \frac{e^2 ni}{\omega m_e}$$

and permittivity

$$\epsilon = \epsilon_0 + \frac{i}{\omega}\sigma$$

$$\epsilon = \epsilon_0 - \frac{e^2 n}{\omega^2 m_e}$$

Defining the plasma frequency

$$\omega_p^2 = \omega_e^2 + \omega_i^2 \sim \omega_e^2 = \frac{n_e e^2}{\epsilon_0 m_e}$$

yields the cold plasma permittivity

$$\epsilon = \epsilon_0(1 - \frac{\omega_p^2}{\omega^2})$$

and the dispersion relation

$$k = \frac{\omega}{c}\sqrt{1 - \frac{\omega_p^2}{\omega^2}}$$

2.2.2 Collisional Model

The influence of discrete positive ions and neutral molecules in a plasma can be represented to good approximation by including a viscous damping term, proportional to velocity, in the electron equation of motion

$$m\frac{d\vec{v}}{dt} = -e\vec{E} - \nu m\vec{v}$$

With Fourier analysis this yields

$$\vec{v} = \frac{-e}{m(\nu - i\omega)}\vec{E}$$

Using $\vec{J} = -en\vec{v} = \sigma\vec{E}$ gives

$$\sigma = \frac{e^2 n}{m(\nu - i\omega)}$$

The permittivity is given by

$$\epsilon = \epsilon_0 + \frac{i}{\omega}\sigma$$

which gives

$$\epsilon_r = 1 - \frac{\omega_p^2}{\omega(i\nu + \omega)}$$

or

$$\epsilon_r = (1 - \frac{\omega_p^2}{\nu^2 + \omega^2}) + i(\frac{\nu\omega_p^2}{\omega(\nu^2 + \omega^2)})$$

Now using

$$k = \frac{\omega}{c}\sqrt{\epsilon_r} = \beta + i\alpha$$

gives the collisional dispersion relation

$$k = \frac{\omega}{c}\sqrt{1 - \frac{\omega_p^2}{\nu^2 + \omega^2} + i\frac{\nu\omega_p^2}{\omega(\nu^2 + \omega^2)}}$$

Three frequency regimes can be identified:

1. Low frequencies $\omega < \nu$. The high plasma conductivity for DC and low frequency fields is obtained.

2. Intermediate frequencies $\nu < \omega < \omega_p$. Here the plasma will not propagate an EM wave, similar to a waveguide in cutoff. The wave penetration is the order of the wavelength of a free space wave at the plasma frequency.

3. High frequencies $\omega > \omega_p$. The plasma is a relatively low-loss dielectric. This is the regime of interest.

For the high frequency regime, using

$$\nu^2 + \omega^2 \sim \omega^2$$

$$\sqrt{1+x} \sim 1 + \frac{x}{2}$$

yields

$$k \sim \frac{\omega}{c}\sqrt{1 - \frac{\omega_p^2}{\omega^2}}\left(1 + \frac{i\nu\omega_p^2}{2\omega^3(1-\omega_p^2/\omega^2)}\right)$$

and therefore

$$\beta \sim \frac{\omega}{c}\sqrt{1 - \frac{\omega_p^2}{\omega^2}}$$

$$\alpha \sim \frac{\omega}{c}\left(1 - \frac{\omega_p^2}{\omega^2}\right)^{-1/2}\frac{\nu\omega_p^2}{2\omega^3}$$

The real refractive index is quite insensitive to collisional damping. The attenuation is small except near the plasma frequency.

2.2.3 Collisions

For a partially ionized gas

$$\nu_{total} = \nu_{en} + \nu_{ei}$$

where ν_{en} is the electron-neutral collision frequency and ν_{ei} is the electron-ion collision frequency.

The degree of ionization above which Coulomb collisions dominate is strongly temperature dependent. At $T_e \sim 0.1\,eV$ the critical ionization is small, the order of $10^{-5} - 10^{-6}$. The arcjet operates with $n_e \sim 5 \times 10^{-4} n_n$ and T_e from 0.1 to 0.3 eV (Carney NASA TM 102284).

For a Maxwellian velocity distribution

$$\nu_{ei} = 8.4 \times 10^{-5} \frac{n_e}{(T_e)^{3/2}}\ s^{-1}$$

with n in cm^{-3} and T_e in eV. For $n_e = 10^{10}\,cm^{-3}$ and $T_e = 0.1\,eV$

$$\nu_{ei} = 2.7 \times 10^7\ s^{-1}$$

The collision frequency for the scattering of charged particles of species α by neutrals is

$$\nu_{\alpha n} = n_n \sigma_{\alpha n} \sqrt{\frac{kT_\alpha}{m_\alpha}} \; s^{-1}$$

where n_n is the neutral density and $\sigma_{\alpha n}$ is the cross section, typically $\sim 5 \times 10^{-15} cm^2$ and weakly dependent on temperature. For electrons

$$\nu_{en} = 2.1 \times 10^{-7} n_n \sqrt{T_e} \; s^{-1}$$

with n_n in cm^{-3} and T_e in eV. For $n_n = 2 \times 10^{13} \; cm^{-3}$ and $T_e = 0.3 \; eV$

$$\nu_{en} = 2.3 \times 10^6 \; s^{-1}$$

These calculations are consistent with Carney's mean free path estimates

$$\lambda_{ei} = 3 - 200 \; cm$$

$$\lambda_{en} = 20 - 4000 \; cm$$

Using

$$\nu = n \sigma \bar{v} = \frac{\bar{v}}{\lambda}$$

and

$$\bar{v} = \sqrt{\frac{8kT_e}{\pi m_e}}$$

$$\bar{v}(T_e = 0.1 \; eV) = 2.1 \times 10^7 \; cm/s$$

$$\bar{v}(T_e = 0.3 \; eV) = 3.7 \times 10^7 \; cm/s$$

gives

$$1.1 \times 10^5 \; < \; \nu_{ei} \; < \; 7 \times 10^6 \; s^{-1}$$

$$9.3 \times 10^3 \; < \; \nu_{en} \; < \; 1.9 \times 10^6 \; s^{-1}$$

2.2.4 Attenuation

Using the following parameters

$$n = 10^{10}\ cm^{-3} \Rightarrow \omega_p = 5.65 \times 10^9\ s^{-1}$$

$$\nu = 3 \times 10^7\ s^{-1}$$

in

$$\alpha \sim \frac{\omega}{c}\left(1 - \frac{\omega_p^2}{\omega^2}\right)^{-1/2} \frac{\nu\omega_p^2}{2\omega^3}$$

yields, for $\omega = 1.2\omega_p$, attenuation and skin depth

$$\alpha = 0.0628\ m^{-1}$$

$$\delta = \frac{1}{\alpha} = 15.9\ m$$

For $\omega = 1.5\omega_p$ the results are

$$\alpha = 0.0298\ m^{-1}$$

$$\delta = \frac{1}{\alpha} = 33.6\ m$$

and for $\omega = 5\omega_p$

$$\alpha = 0.00203\ m^{-1}$$

$$\delta = \frac{1}{\alpha} = 492\ m$$

Conclusions:

1. The attenuation is small for the low power arcjet, even close to the plasma frequency.
2. Attenuation could be a factor in signal degradation in higher power arcjets if ν increases about an order of magnitude. This will depend on how the plasma density and temperature scales.
3. These results can be incorporated into our ray-tracing codes. A perturbation technique is most appropriate, where the ray trajectory is unchanged (the collisional β is unchanged from the collisionless model) but the attenuation α is carried along giving exponential attenuation of the ray amplitude.

2.3 Plume Electron Density Model

1. We have modeled the plume profile as a function of space and arcjet power, based on Carney's experimental measurements and motivated by NASA modeling.

2. We have initially used a simple model allowing linear optimization: $n_e = A_1 exp(-\alpha\theta)/r^2$.

3. We have also evaluated Reynold's model using nonlinear optimization: $n_e = A_0 exp\{-[\lambda(1-\cos(\theta)]^N\}/z^2$.

4. Future work will include modeling other functions to the experimental data, to eliminate the on-axis discontinuity and test the ray-tracing code sensitivity to the model details.

5. Our modeling programs allow optimization of almost any function with the experimental data available. The code provides the least squared error for comparison.

6. We have also modeled the arcjet power dependence, based on the experimental data: $n_e = n_e(P = 1025\ W)K_P exp(\beta_P P)$.

7. The work has been done on a DEC microVAX workstation, using IMSL math routines and IDL processing/plotting software.

8. The output of this modeling is the input to the ray-tracing codes. We have also used the microVAX capabilities for interactive 3-d display of the ray-tracing code output.

Figures 1 - 5 illustrate this work. The analysis is described in detail in Publication 8 (B. W. Birkner M.S. Thesis).

SPATIAL SURFACE FIT TO DATA

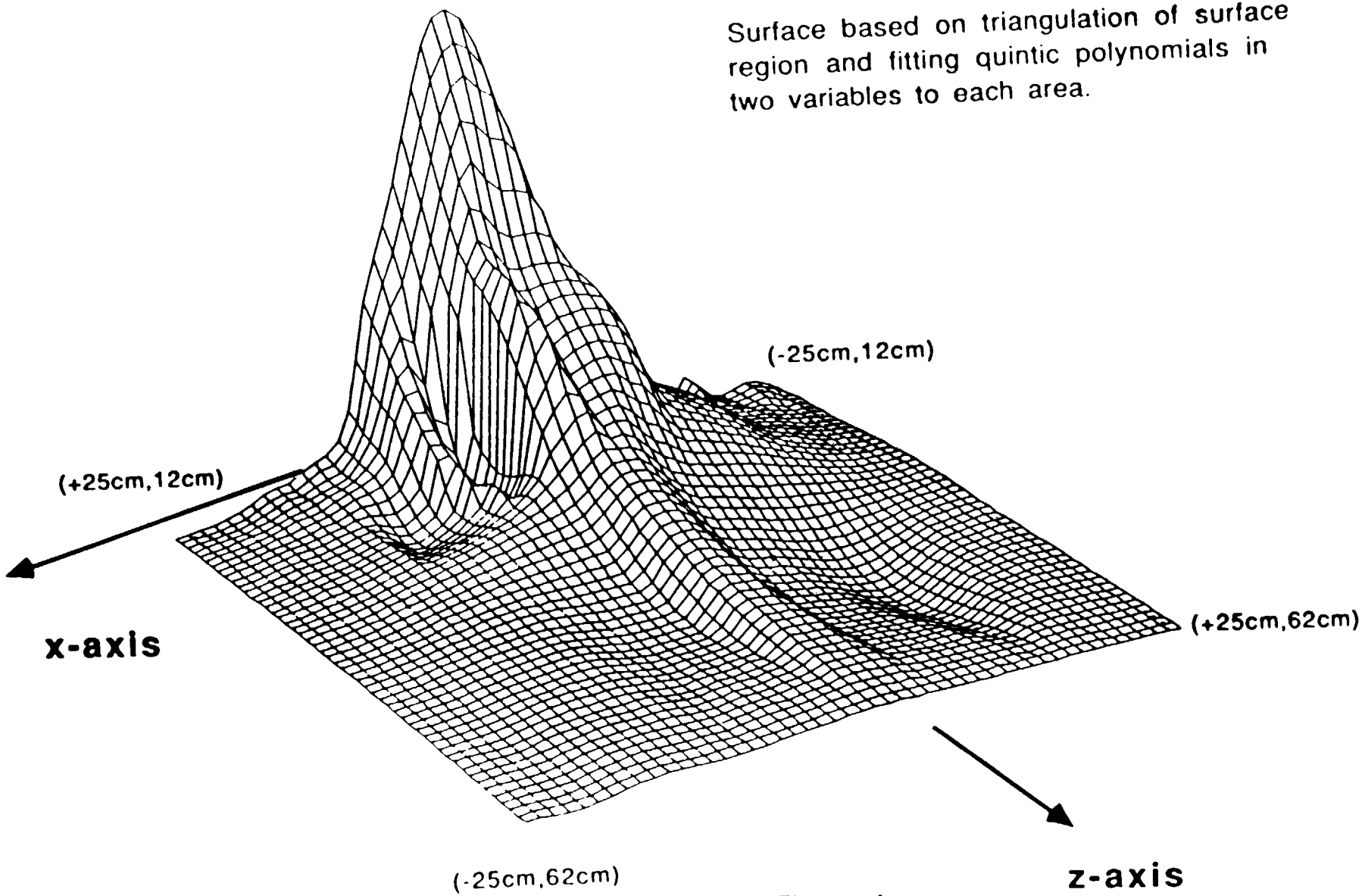

Figure 1

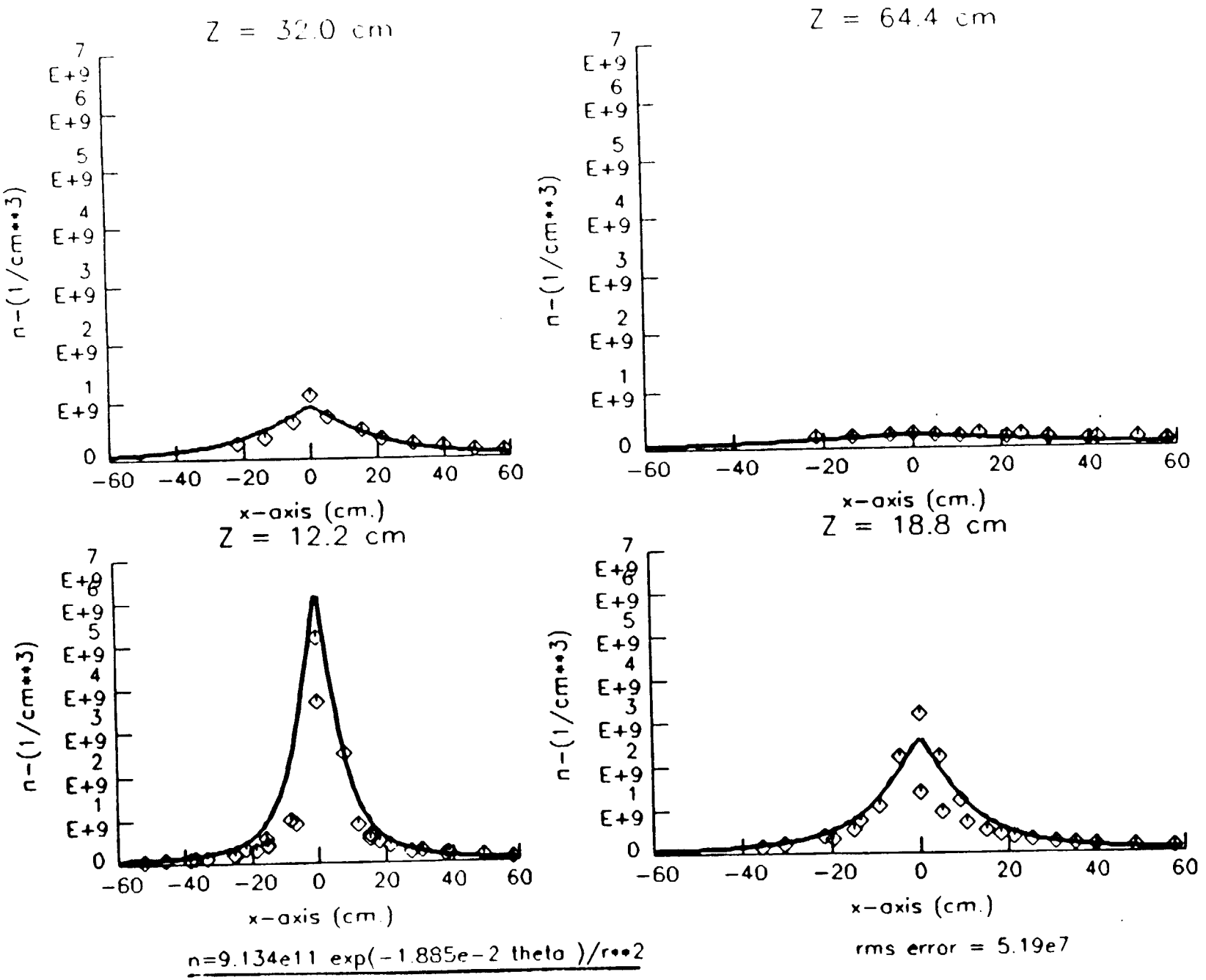
Z = 32.0 cm
Z = 64.4 cm
Z = 12.2 cm
Z = 18.8 cm
n-(1/cm**3)
x-axis (cm.)
7 E+9
6 E+9
5 E+9
4 E+9
3 E+9
2 E+9
1 E+9
0
-60 -40 -20 0 20 40 60
n=9.134e11 exp(-1.885e-2 theta)/r**2
rms error = 5.19e7

Figure 2

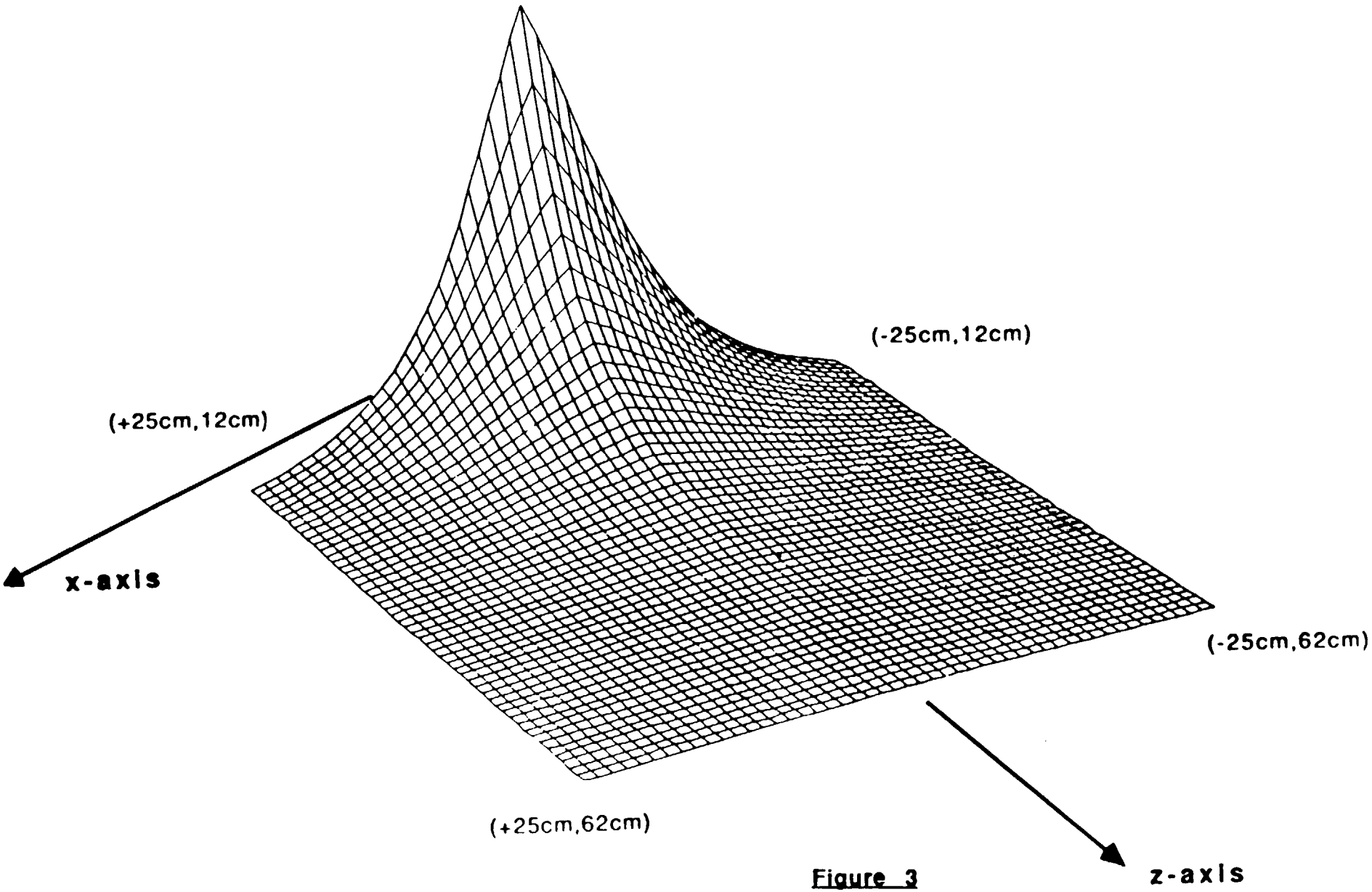
LEAST SQUARES FIT TO SPATIAL DATA
(-25cm,12cm)
(+25cm,12cm)
x-axis
(-25cm,62cm)
(+25cm,62cm)
z-axis

Figure 3

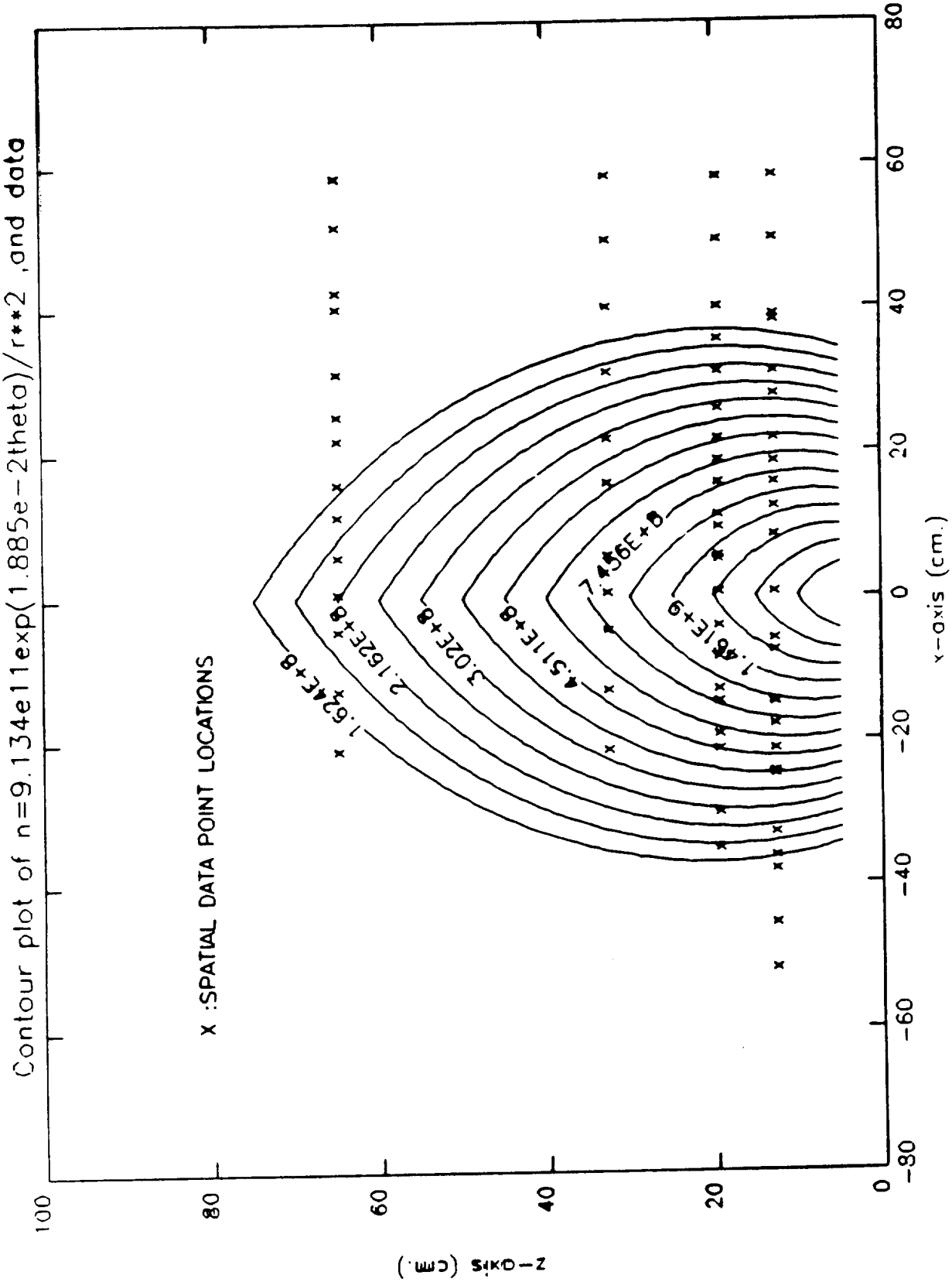
Contour plot of n=9.134e11exp(1.885e-2theta)/r**2 ,and data
X :SPATIAL DATA POINT LOCATIONS
1.624E+8
2.162E+8
3.02E+8
4.511E+8
7.456E+8
1.48E+9
Z-axis (cm.)
X-axis (cm.)
100
80
60
40
20
0
-80
-60
-40
-20
0
20
40
60
80

Figure 4

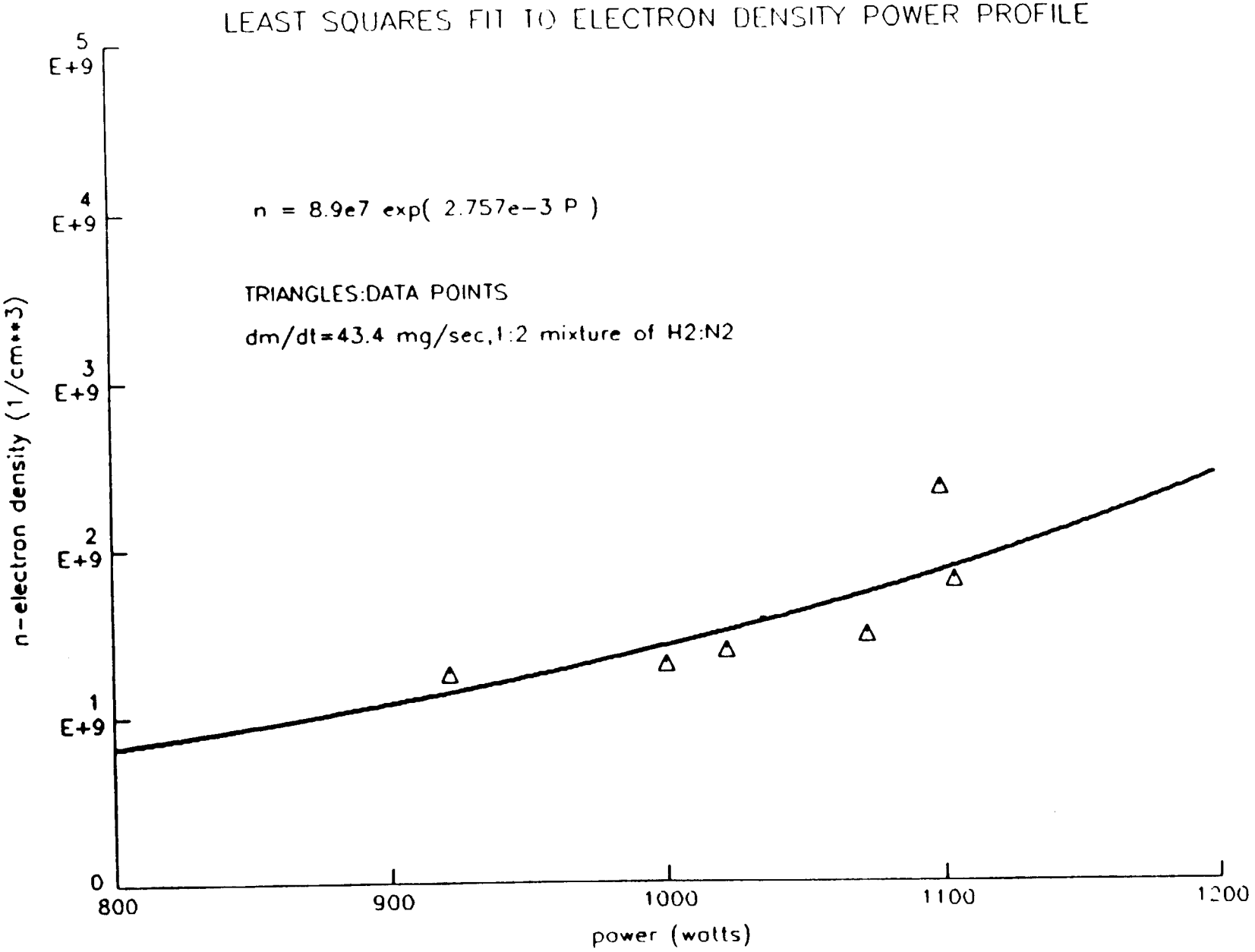

Figure 5

2.4 Proposed Experimental Program

1. Experimental verification of our present results is a logical next step in our program. This should be done in parallel with configuration studies and advanced modeling/code development.

2. Experimental verification is very important because the geometrical optics assumptions which underlie the ray-tracing methods may not be well satisfied by the plasma plume.

3. In addition, it appears that the equipment and experimental setup used for code validation could be used as a microwave interferometer for plume electron density measurements.

2.4.1 Near-Field Measurements

1. The issue for satellite communications is the plume effect on the far-field antenna radiation pattern.

2. Far-field measurements are difficult to simulate in the laboratory, however, with the plume vacuum requirements. A far-field experiment might be possible in the 19 m NASA, tank, but would require dedicated use of the tank and would only allow limited angular measurements.

3. Therefore a near-field experiment seems more appropriate. It will require much less space, and allow measurements over the entire antenna pattern.

4. A near field experiment is also a very sensitive test of our code. If our near-field calculations are verified correct then our far-field calculations are very accurate.

5. We propose a near field experiment be undertaken during the summer of 1990. One of our graduate students, Bjorn Birkner, will work on-site at NASA Lewis. We would hope equipment costs can be kept low by making use of microwave components available at NASA Lewis and UT Austin.

2.4.2 Electron Density Measurements

1. Experimental measurements of the plasma electron density are important for optimizing arcjet performance. The profile is also a fundamental parameter in our communication degradation studies.

2. It appears that the experimental apparatus required for code verification can also be used for microwave interferometry. Additional components required are:

(a) Two microwave lenses to focus the antenna radiation and provide spatial resolution.

(b) Microwave hardware (waveguide, beamsplitters, etc.) to configure the system as a Mach-Zehnder interferometer.

(c) A mounting structure (or beam steering capabilities) to allow positioning the beam with respect to the plasma.

2.4.3 Comparison of Interferometry with Probe Measurements

ADVANTAGES:

1. It is completely non-invasive.
2. It can be applied to higher power arcjets (and in fact will work better). Langmuir probes will be restricted to the edge region of high power thrusters.
3. It can provide measurements close to the thruster nozzle (Langmuir probes appear to be limited to about 12 cm). Data near the arcjet nozzle are needed to understand plume anomalies (n_e increases with increased flow rate; expect more recombination, etc.).
4. It might be capable of resolving probe measurement uncertainties, due to unknown factors such as the "wetted" current collection area.
5. Cross-section or even full 3-D profiles can be made in a short time.
6. It has a fast time response (typically sub-millisecond) for transient measurements.
7. It has high noise immunity (excellent environmental isolation). The system should operate well in pulsed ignition experiments, for example.

DISADVANTAGES:

1. The measurement is inherently chord-integrated and requires Abel or tomographic inversion. Langmuir probes provide a highly localized measurement.
2. Application of interferometry to low power ($\sim 1\ KW$) arcjets appears feasible, but nontrivial. It is near the lower limit of plasma size $\times$ density needed for the measurement. However, all aspects should improve as the arcjet program evolves to higher power thrusters.
3. Interferometry is more complex and costly than probe measurements.

2.4.4 Proposed Arcjet Interferometer

CONSTRAINTS:

1. To avoid dissipative and nonlinear effects the operating frequency should be several times the plasma frequency.
2. The probing wavelength should be small compared to the plasma diameter, to minimize refractive effects.
3. The probing beam should be small compared to the plasma size, to provide good spatial resolution.
4. The operating frequency must not be too far above the plasma frequency or the phase shift will be too small to measure.

INITIAL DESIGN:

1. 10 GHz operating frequency (The plasma frequency is $\sim$ 1 GHz for $n_e = 10^{10}\ cm^{-3}$.
2. Obtain a phase shift of $\sim$ 10 degrees for a 20 cm chord-integrated average density of $10^{10}\ cm^{-3}$.
3. Spatial resolution will be the order of 3 cm, the beam wavelength. This is 15 % of a 20 cm plume diameter.
4. A heterodyne configuration is being evaluated.

A block diagram of the proposed interferometer is shown in Fig. 6.

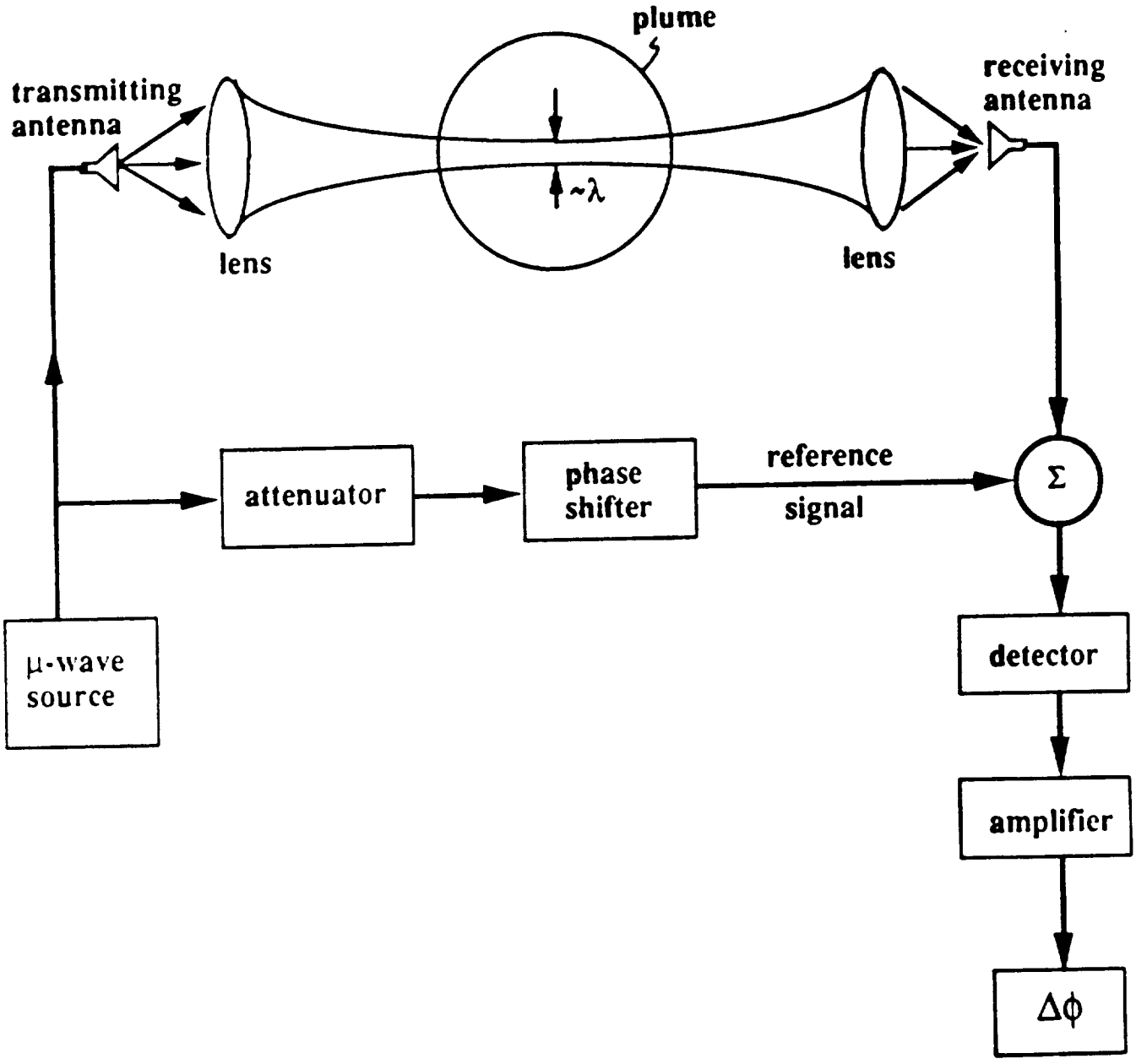

Figure 6 Microwave Interferometer for Plasma Density Measurements.

3. ELECTROMAGNETIC MODELING

3.1. New Developments in Ray Code

Emphasis: Support experimental effort

1. 3-D Near Field Calculation
2. Modeling Scatterer Boundary
3. Variable Step Size Ray Tracing

1. 3-D Near Field Calculation

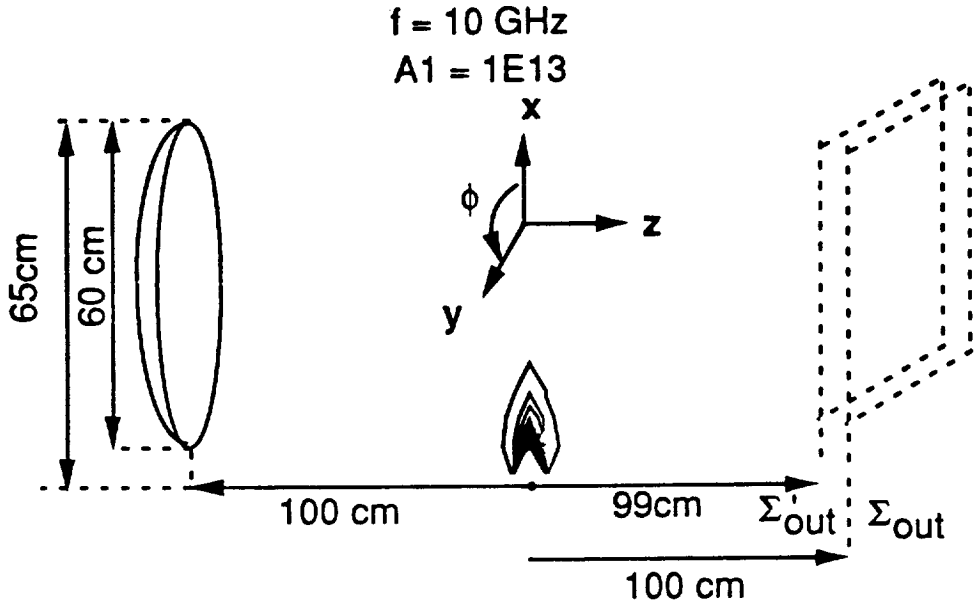

Approach:

- Launch a uniformly spaced set of rays from source antenna.
- Obtain a set of non-uniformly spaced exit rays on the Σ' out.
- Use "near-field" ray tube integration to calculate the field distribution on Σ out

Near-field ray tube integration:

$$\vec{E}(\vec{r}) = \int_{\text{Ray tube}} dS' \{ i\omega\mu\, g(\vec{r},\vec{r}')\, [\hat{n}\times\vec{H}(\vec{r}')] + \frac{i\omega\mu}{k^2} \nabla\nabla g(\vec{r},\vec{r}')\cdot[\hat{n}\times\vec{H}(\vec{r}')]$$

$$+\nabla g(\vec{r},\vec{r}')\times[\hat{n}\times\vec{E}(\vec{r}')]\}$$

2-D Results

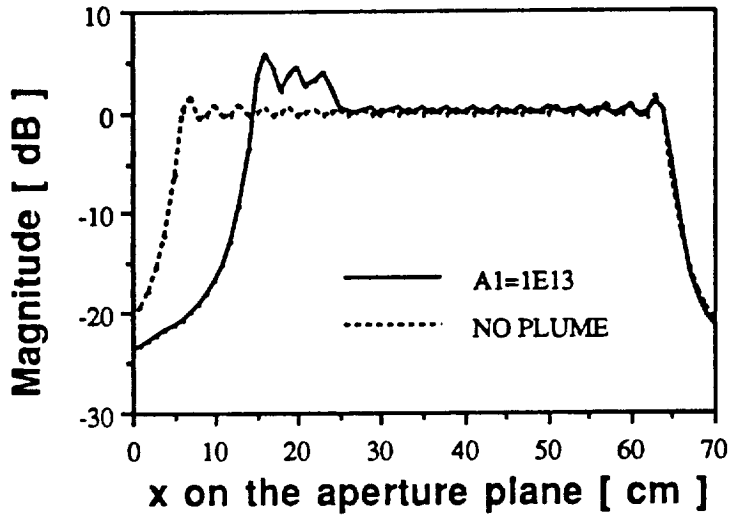
Magnitude [dB]
10
0
-10
-20
-30
0
10
20
30
40
50
60
70
x on the aperture plane [cm]
A1=1E13
NO PLUME

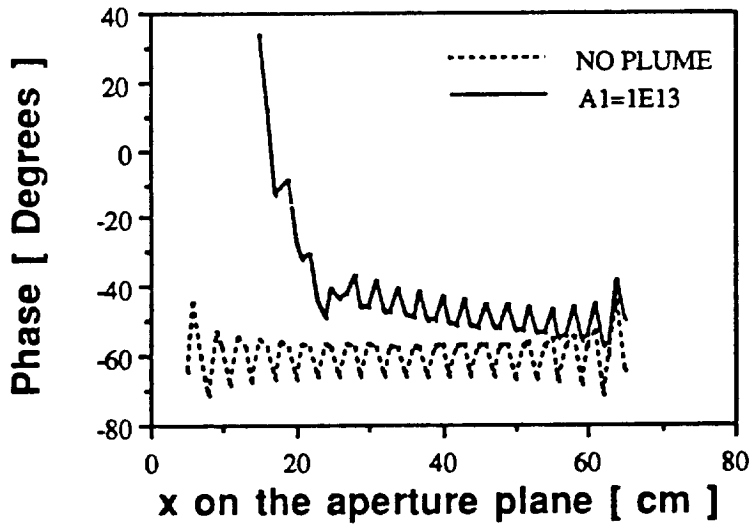
Phase [Degrees]
40
20
0
-20
-40
-60
-80
0
20
40
60
80
x on the aperture plane [cm]
NO PLUME
A1=1E13

3-D Results

Data Sampling:

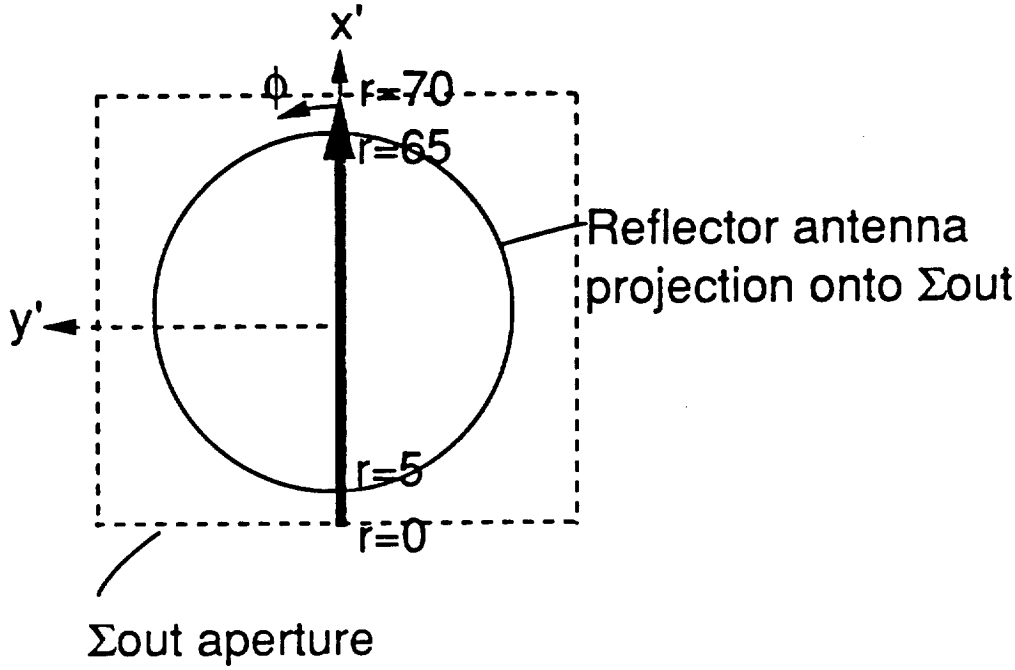

Data sampling at ϕ = 0 degree :

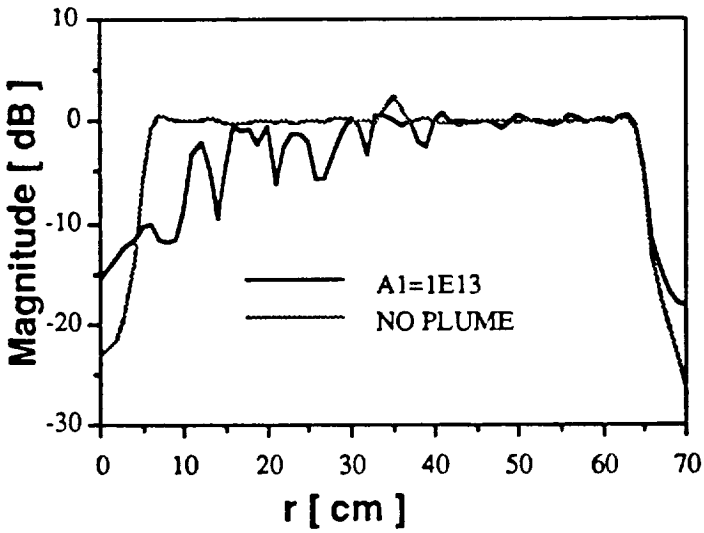

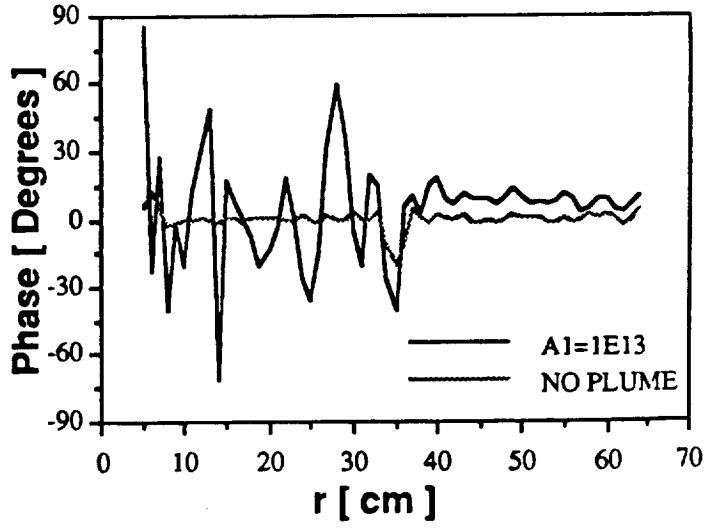

2. Modeling Scatterer Boundary

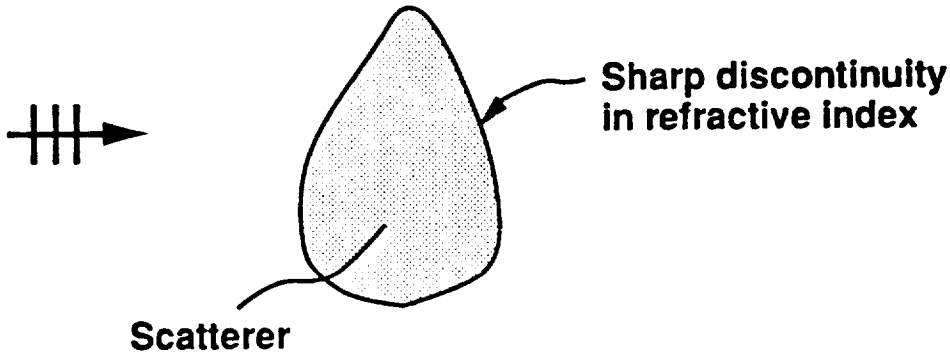

Motivation: Comparison with preliminary experiment

Approach :

1) Propagation through continuous inhomogeneous media

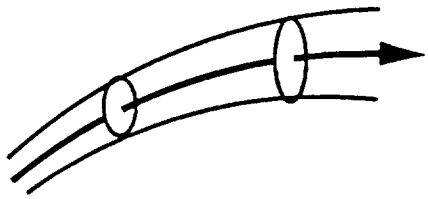

2) Reflection/ refraction at boundary discontinuity

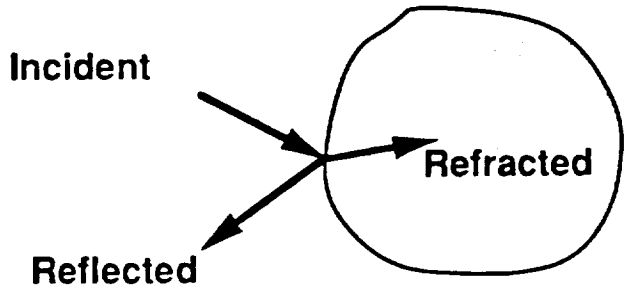

Scattering from 2-D Circular Dielectric Cylinder

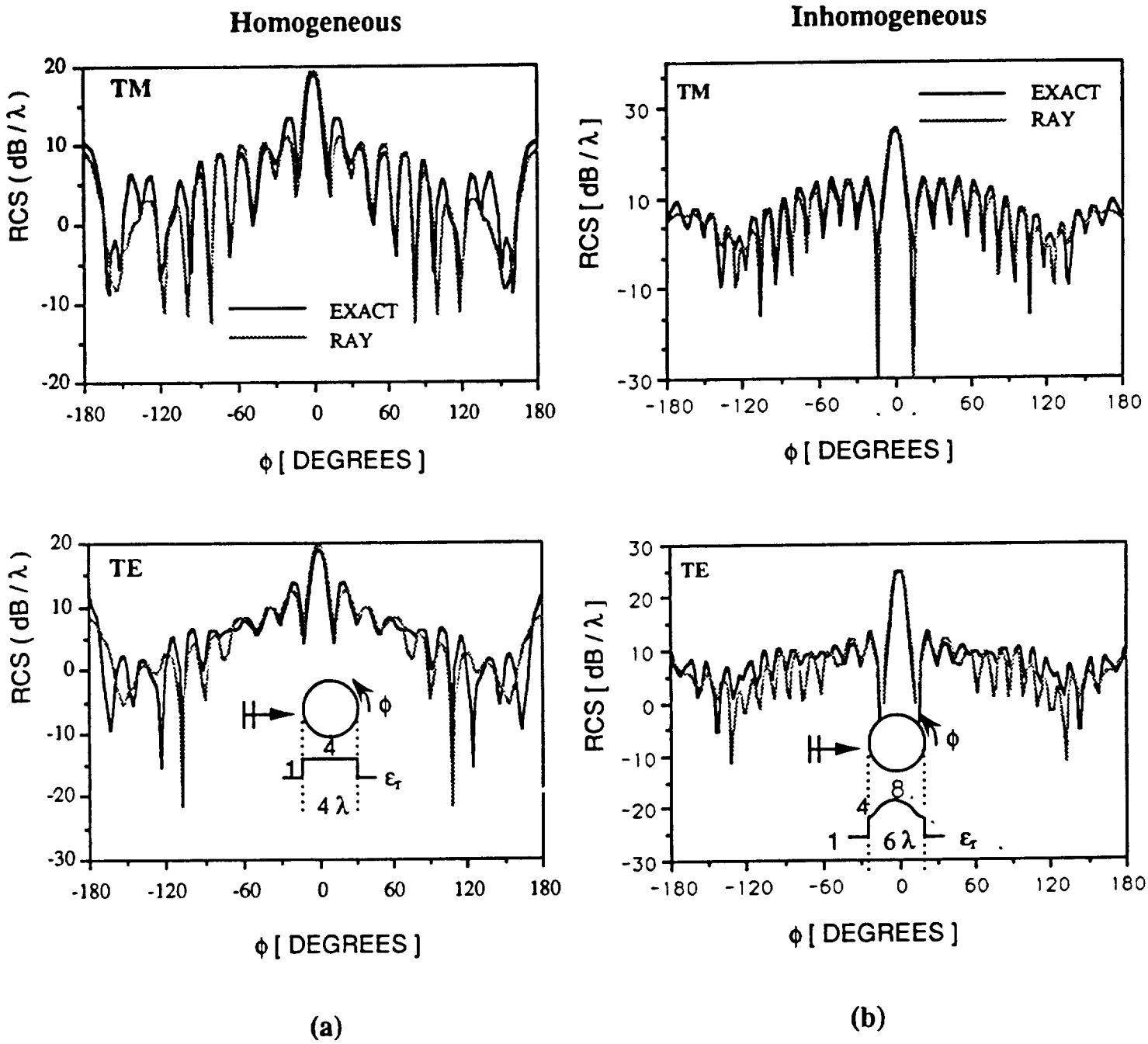

3. Variable Step Size Ray Tracing

- **Fixed step size in ray tracing algorithm**

  $\Longrightarrow$ Too much computation time !!!

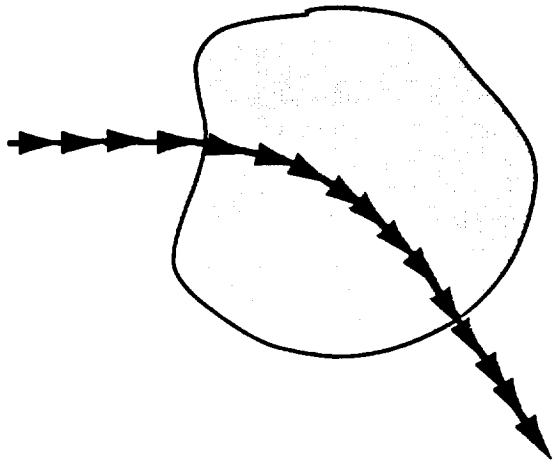

- **Variable step size**

  $\Longrightarrow$ Use large step size when refractive index variation is small

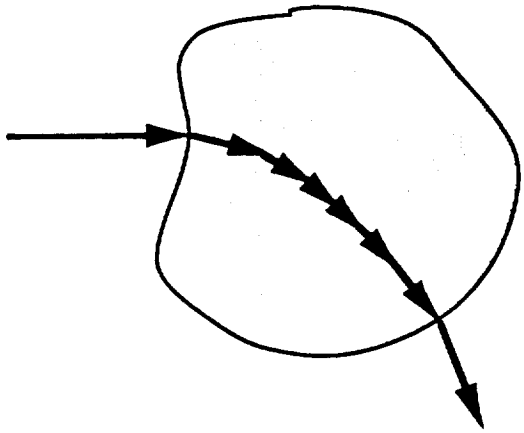

Algorithm

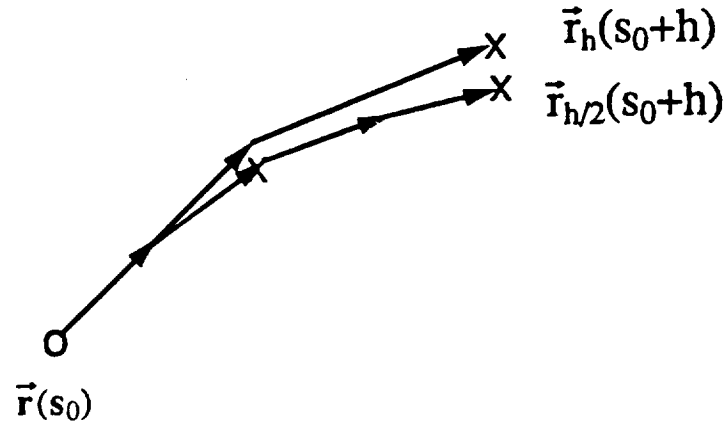

Local truncation error ~ $D_n = | \vec{r}_h(s_0+h) - \vec{r}_{h/2}(s_0+h) |$

$\vec{r}_h(s_0+h)$: ray trajectory using step size h

$\vec{r}_{h/2}(s_0+h)$: ray trajectory using step size h/2

ERRLIM : error tolerance

Based on local error,

if $D_n <$ ERRLIM, $\vec{r}_h(s_0+h)$ is accepted and increase stepsize

if $D_n >$ ERRLIM, reduce step size and try again

Details in Conte and Boor, *Elementary Numerical Analysis*, 3rd ed., p 366-372,1981

3.2. Validation of 3-D Ray Results

1) Layered model solution

Problem statement: Find the scattered field of a spherically inhomogeneous sphere by modelling it as a multi-layered sphere.

Details in J. R. Wait, "Electromagnetic scattering from a radially inhomogeneous sphere," Appli. Sci. Res., section B, vol. 10, pp. 441-450, 1963

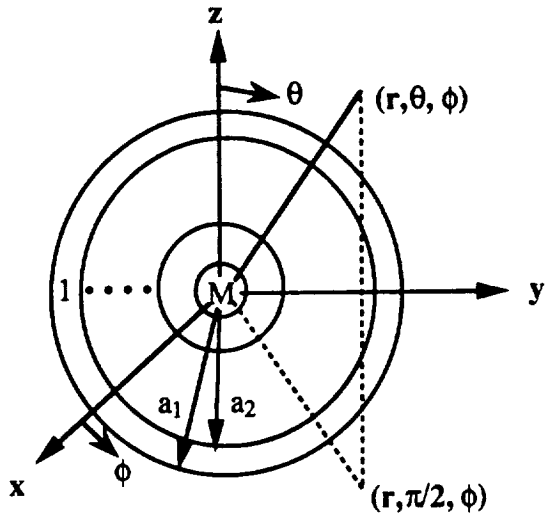

incident plane wave

$$E_x^i = E_0 e^{-jkz}$$

Far-field scattered field:

$$E_\theta^s = \frac{jE_0}{kr} e^{-jkr} \cos\phi \, P(\theta)$$

$$E_\phi^s = \frac{-jE_0}{kr} e^{-jkr} \sin\phi \, Q(\theta)$$

where

$$P(\theta) = \sum_{n=1}^{\infty} \frac{(2n+1)}{n(n+1)} \left[B_n \frac{d}{d\theta} P_n'(\cos\theta) + C_n \frac{P_n'(\cos\theta)}{\sin\theta} \right]$$

$$Q(\theta) = \sum_{n=1}^{\infty} \frac{(2n+1)}{n(n+1)} \left[B_n \frac{P_n'(\cos\theta)}{\sin\theta} + C_n \frac{d}{d\theta} P_n'(\cos\theta) \right]$$

$$B_n = -\frac{\hat{J}_n'(ka_1) - j\Delta_n \hat{J}_n(ka_1)}{\hat{H}_n^{(2)'}(ka_1) - j\Delta_n \hat{H}_n^{(2)'}(ka_1)}$$

$$C_n = -\frac{\hat{J}_n'(ka_1) - j\delta_n \hat{J}_n(ka_1)}{\hat{H}_n^{(2)'}(ka_1) - j\delta_n \hat{H}_n^{(2)'}(ka_1)} \qquad \text{with} \qquad k = \omega\sqrt{\varepsilon_0\mu_0}$$

$$\Delta_n = Z_1^n/\eta_0$$

$$\delta_n = Y_1^n\eta_0$$

Input impedance and admittance from the outside can be calculated from the following recurrence relationship.

$$Z_{m-1}^n = \frac{k}{j\omega\varepsilon}\frac{[\hat{J}_n'(ka_{m-1})\hat{N}_n'(ka_m) - \hat{N}_n'(ka_{m-1})\hat{J}_n'(ka_m)] + \frac{j\omega\varepsilon}{k}Z_m^n[\hat{N}_n'(ka_{m-1})\hat{J}_n(ka_m) - \hat{J}_n'(ka_{m-1})\hat{N}_n(ka_m)]}{[\hat{J}_n(ka_{m-1})\hat{N}_n'(ka_m) - \hat{N}_n(ka_{m-1})\hat{N}_n'(ka_m)] + \frac{j\omega\varepsilon}{k}Z_m^n[\hat{N}_n(ka_{m-1})\hat{J}_n(ka_m) - \hat{J}_n(ka_{m-1})\hat{N}_n(ka_m)]}$$

$$Y_{m-1}^n = \frac{k}{j\omega\mu}\frac{[\hat{J}_n'(ka_{m-1})\hat{N}_n'(ka_m) - \hat{N}_n'(ka_{m-1})\hat{J}_n'(ka_m)] + \frac{j\omega\mu}{k}Y_m^n[\hat{N}_n'(ka_{m-1})\hat{J}_n(ka_m) - \hat{J}_n'(ka_{m-1})\hat{N}_n(ka_m)]}{[\hat{J}_n(ka_{m-1})\hat{N}_n'(ka_m) - \hat{N}_n(ka_{m-1})\hat{N}_n'(ka_m)] + \frac{j\omega\mu}{k}Y_m^n[\hat{N}_n(ka_{m-1})\hat{J}_n(ka_m) - \hat{J}_n(ka_{m-1})\hat{N}_n(ka_m)]}$$

with $m = M, M-1, \ldots, 1$

$$Z_M^n = -j\eta\frac{\hat{J}_n'(ka_M)}{J_n(ka_M)}$$

$$Y_M^n = \frac{1}{j\eta}\frac{\hat{J}_n'(ka_M)}{J_n(ka_M)}$$

2) Ray formulation

The ray scattering formulation for validation is based on Huygens' principle as in two-dimensional case. A dense grid of geometrical optics (GO) rays representing the incident plane wave is shot toward the inhomogeneous object. The shot rays are traced numerically, considering the discontinuous boundary and propagation inside the object. Whenever the rays cross the Huygens' surface S, the contributions of the rays to the scattered field are calculated by a ray-tube integration scheme.

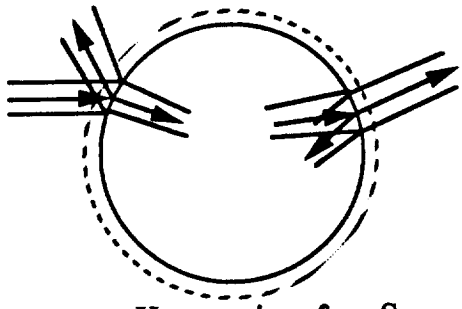

Huygens' surface S

At discontinuous boundary:

The ray tangential vector, amplitude, polarization and wavefront curvature of refflected (or refracted) are calculated from those of the incident ray using Snell's law, Fresnel's formulations for reflection (or refraction) coefficient, and phase matching.

Inside the object:

The ray trajectory, the associated phase, amplitude and polarization of the ray field are traced numerically.

Formulation of ray tube integration

: Integrate over ray-tube projection on Huygens' surface

3-D radiation integral in the far field:

$$\vec{E}^s = \frac{e^{jkr}}{r}\left[\hat{\theta}A_\theta + \hat{\phi}A_\phi\right]$$

$$\begin{bmatrix} A_\theta \\ A_\phi \end{bmatrix} = \frac{jk}{4\pi}\int_{\substack{\text{ray-tube} \\ \text{projection} \\ \text{on S}}} e^{j\vec{k}_0\cdot\vec{r}'}\left(\begin{bmatrix} \hat{\phi} \\ \hat{\theta} \end{bmatrix} \times \vec{E}(r') + \eta\begin{bmatrix} \hat{\theta} \\ \hat{\phi} \end{bmatrix} \times \vec{H}(r')\right)\cdot \hat{n}\ ds'$$

$$\vec{r} = \vec{r}_a + \vec{r}'$$

$$\vec{r}_a = x_a\hat{x}+y_a\hat{y}+z_a\hat{z}$$

$$\vec{r} = x\hat{x}+y\hat{y}+z\hat{z}$$

$$\vec{v} = v_x\hat{x}+v_y\hat{y}+v_z\hat{z}$$

$$\vec{n} = n_x\hat{x}+n_y\hat{y}+n_z\hat{z} = \frac{x_a}{a}\hat{x}+\frac{y_a}{a}\hat{y}+\frac{z_a}{a}\hat{z}$$

$$\vec{k} = k(\cos\phi\sin\theta\,\hat{x}+\sin\phi\sin\theta\,\hat{y}+\cos\theta\,\hat{z})$$

$$\hat{\phi} = \cos\theta\cos\phi\,\hat{x}+\cos\theta\sin\phi\,\hat{y}-\sin\theta\,\hat{z}$$

$$\hat{\theta} = -\sin\phi\hat{x}+\cos\phi\,\hat{y}$$

$$\vec{E}(\vec{r}) \cong \vec{E}(\vec{r}_a)\exp\{-jk\hat{t}\cdot(\vec{r}-\vec{r}_a)\}$$

$$\vec{H}(\vec{r}) \cong \vec{H}(\vec{r}_a)\exp\{-jk\hat{t}\cdot(\vec{r}-\vec{r}_a)\} = \frac{\hat{v}\times\vec{E}(\vec{r}_a)}{Z_0}\exp\{-jk\hat{t}\cdot(\vec{r}-\vec{r}_a)\}$$

$$\begin{bmatrix} A_\theta \\ A_\phi \end{bmatrix} = \frac{jk}{4\pi} \int_{\substack{\text{ray tube} \\ \text{projection} \\ \text{on S}}} e^{j\vec{k}\cdot\vec{r}_a} \left(\begin{bmatrix} -\hat{\phi} \\ \hat{\theta} \end{bmatrix} \times \vec{E}(\vec{r}_a) + \eta \begin{bmatrix} \hat{\theta} \\ \hat{\phi} \end{bmatrix} \times \vec{H}(\vec{r}_a) \right) e^{-jk\hat{t}\cdot(\vec{r}-\vec{r}_a)} \cdot \hat{n}\, ds$$

$$\equiv \frac{jk}{4\pi} e^{j\vec{k}\cdot\vec{r}_a} \left(\begin{bmatrix} -\hat{\phi} \\ \hat{\theta} \end{bmatrix} \times \vec{E}(r_a) + \eta \begin{bmatrix} \hat{\theta} \\ \hat{\phi} \end{bmatrix} \times \vec{H}(r_a) \right) \cdot \hat{n}\ (\Delta A)\, S(\theta,\phi)$$

$$= \frac{jk}{4\pi} e^{j\vec{k}\cdot\vec{r}_a} \begin{bmatrix} B_\theta \\ B_\phi \end{bmatrix} (\text{Area})_{proj}\, S(\theta,\phi)$$

$$S(\theta, \phi) = \frac{1}{(\text{Area})_{proj}} \int_{\substack{\text{raytube} \\ \text{projection} \\ \text{on S}}} e^{jk(\hat{k}-\hat{v})\cdot\vec{r}'} ds'$$

$$B_\theta = (-\hat{\phi}\times\vec{E} + \eta\hat{\theta}\times\vec{H})\cdot\hat{n} = [-n_x E_z \cos\phi - n_y E_z \sin\phi + n_z(E_y \sin\phi + E_x \cos\phi)]$$

$$+ \eta[n_x(H_z \cos\theta \sin\phi + H_y \sin\theta) - n_y(H_z \cos\theta + H_x \sin\theta) + n_z(H_y \cos\theta \cos\phi - H_x \cos\theta \sin\phi)]$$

$$B_\phi = (\hat{\theta}\times\vec{E} + \eta\hat{\phi}\times\vec{H})\cdot\hat{n}$$

$$= n_x(E_z \cos\theta \sin\phi + E_y \sin\theta) - n_y(E_z \cos\theta + E_x \sin\theta) + n_z(E_y \cos\theta \cos\phi - E_x \cos\theta \sin\phi)$$

$$+ \eta[n_x H_z \cos\phi + n_y H_z \sin\phi - n_z(H_y \sin\phi + H_x \cos\phi)]$$

$$(\text{Area})_{proj} = \pi A^2 = \frac{(\text{Area})_{in}}{|DF|^2} \left(\frac{1}{\hat{n}\cdot\hat{v}}\right)$$

$(\text{Area})_{in}$: **initial ray-tube size**

$$S(\theta, \phi) = \frac{2J_1(u)}{u}, \quad u = kA \sin[\cos^{-1}\{(\hat{k}-\hat{v})\cdot\hat{n}\}]$$

3) Comparisons

Permittivity profile:

$$\varepsilon_r(r) = d + b(1 - c\ \cos\frac{\pi r}{a})$$

where

$$b = \frac{1+\varepsilon_r(0)}{2}$$

$$c = \frac{1-\varepsilon_r(0)}{1+\varepsilon_r(0)}$$

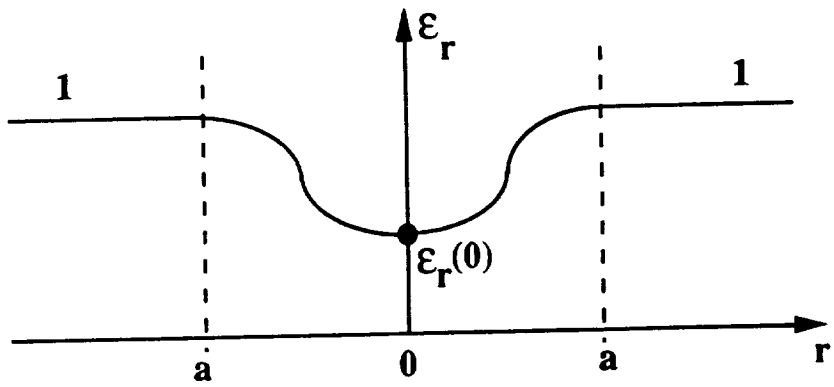

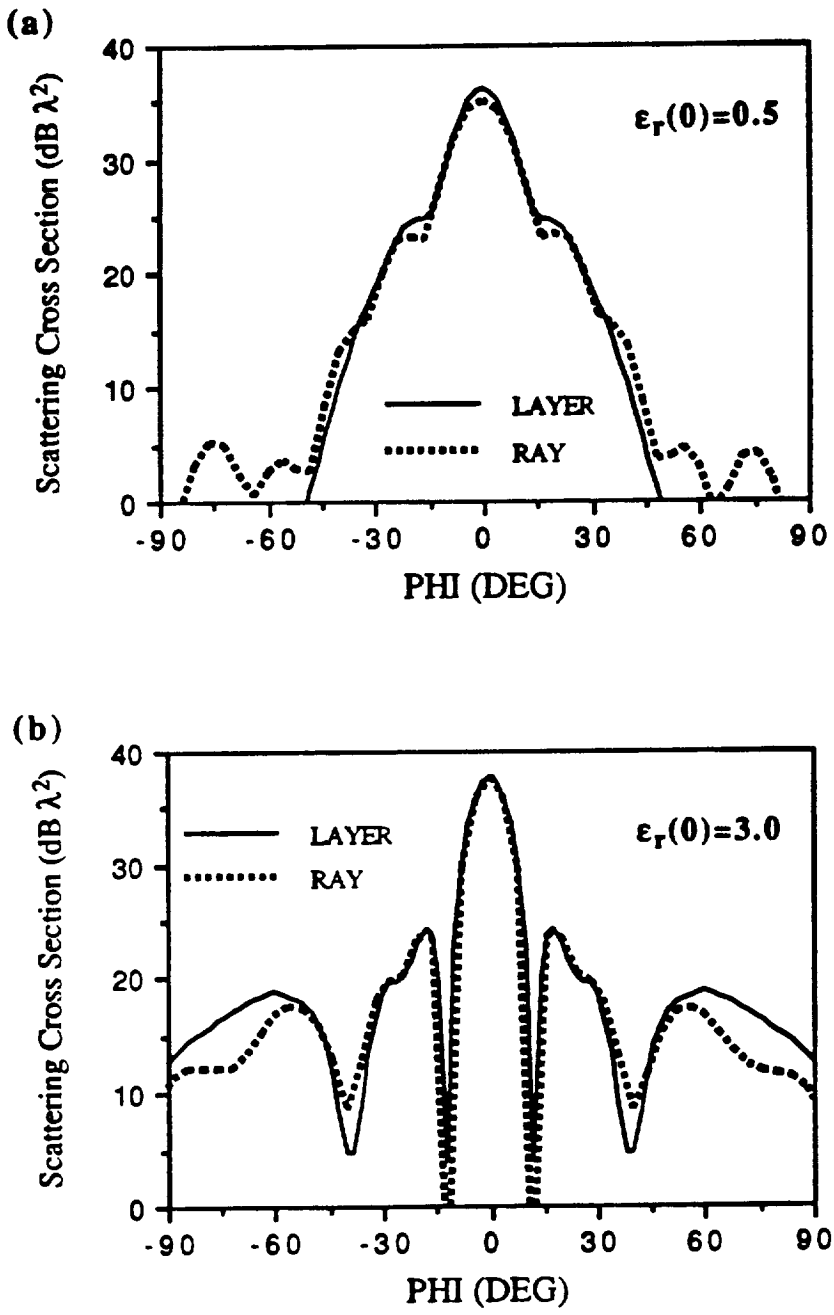

Comparion of the scattering cross section of an inhomogeneous sphere of diameter 6λ calculated using ray optics and that obtained from the multi-layered solution. (a) $\varepsilon_r(0)=0.5$. (b) $\varepsilon_r(0)=3.0$.

APPENDIX 1.

1990 High Temperature Plasma Diagnostics Conference Presentation

ARCJET PLASMA PLUME EFFECT ON A MICROWAVE REFLECTOR ANTENNA.*

B.W. Birkner, G.A. Hallock, H. Kim, H. Ling

The University of Texas at Austin.

Eighth Topical Conference

On High Temperature Plasma Diagnostics

May 6-10 1990

Poster Presentation F27

Abstract

A configuration is described to measure the effect of the plasma produced by an arcjet thruster on a reflector antenna. The diagnostic consists of a small movable RF probe coupled to a Hewlett-Packard HP 8510 network analyzer. Because the perturbation is expected to be small ($\sim 10^\circ$ phase shift) wall reflections are an important consideration. To minimize their effect we use Fourier transform gating techniques.

*Supported by the NASA Lewis Research Center

INTRODUCTION

- Electric Propulsion for space applications has regained interest in recent years due to availability of large power supplies for satellites.
- Arcjet thrusters, one of the simplest devices, can attain specific impulse levels above 400 sec. Arcjet thruster propulsion consists in heating a flowing gas in a constricted volume by means of an arc discharge thus obtaining thrust by heat expansion. See Figure 1.
- Use of arcjet thrusters for stationkeeping and attitude control can potentially extend the lifetime of modern satellites up to ten years.
- Focus of this work is on the $\sim 1KW$ class arcjet thruster.
- Higher power arcjets are being developed for boosting satellites from Earth orbit to geosynchronous orbit.
- The arcjet produces a weakly ionized plasma plume during operation. For this technology to be usable on communication satellites, the signal degradation to and from the spacecraft due to refraction and attenuation of the microwave signals must be within acceptable limits.

- Establishing arcjet compatibility with microwave communications requires both modeling and laboratory experiments, with neither approach alone being able to predict the operation of an actual system with adequate confidence:

  1. Modeling is limited by plasma parameters which are not accurately known, and difficulties inherent to wave propagation calculations.
  2. Experimental work is limited by laboratory simulation of the space environment (boundary conditions, vacuum pressure, and wall reflections).

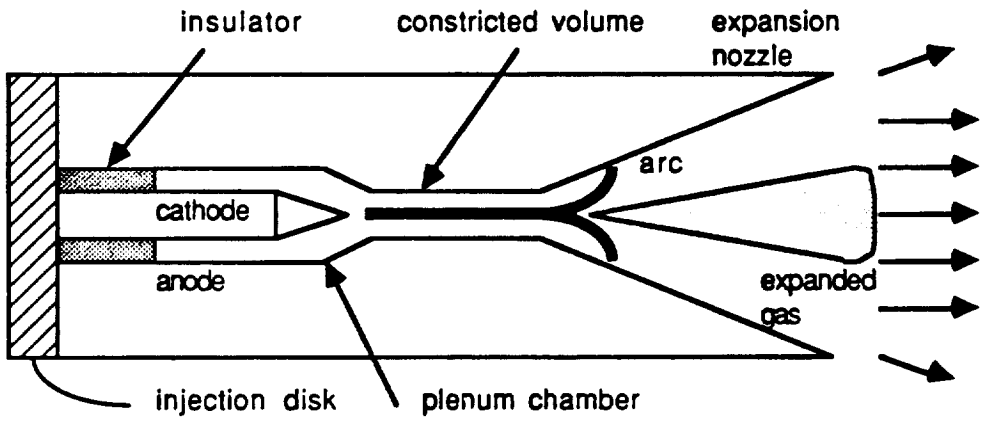

Figure 1: Arcjet Thruster

PLUME MODELING AND RAY TRACING

- The arcjet produces a weakly ionized plasma which extends 10's of centimeters from the arcjet nozzle. See Figure 2 for arcjet geometry and coordinates.

- The cold plasma model provides a very good approximation to the electromagnetic behavior, with index of refraction N given by:

$$N = \sqrt{1 - \frac{\omega_p^2}{\omega^2}}$$

  where ω_p is the electron plasma frequency.

- The plasma frequency dependes on the electron number density ($\omega_p^2 = n_e e^2 / m_e \epsilon_o$), which has been measured experimentally with Langmuir probes. The electron density is $\sim 10^{10} cm^{-3}$ close to the thruster nozzle, and is well modeled by $n_e \propto exp(-\alpha\theta)/r^2$ for all arcjet operating conditions.(See Figure 2).

- A least squares fit to the data is shown in the contour plot in Figure 3 along with the measurement locations.

- Microwave communication frequencies are typically only a factor of 2-20 above the plasma frequency close to the thruster, and the plasma behaves as a very dispersive medium.

- To study the effect of the plasma on the performance of on-board

reflector antennas, the arcjet plume is modeled as an inhomogeneous scatterer with a smoothly varying refractive index.

- Since the plume size is of the order of several wavelengths, geometrical optics is used to calculate the wave propagation.
- Geometrical optics is implemented by means of numerical ray tracing. Given the value of the electric and magnetic fields at some point, the fields can then be calculated along a ray extending from that point.
- Once ray optics fields are obtained on some near-field aperture of the antenna the far-field pattern can be obtained by the Fourier Transform.
- Two-dimensional calculations have been performed indicating the plume can cause serious pointing errors, especially for very narrow beam antennas. In addition deterioration in both the main beam and sidelobes has been observed in the calculations.

EXPERIMENTAL VALIDATION

- Experimental validation is important because the geometrical optics assumptions which underlie the ray-tracing methods are not well satisfied by the plasma plume. For our work *plume size* $\lesssim \lambda$ whereas geometrical optics requires *plume size* $\ll \lambda$.
- Experimental measurement of the effect of the plume on the reflector antenna pattern is planned.
- Due to size limitations of vacuum chambers a far-field radiation pattern is difficult to measure.
- A near-field radiation measurement is feasible and provides a very sensitive test of our code. If near-field calculations are verified correct then our far-field calculations are very accurate.
- The experimental configuration is shown in Figure 4. A 40 cm diameter reflector antenna directs collimated radiation at 10 GHz through the plasma plume. The diagnostic consisits of a small movable RF probe coupled to a Hewlett-Packard HP 8510 network analyzer.
- The arcjet plume will cause the antenna radiation to deflect upward, since the index of refraction is less than unity within the plasma. This changes both the magnitude and phase of the near

field distribution, as shown in Figure 5. The effect is small and is concentrated towards the region closest to the plume. The induced phase shift in this region is $\sim 8°$ and the magnitude change is of the order of 2.5 decibels. In addition a dark region extending for $\sim$2 cm is observed.

- The arcjet thruster requires a modest vacuum for operation $\sim 10^{-4} torr$. To reduce the effect of wall reflections we will make use of the time domain gating feature of the HP 8510 analyzer. In this technique measurements are made over a broad frequency range in the AC steady state, and Fourier transformed to the time domain via the FFT (Fast Fourier Transform). The FFT is applied over a finite bandwidth of positive frequencies. Gating in the time domain is then applied to eliminate the reflections, the latter being shifted in time by the extra path length traveled. The gated data is then transformed back into the frequency domain.
- Time gating introduces several sources of error:
  1. The finite sampling used for the FFT causes aliasing if the extra path length for reflections is too large and/or multiple reflections do not die out quickly.
  2. Short path lengths might not be separable in time.
- Aliasing problem can be reduced by using a sufficiently small

chamber so that the first reflections can be gated out, and vacuum compatible microwave absorbing material which can alleviate multiple bounce effects.

- Because the plasma is dispersive the time domain pulses will be distorted thus complicating the task of gating out the reflections.
- A numerical simulation has been done (shown in Figure 6) where the frequency spectrum of the input signal is assumed Gaussian with a center frequency of 15 GHz and a FWHM of 2.94 GHz.
- In Figure 6(b) is shown the magnitude of the transformed pulse shape of the input signal. The output of this signal after propagating through a homogeneous plasma slab of thickness $d = 20cm$ is computed by assuming that each frequency component undergoes a phase shift of $-(\omega d/c)\sqrt{1-\omega_p^2/\omega^2}$. The results are shown in Figure 6(c) for different plasma frequencies.
- It is shown that as long as the frequency range of measurement is sufficiently above the plasma frequency, no significant pulse distortion will occur. The observed pulse delay is also not significant.
- We have set up a test facility consisting of an antenna chamber, antennas, and an HP 8510 analyzer. We have verified basic system operation, using time gating on induced reflections. We have

successfully compared predicted and measured effects of various dielectrics (such as paraffin) to high accuracy.

- After completing a proof-of-principle work, we plan to set up the measurement configuration at NASA Lewis on their arcjet vacuum facility.

- Figure 7 shows the problem of vacuum chamber wall reflections. The main beam is illustrated together with two direct reflections – the side wall refection and the back wall reflection, and a multiple bounce reflection.

- The following figures illustrate the time gating procedure with actual HP 8510 measurements:

  1. Measured frequency response in "clean" environment, Figure 8.
  2. Frequency response with a strong reflection, Figure 9.
  3. Frequency response with gated out reflection, Figure 10.

- Gating errors are of major concern and an illustration of the distortion produced on the frequency response by time gating is illustrated in Figure 11, Figure 12, and Figure 13. Preliminary calculations were done to estimate the time gating error in terms of the root mean square error over the measuring frequency span:

1. For small gating (Figure 12) the frequency response magnitude rms-error is $\sim 1\%$, and the phase rms-error is $\sim 1.8°$.
2. For large gating (Figure 13) the frequency response magnitude rms-error is $\sim 0.5\%$, and the phase rms-error is $\sim 0.1°$.

- For a 12-18 GHz reflector feed sweep sampled with 800 points we obtain a time domain window of 50 nsec, corresponding to an electrical length of 15 m. In addition the time domain 50% pulse width is $\sim$ 0.1 nsec, corresponding to an electrical length of $\sim$ 4 cm.

- Some considerations on the choice of frequency span are listed below:

1. Lower frequencies are preferred because more plasma induced phase shift can be observed. But for lower frequencies the reflector beam is not well as collimated.
2. Only the interior of the frequency sweep is of concern for the plume degradation measurements.
3. Most of the frequency sweep is used for time gating.

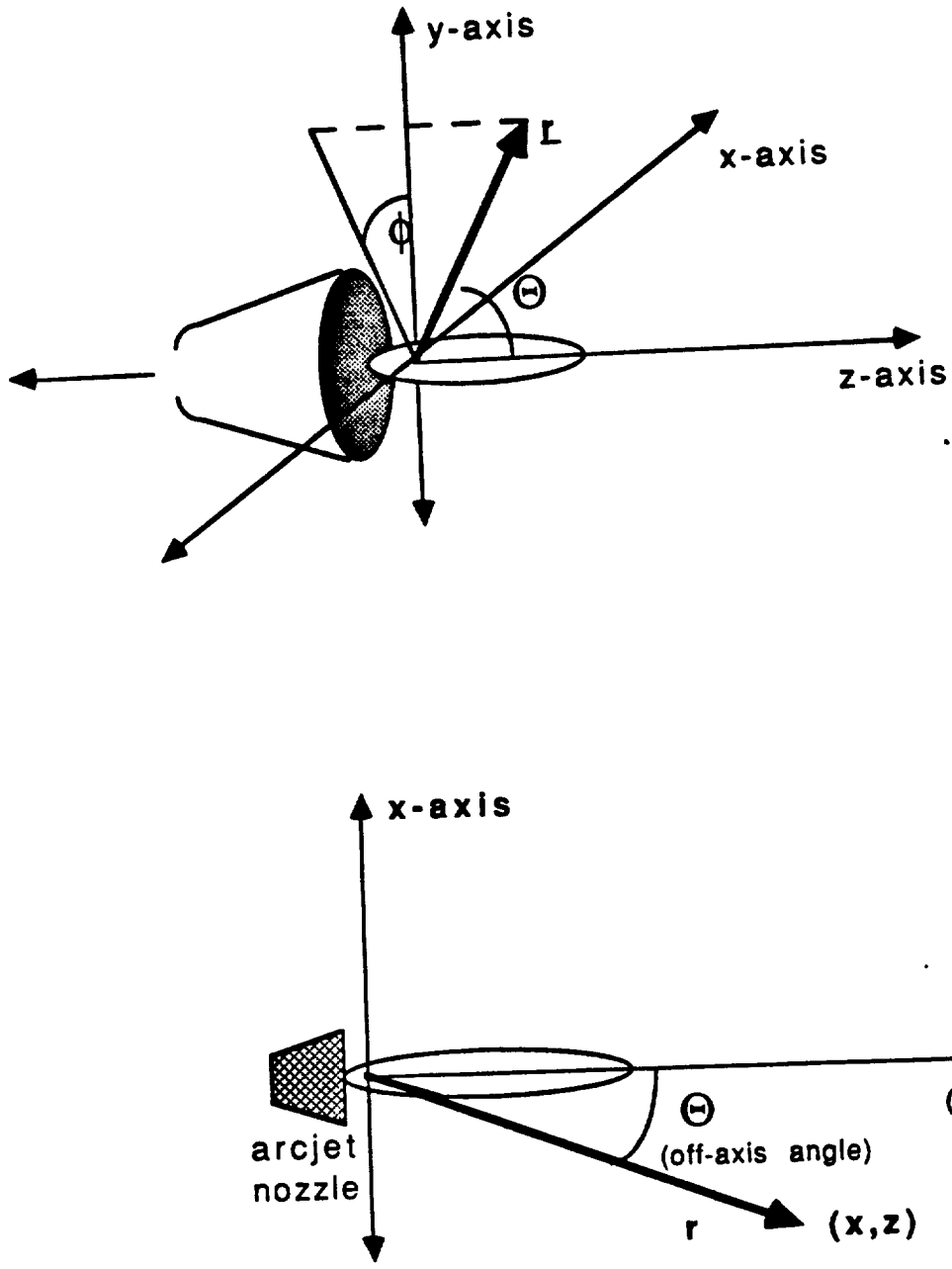

Figure 2: Arcjet Thruster Geometry and Coordinates

Figure 3. Contour Plot of the arcjet electron density profile. Measurement locations are denoted by x. The contours are given by the least squares fit $n_e = 9.1 \times 10^{11} exp(-0.019\theta)/r^2\, cm^{-3}$ (θ in degrees, r in cm).

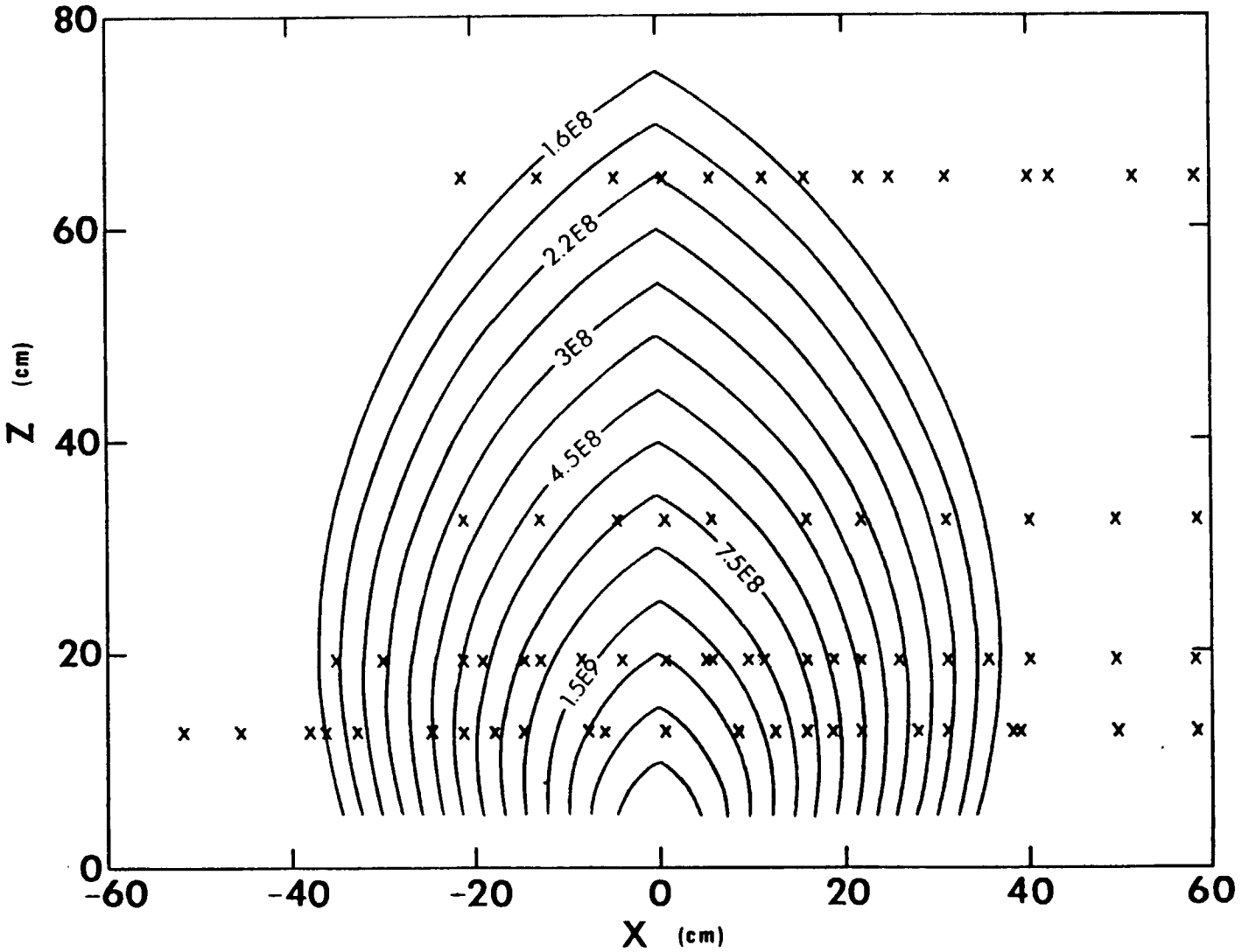

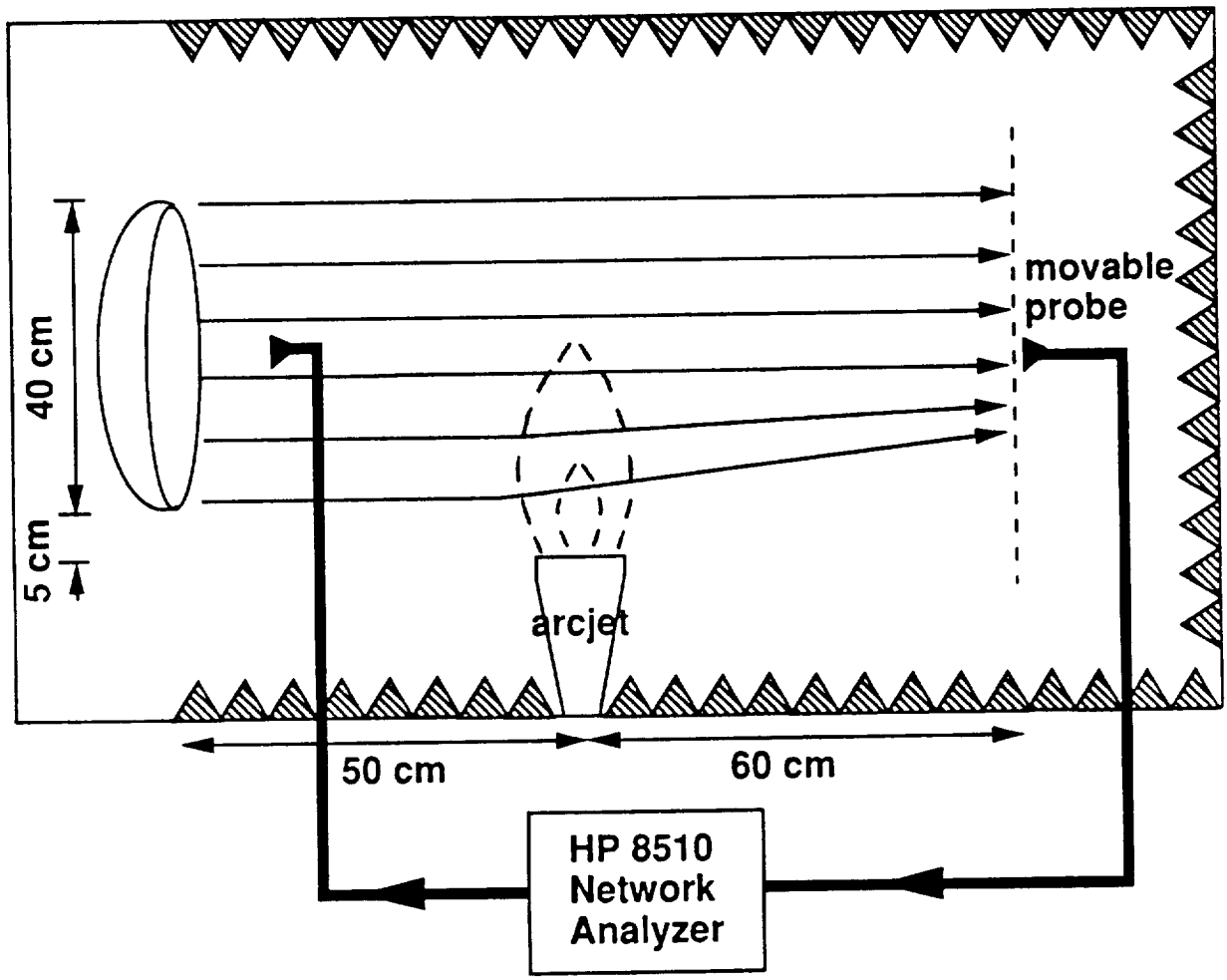

Figure 4: Schematic of the measurement configuration, showing approximate ray trajectories in the presence of the plasma.

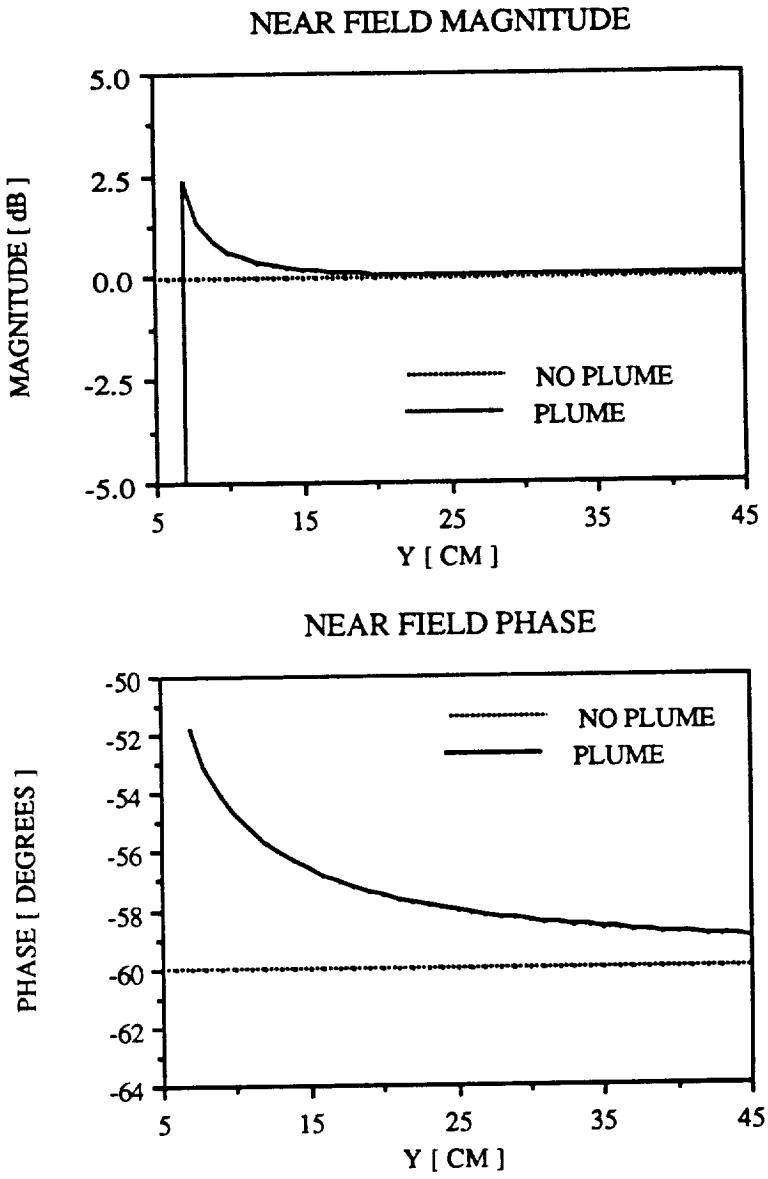

Figure 5: Calculated near-field magnitude and phase (referenced to the antenna plane) with and without plasma.

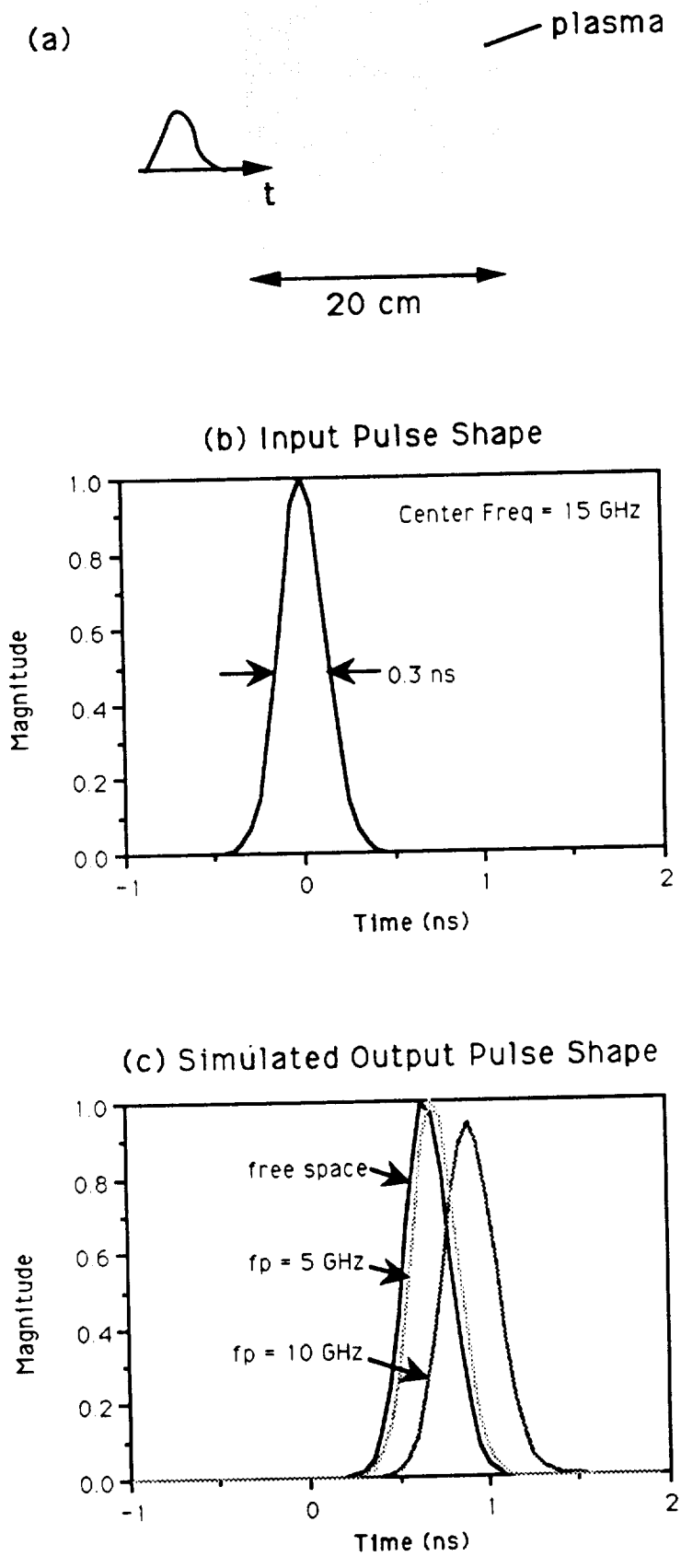

Figure 6: Simulated time-domain output of the input pulse shape and the output pulse shapes after propagation through a 20 cm plasma slab.

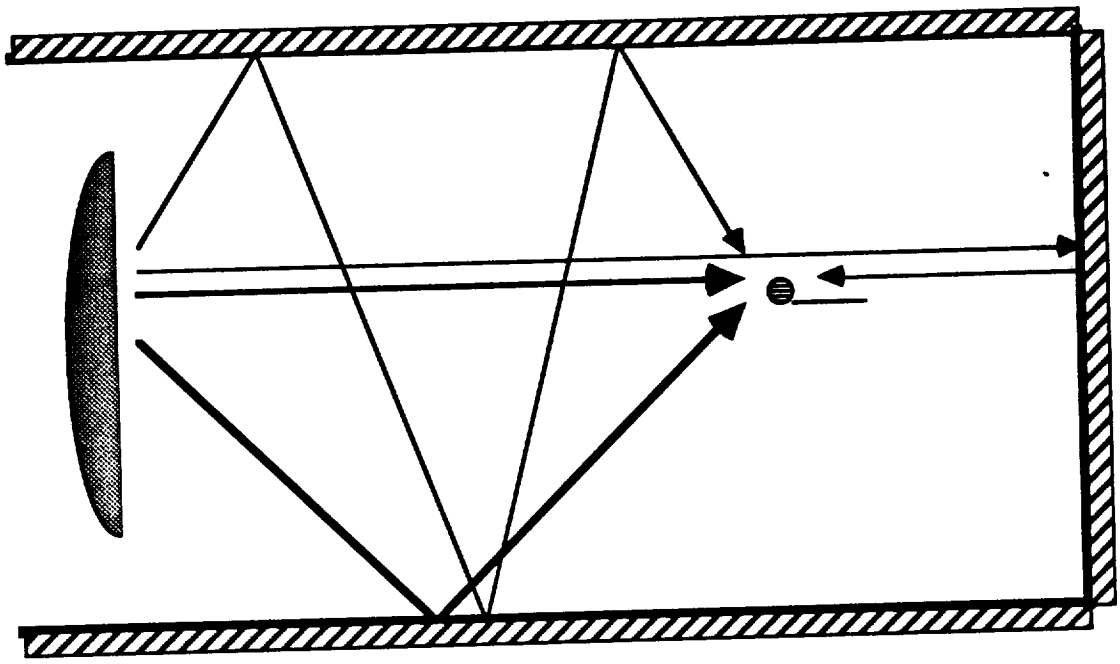

Figure 7: Illustration of Main beam and the different reflections present in vacuum chamber antenna measurements.

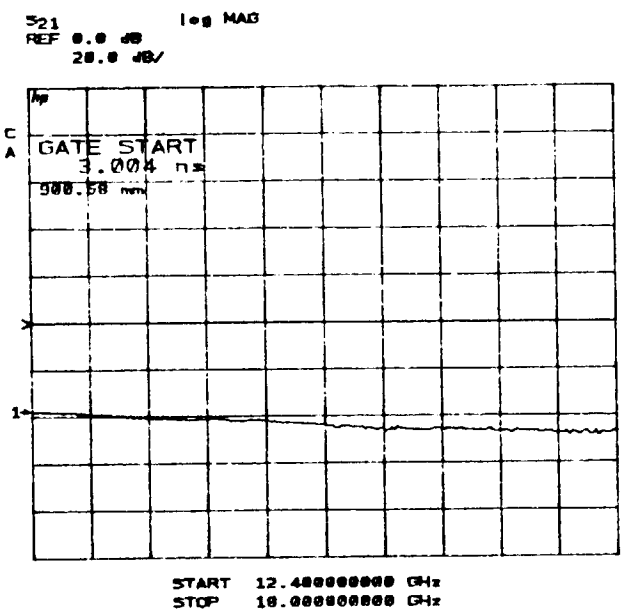

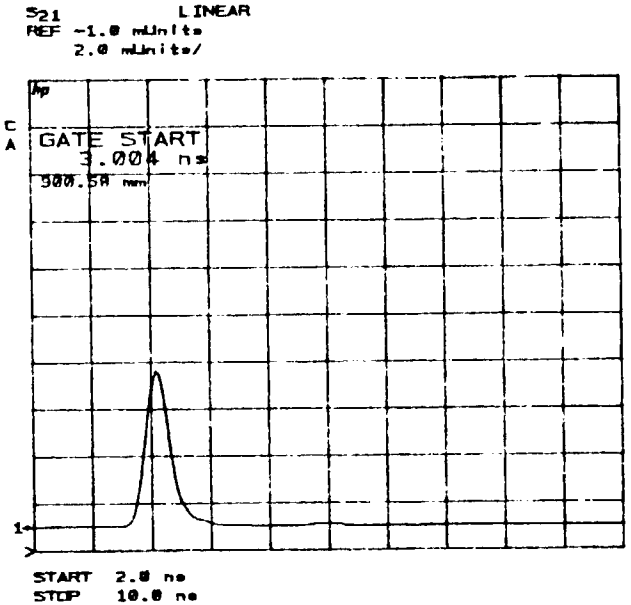

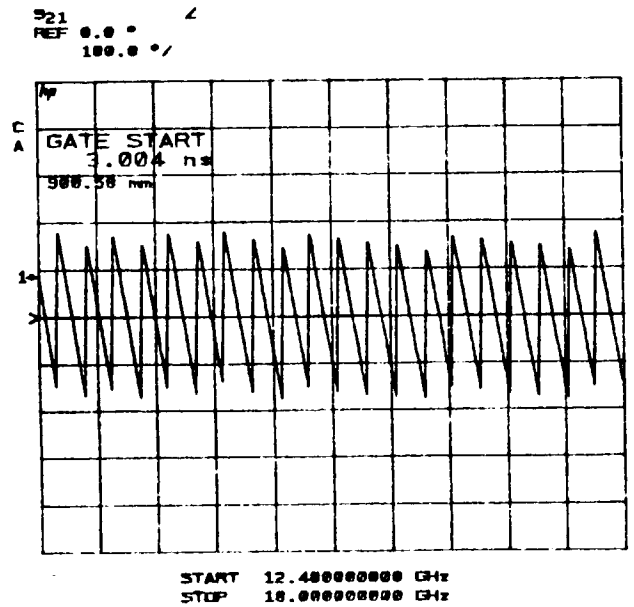

Figure 8: Frequency response and time domain with no reflections.

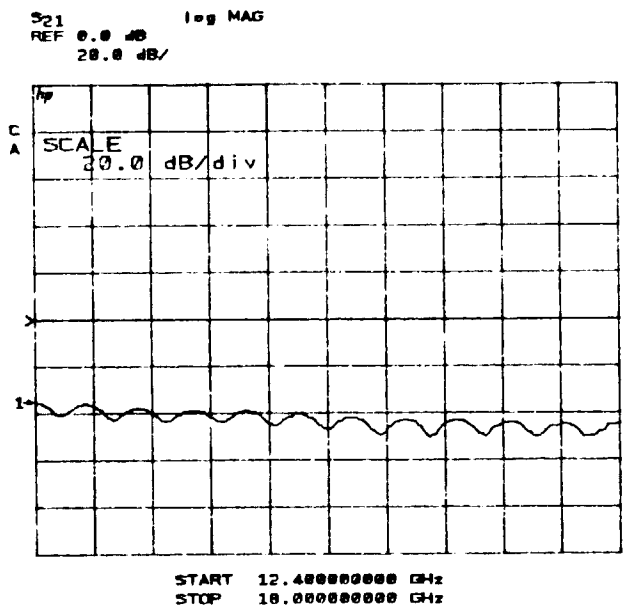

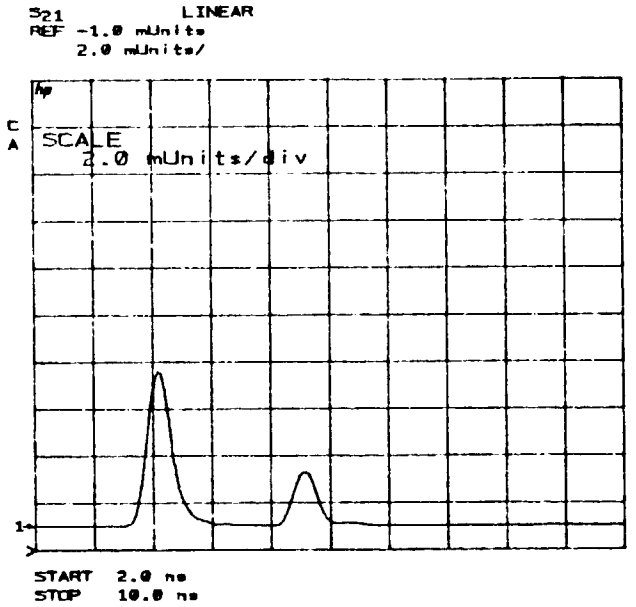

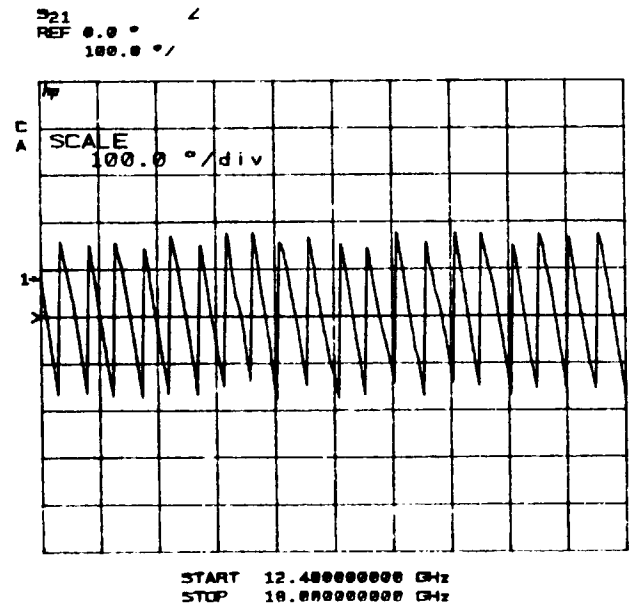

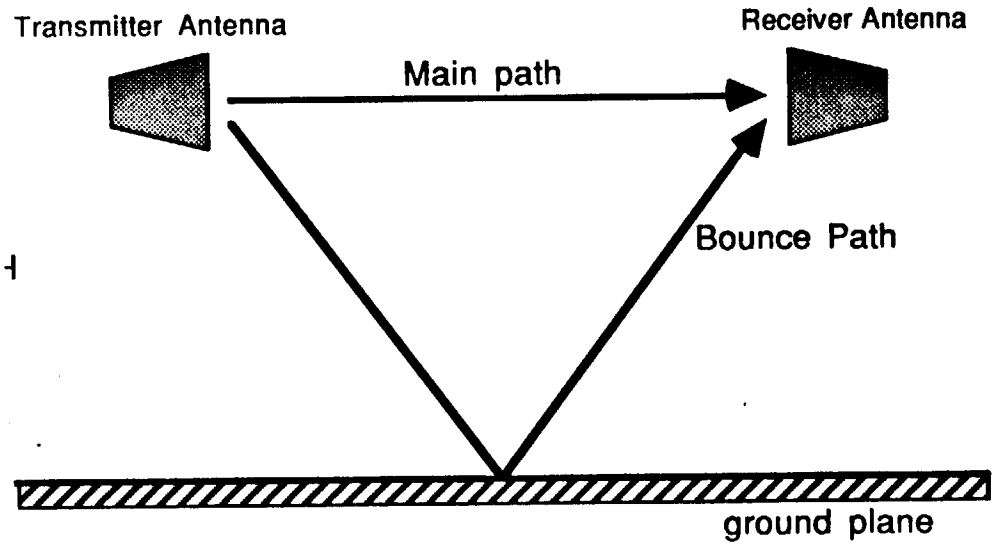

Figure 9: Frequncy response and time domain with enhanced reflection.

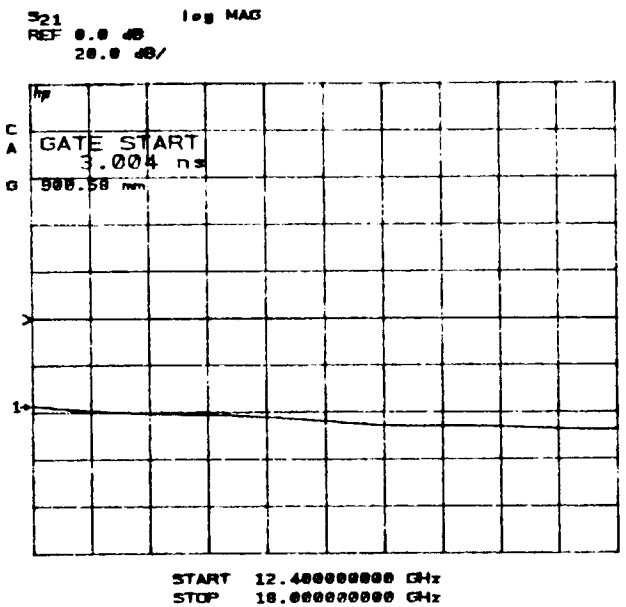

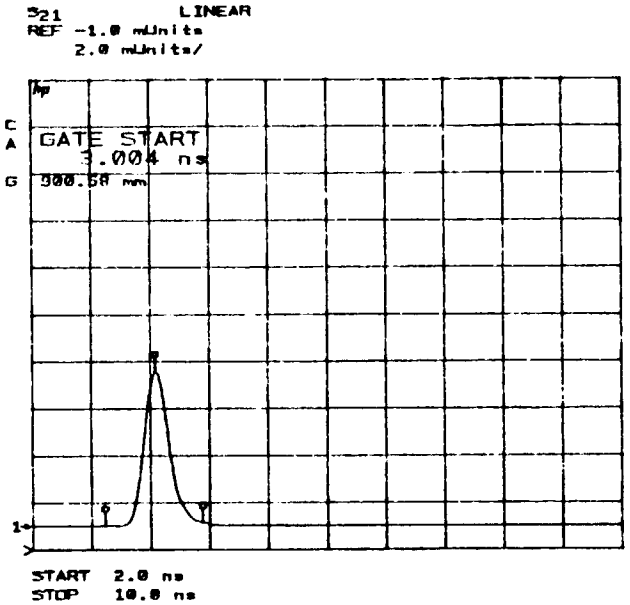

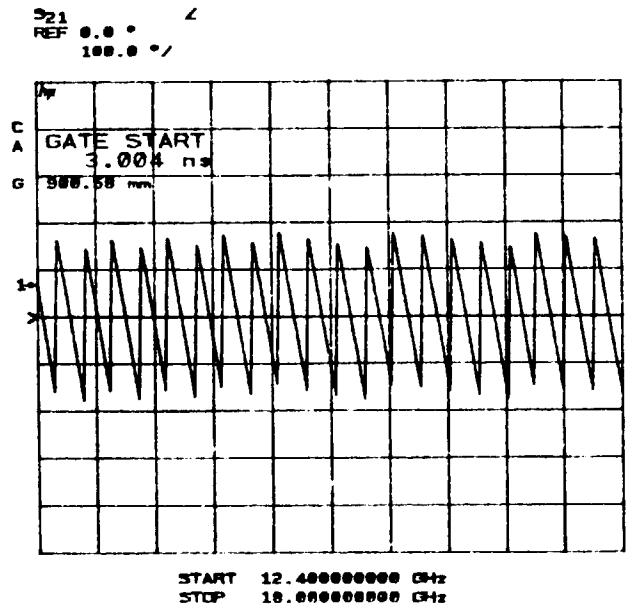

Figure 10: Frequency response and time domain with gated out reflection.

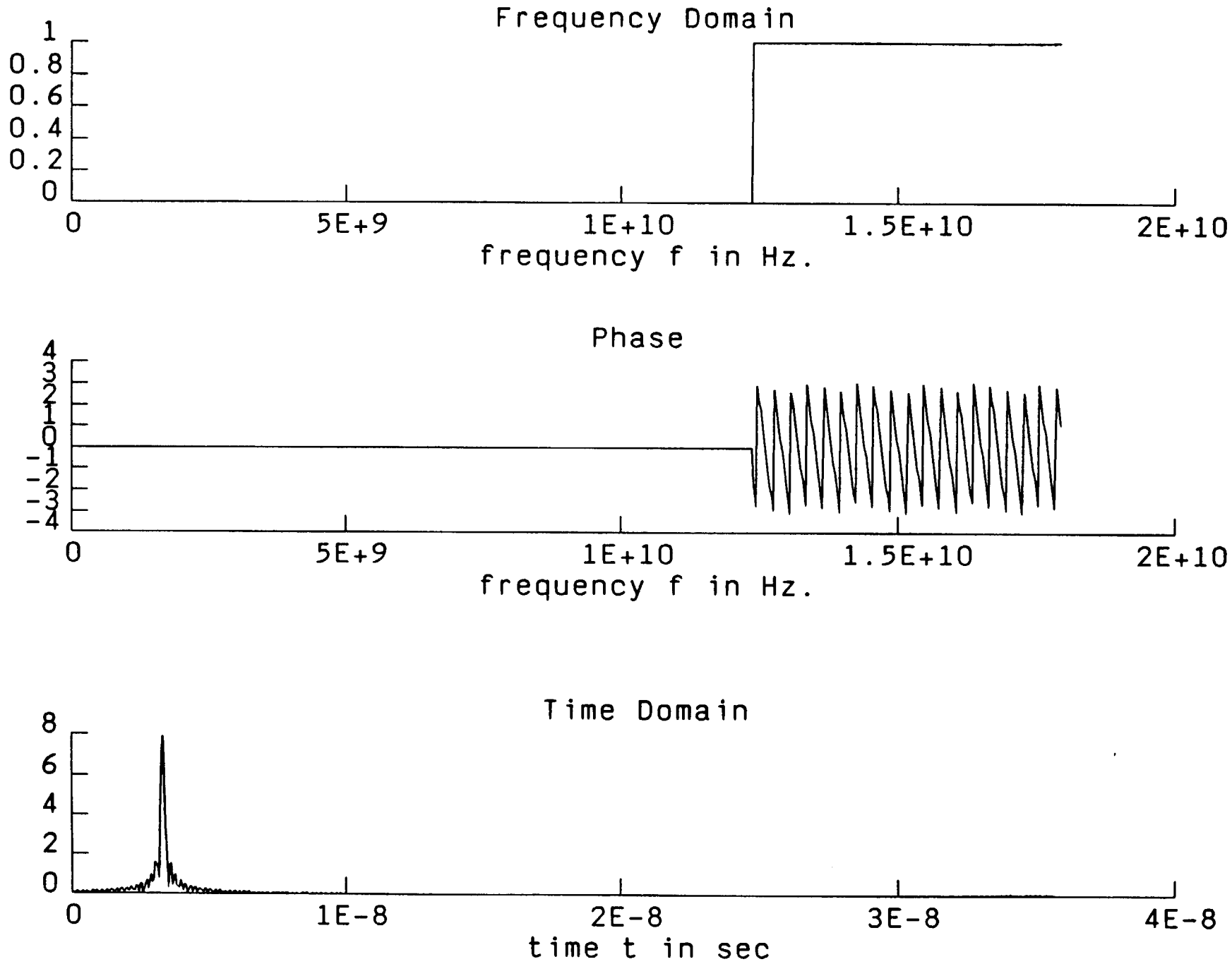

Figure 11: Simulated FFT with no gating.

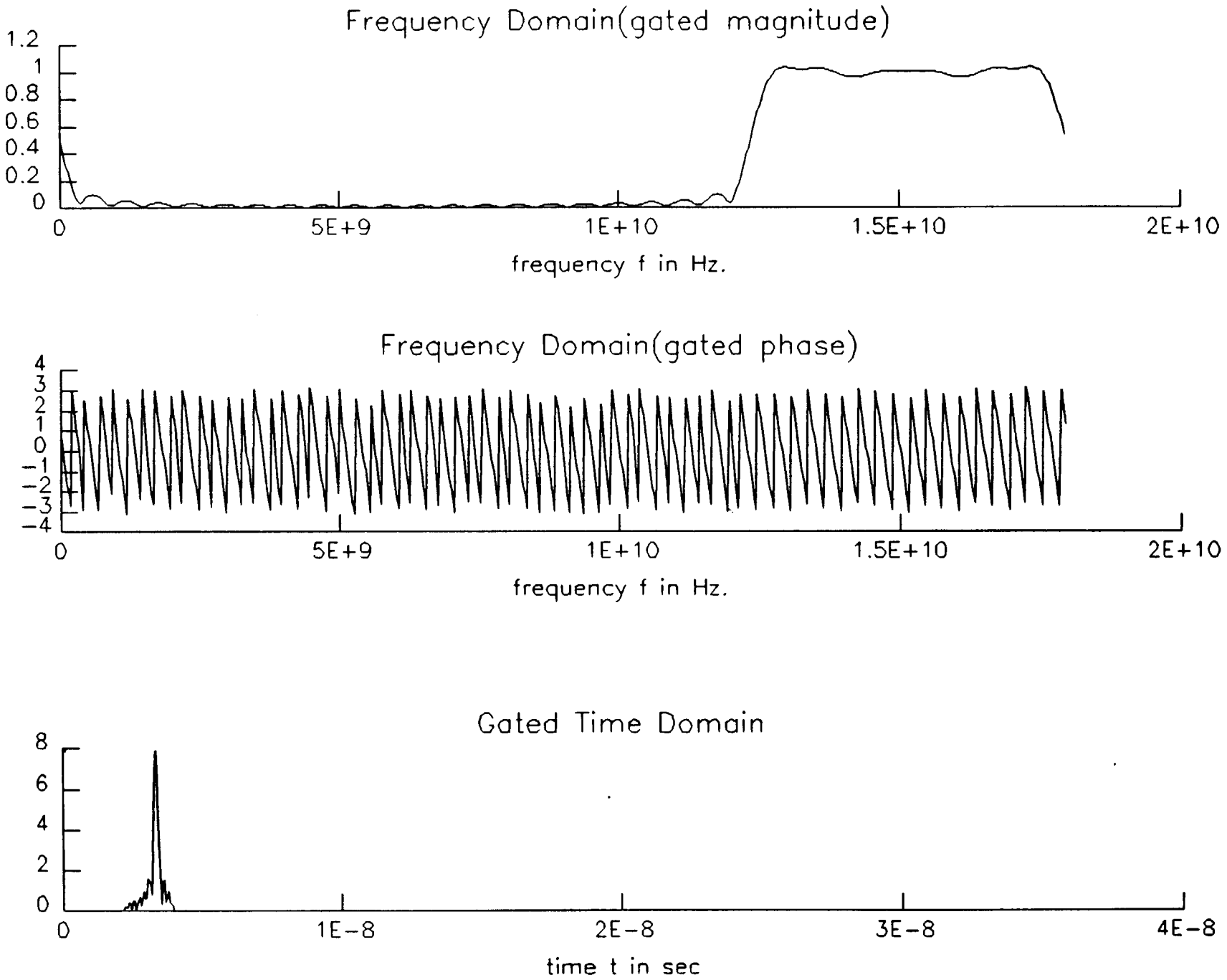

Figure 12: Errors introduced by time-gating(small gate)

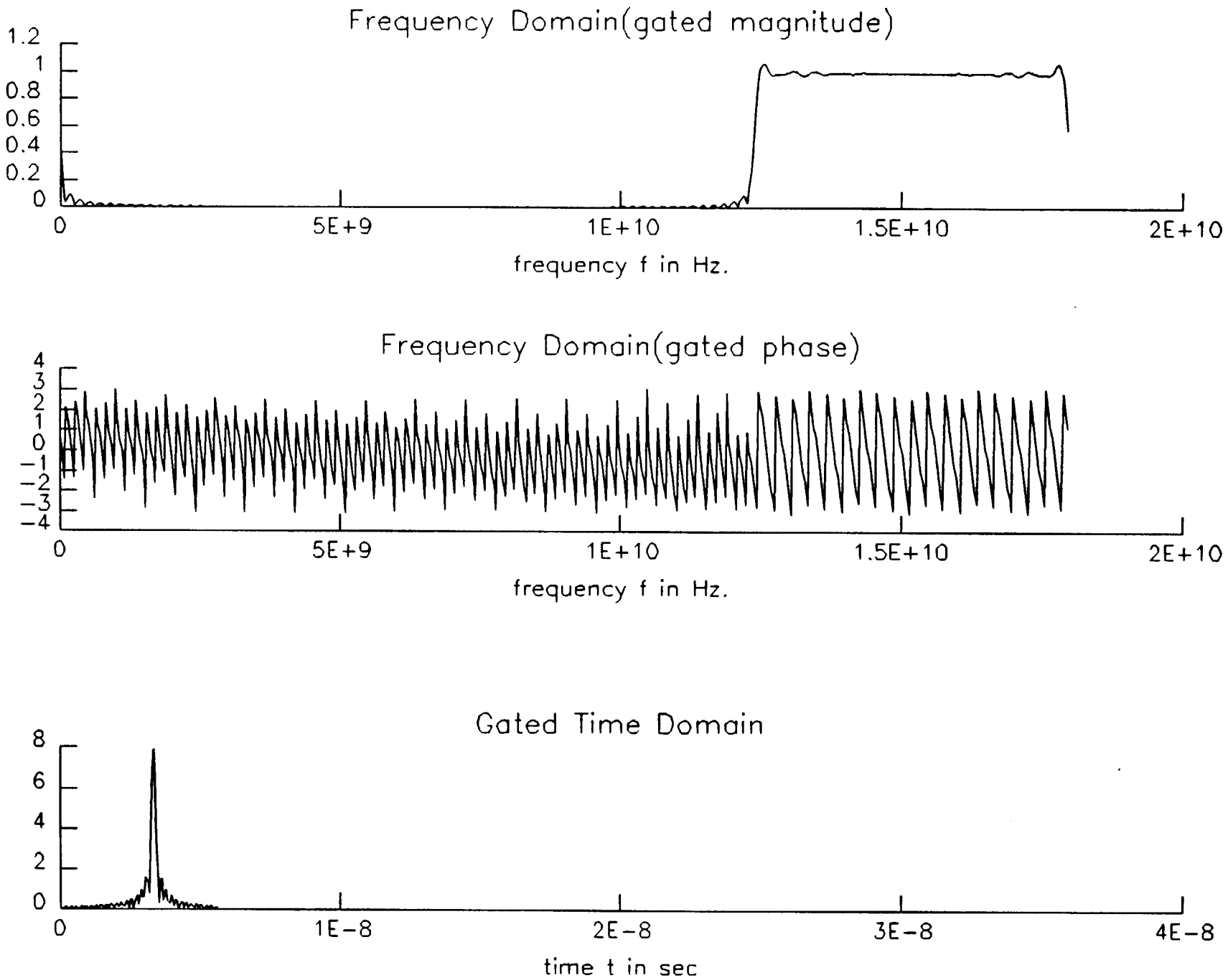

Figure 13: Errors introduced by time-gating(large gate)

APPENDIX 2.

1990 Review of Scientific Instruments Paper

Arcjet plasma plume effect on a microwave reflector antenna

B. W. Birkner, G. A. Hallock, H. Kim, and H. Ling
The University of Texas at Austin, Austin, Texas 78712

(Presented on 8 May 1990)

A configuration is described to measure the effect of the plasma produced by an arcjet thruster on a reflector antenna. The diagnostic consists of a small movable rf probe coupled to a Hewlett–Packard 8510 network analyzer. Because the perturbation is expected to be small ($< 10°$ phase shift), wall reflections are an important consideration. To minimize their effect we use Fourier transform gating techniques.

I. INTRODUCTION

The availability of large power supplies on the next generation of communication satellites has provided renewed interest in electric propulsion. An arcjet engine is one of the simplest devices, and current research indicates that specific impulse levels above 400 s are attainable,[1] making arcjets a very attractive candidate. The use of arcjet thrusters for station keeping and attitude control can potentially extend the lifetime of modern communication satellites up to ten years. This requires arcjets of the ~ 1 kW class, which is the focus of the work reported here. Higher power arcjets are also being developed for boosting satellites from lower Earth orbit to geosynchronous orbit. Again the fuel savings over conventional chemical propulsion are very large.

The arcjet produces a weakly ionized plasma during operation. For this technology to be usable on communication satellites, the signal degradation to and from the spacecraft due to refraction and attenuation of the microwave signals must be within acceptable limits. Since the satellites require totally uninterrupted operation, it is necessary to understand both steady-state and transient (startup and shutdown) operation of the thrusters.

A program of both modeling and laboratory experiments is required to establish arcjet compatibility with the microwave communications. Neither approach alone can predict the operation of an actual system with adequate confidence. Modeling relies on plasma parameters which are not accurately known, and is uncertain because of the difficulties inherent in wave propagation calculations. Experimental work is limited by the difficulty in laboratory simulation of the space environment, particularly boundary conditions, vacuum pressure, and wall reflections. In addition, accurate nonintrusive measurements of the plasma parameters are difficult.

II. PLUME MODELING AND RAY TRACING

The arcjet produces a weakly ionized plasma plume, which extends 10's of centimeters from the thruster nozzle. The cold plasma model provides a very good approximation to the electromagnetic behavior, with the index of refraction given by $N = \sqrt{1-\omega_p^2/\omega^2}$, where ω_p is the electron plasma frequency. The plasma frequency depends on the electron number density ($\omega_p^2 = n_e e^2/m_e \epsilon_0$), which has been experimentally measured by Carney using Langmuir probes in a laboratory facility.[2] The electron density is $\sim 10^{10}$ cm^{-3} close to the thruster nozzle, and is well modeled by a 1/(distance squared) falloff away from the nozzle times a factor giving exponentially decreasing density with angle away from the thruster axis.[3] A contour plot showing the measurement locations and a least-squares fit to the data is shown in Fig. 1. The microwave communication frequencies are typically only a factor of 2–20 above the plasma frequency close to the thruster, and therefore the plasma behaves as a very dispersive medium.

To study the effect of the plasma on the performance of on-board reflector antennas, the arcjet plume is modeled as an inhomogeneous scatterer with a smoothly varying refractive index. Since the plume size is the order of several wavelengths, geometrical optics is used to calculate the wave propagation. The trajectory, phase, amplitude, and polarization of the high-frequency ray field are computed numerically, based on the laws of geometrical optics.[4]

Once the ray optics field transmitted through the plume on the near-field aperture is found, the far-field pattern of the antenna can be calculated by its Fourier transform.[5] Two-dimensional calculations have been performed, and we are now extending our analysis to full 3-D geometry. Results indicate the plume can cause serious pointing errors, especially for very narrow beam antennas. Deterioration in both the main beam and sidelobes has been observed in the calculations.[6,7]

III. EXPERIMENTAL VALIDATION

Experimental verification of our calculated results is very important, because the geometrical optics assumptions which underlie the ray-tracing methods are not well satisfied by the plasma plume. We are therefore planning to experimentally measure the effect of the plume on the reflector antenna pattern. The issue for satellite communications is the plume effect on the far-field radiation pattern. This is difficult to simulate in the laboratory, however, particularly with the arcjet vacuum requirements. A near-field experiment is more appropriate, and also provides a very sensitive test of our code. If the near-field calculations are verified correct, then our far-field predictions should be very accurate.

The experimental configuration is shown in Fig. 2. A 40-cm-diam reflector antenna directs collimated radiation at 10 GHz through the plasma plume. The diagnostic consists of a small movable rf probe coupled to a Hewlett-

 0034-6748/90/102978-03$02.00

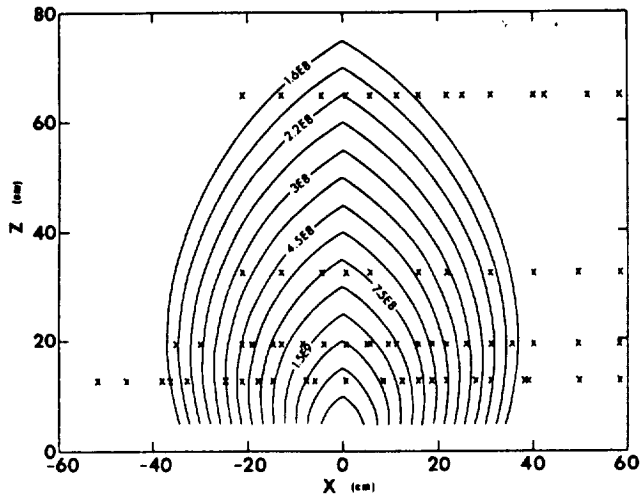

FIG. 1. Contour plot of the arcjet electron density profile. Measurement locations are denoted by ×. The contours are given by the least-squares fit $n_e = 9.1\times10^{11}\exp(-0.019\theta)/r^2\ \mathrm{cm}^{-3}$ (θ in degrees, r in cm).

Packard 8510 network analyzer. With the arcjet operating the antenna radiation is deflected upward, since the index of refraction is less than unity within the plasma. This changes both the magnitude and phase of the near-field distribution, as shown in Fig. 3. These calculations are for the probe location shown as a dotted line in Fig. 2, with $Y = 0$ referenced to the arcjet nozzle. The effect is relatively small, and concentrated toward the region closest to the plume. Here the maximum induced phase shift is ~8° and the magnitude change the order of 2.5 decibels.

The arcjet thruster requires a modest vacuum for operation, typically $\sim10^{-4}$ Torr. Microwave reflections, particularly from the wall behind the rf probe, are a considerable problem because of the relatively small tank dimensions (~1 m×1 m×1 m). Some attenuation will be obtained with vacuum compatible microwave absorbing material (Eccosorb FDS), which provides ~3 dB/mm attenuation at 3 GHz. The absorbing material will damp multiple reflections.

To eliminate primary reflections we will make use of the time domain gating feature of the HP8510 analyzer. In this technique measurements are made over a broad frequency range in the ac steady state, and Fourier transformed to the time domain. Gating can then be applied in the time domain to eliminate the reflections, since they are shifted in time by the extra path length traveled. The gated data are then transformed back into the frequency domain. Because the measurements do not extend to zero frequency ($\omega > \omega_p$), the FFT is performed over positive frequencies only. This operation preserves distinct time domain features (uniform response in the frequency domain transforms to a pulse in the time domain), although the time domain data are complex.

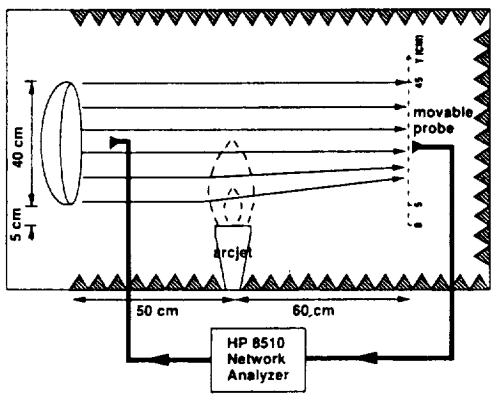

FIG. 2. Schematic of the measurement configuration, showing approximate ray trajectories in the presence of the plasma.

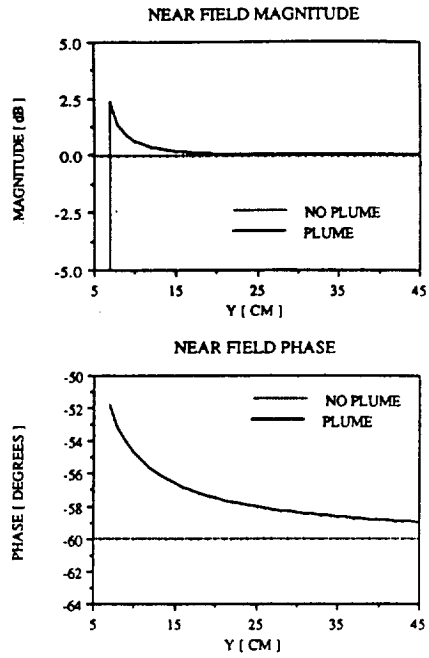

FIG. 3. Calculated near-field magnitude and phase (referenced to the antenna plane) with and without the plasma.

Several sources of error must be considered when using time gating.[8] The finite sampling used for the FFT causes aliasing if the extra path length for reflections is too large. If the path difference is too small, the reflections will not be time separated from the main signal (which is broadened by dispersion and the limited range of frequency measurements). Aliasing is not expected to be a problem, because of the small tank dimensions and use of some absorbing material. Separation of the reflections may be difficult, however.

The plasma is dispersive and distorts the transformed time domain pulse shape, complicating the task of time gating. A numerical simulation is shown in Fig. 4, where the frequency spectrum of the input signal is assumed to be Gaussian with a center frequency of 15 GHz and a FWHM of 2.94 GHz. The magnitude of the transformed pulse shape of the input signal is shown in Fig. 4(a). The corresponding FWHM of the pulse is 0.3 ns. The output of this signal after propagating through a homogeneous plasma slab of thickness $d = 20$ cm is computed, by assuming that each frequency component undergoes a phase shift of $-(\omega d/c)\sqrt{1-\omega_p^2/\omega^2}$. This is shown in Fig. 4(b) for different plasma frequencies. It is observed that as long as the frequency range of measurement is sufficiently above

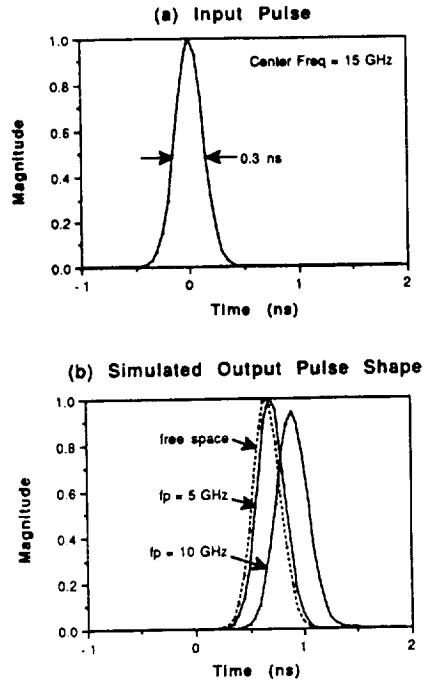

FIG. 4. Simulated time domain output of (a) the input pulse shape and (b) the output pulse shapes after propagation through a 20 cm plasma slab.

the plasma frequency, no significant pulse distortion will occur. The observed pulse delay is also not significant.

We have set up a test facility consisting of an antenna chamber, antennas, and HP8510 analyzer. We have verified basic system operation, using time gating on induced reflections. We have successfully compared predicted and measured effects of various dielectrics (such as paraffin) to high accuracy. Our current facility does not have vacuum capabilities, however. After completing this proof-of-principle work, we plan to set up the measurement configuration at NASA Lewis on their arcjet vacuum facility.[2] This is expected to begin during the summer of 1990.

IV. CONCLUSIONS

Electric satellite positioning and propulsion is now practical because of the substantial power supplies now designed into the spacecraft. One of the most critical issues for its use on communication satellites is the effect of the thruster plasma on microwave communication systems. We have done extensive modeling and analysis of this problem, and are now verifying this work experimentally.

ACKNOWLEDGMENTS

We would like to thank Dr. A. Zaman, Ms. L. Carney, Dr. F. Curran, and Dr. D. Byers for their strong support of this project. In addition, we would like to acknowledge Ms. Carney for supplying the plasma electron density measurements. This work is supported by the NASA Lewis Research Center under Cooperative Agreement NCC 3-127.

[1] S. C. Knowles, W. W. Smith, F. M. Curran, and T. W. Haag, AIAA Paper 87-1057, May 1987.
[2] L. M. Carney and J. M. Sankovic, NASA Tech. Mem. 102284 and AIAA-89-2723, AIAA/ASME/SAE/ASEE 25th Joint Prop. Conf., 1989.
[3] B. W. Birkner, MS thesis, The Univ. of Texas at Austin, Austin, TX, 1990.
[4] M. Kline and I. W. Kay, *Electromagnetic Theory and Geometrical Optics* (Wiley, New York, 1965).
[5] H. Ling, R. Chou, and S. W. Lee, IEEE Trans. Antennas Prop. AP-37, 194 (1989).
[6] H. Ling, G. A. Hallock, H. Kim, B. W. Birkner, and A. Zaman, Proc. 1989 Antenna Appl. Symposium, Allerton, IL, Sept. 1989.
[7] H. Ling, H. Kim, G. A. Hallock, B. W. Birkner, and A. Zaman, Proc. 1990 Int. IEEE Antennas and Prop. Soc. Symposium, Dallas, TX, May 1990.
[8] A. Henderson, J. R. James, P. Newham, and G. Morris, IEE Proc. 136, Pt. H, No. 4, 311 (1989).

APPENDIX 3.

1991 Transactions on Antennas and Propagation Paper (under review)

EFFECT OF ARCJET PLUME ON SATELLITE REFLECTOR PERFORMANCE

H. Ling, H. Kim, G. A. Hallock, B. W. Birkner and A. Zaman+

Department of Electrical and Computer Engineering
The University of Texas at Austin
Austin, TX 78712-1084

+ NASA Lewis Research Center
Cleveland, OH 44135

ABSTRACT

The effect of an arcjet plume on the performance of satellite reflector antennas is studied. The arcjet plume is modeled as a weakly ionized plasma. Spatial permittivity distribution of the plume is approximated using the available measurement data of the electron density profile and a cold plasma model. Geometrical optics is applied to determine the ray paths as well as the transmitted fields through the inhomogeneous plume. The ray optics results are compared against several exact solutions for scattering from inhomogeneous dielectrics and good agreement is observed for sufficiently large scatterer size. The far field antenna patterns of the reflector in the presence of the plume are calculated from the transmitted ray fields using a ray-tube integration scheme. For arcjet prototypes in the 1-kW class, the plume effect on the antenna performance is small. As the electron density increases (corresponding to higher arcjet power), a gradual degradation of the main beam and sidelobe level is observed. In addition, the main beam tends to squint away from the plume region.

This work is supported by the NASA Lewis Research Center under Cooperative Agreement NCC 3-127 and in part by the National Science Foundation under Grant ECS-8657524.

1. INTRODUCTION

An arcjet thruster is an electrothermal propulsion device being developed by NASA and the aerospace industry for stationkeeping and attitude control on future generation satellites. Because of its high efficiency, this device could potentially extend the lifetime of modern communication satellites up to ten years. The operating principle of the arcjet consists of heating a gas mixture (e.g., nitrogen-hydrogen) by means of a high temperature arc discharge. The heated propellant is then ejected through a nozzle to produce thrust. Recent arcjet research indicates that specific impulse levels well above 400 sec are attainable at the 1-kW level [1], making arcjets a very attractive candidate to replace the existing resistojet technology for auxiliary propulsion on satellites. One important issue which arises in the actual spacecraft integration of arcjet technology is the environmental impact of the arcjet plume, especially on microwave communication systems. The arcjet produces a weakly ionized plasma, which modifies the free space normally surrounding the satellite and causes refraction and attenuation of the microwave signals to and from the spacecraft. This is a primary user concern that must be addressed quantitatively before the arcjet technology can be fully accepted by the communication satellite industry.

In this paper, the effect of an arcjet plume on the performance of on-board reflector antennas is studied (Fig. 1). The arcjet plume is modeled as an inhomogeneous scatterer with a smoothly varying index of refraction. The spatial distribution of the refractive index is related to the measured electron density data [2] based on the cold plasma model. To study the propagation of the microwave signal through the inhomogeneous plasma plume, geometrical optics is used. Choosing geometrical optics to attack this problem is motivated by several considerations: (a) the plume size of interest is more than several wavelengths in extent, (b) the permittivity distribution of the plume is smoothly varying, and (c) a ray approach is compatible with existing reflector analysis codes. A "shooting and bouncing ray" (SBR) scheme, developed earlier for characterizing the radar cross section of engine inlets [3], is adopted in implementing the present analysis. A set of rays is shot from the

reflector aperture toward the plume. The trajectory, phase, amplitude and polarization of the high frequency ray field transmitted through the plume are computed numerically based on the laws of geometrical optics [4]. To validate the geometrical optics results, comparisons with several exact solutions to scattering from inhomogeneous dielectric bodies are made. Once the ray optics field transmitted through the plume is found on a near-field aperture, the far field performance degradation of the reflector in the presence of the plume can be fully characterized. Several plume-to-reflector configurations are studied. The resulting gain loss, pointing error and sidelobe degradation are crucial in determining realistic constraints on the location and maximum power output of the arcjet for spacecraft integration.

2. PLUME MODEL

Available experimental data taken from Langmuir probe measurements indicate that the arcjet plume consists of a weakly ionized plasma with electron density which varies as a function of the operating conditions and the distance from the nozzle [2]. The measured electron temperature of the plasma is well below 1 eV, indicating that a cold plasma model should be adequate in describing the plume. It is also estimated that both the collisional effect and the anisotropy due to the earth magnetic field are very small [5]. Therefore, the refractive index for this unmagnetized cold plasma depends only on the electron density and can be modeled as

$$N^2 = \frac{\varepsilon}{\varepsilon_0} = 1 - \frac{\omega_p^2}{\omega^2} \quad , \quad \omega_p^2 = \frac{n_e e^2}{m_e \varepsilon_0} \tag{1}$$

where ω_p is the plasma frequency and n_e is the electron density. From experimental data, the spatial distribution of the plume electron density is observed to obey approximately the functional form

$$n_e = \frac{a_1}{r^2} \exp(-\alpha\,\theta) \quad cm^{-3} \qquad (r \text{ in cm}, \theta \text{ in degrees}) \qquad (2)$$

where r is the distance from the nozzle and θ is measured from the plume center line along the x-axis (see Fig. 2(a)). Numerically, a_1 is equal to the on-axis electron density 1 cm away from the arcjet nozzle. It is a strong function of the arcjet power, but also depends on other parameters such as propellant type and mass flow rate. Typical values for the constants a_1 and α are found, through curve-fitting to experimental data, to be 3×10^{12} cm^{-1} and 0.03 deg^{-1}, respectively. A more detailed description of the curve-fitting algorithm to the experimental data can be found in [5]. Using the above values, contour plots of the relative dielectric constant are generated. Figs. 2(b) and 2(c) are the plume profiles at 3 GHz and 1 GHz, respectively. The contour levels are 0.02 apart with the outermost contour representing a relative dielectric constant of 0.98. Subsequent inner contours have decreasing dielectric constants. Very close to the nozzle, the dielectric constant can become negative due to the high electron density (and thus high plasma frequency) there. This corresponds to the cutoff for wave propagation ($\omega < \omega_p$). Comparing the two contour plots, we observe that the physical size of the plume increases as the frequency of the microwave signal is decreased. On the other hand, the electrical size of the plume (measured in terms of the free space wavelength) remains essentially independent of the frequency.

3. RAY TRACING THROUGH INHOMOGENEOUS PLUME

Once the plume model is established, geometrical optics is applied to calculate the propagation of the microwave signal through the plume. The solution of geometrical optics fields in an isotropic inhomogeneous medium was first derived by Luneburg more than thirty years ago and is documented in detail by Kline and Kay [4], Born and Wolf [6] and most recently, Bremmer and Lee [7]. Most numerical implementations of the ray solution for arbitrary media have been associated with studies of radio wave propagation in the ionosphere [8] and have not been widely reported in the antenna community. Senol and

Romine [9] used ray optics to study the effect of rocket plume on antenna performance, but their work was based on a scalar theory. Below the relevant equations for determining the ray trajectories as well as the associated phase, amplitude and polarization of the field along the ray are described. The detailed numerical implementation of these equations can be found in [10]. The trajectory of a ray in space is governed by the vector differential equation

$$\frac{d}{ds}\,(N\,\hat{t}\,) \;=\; \nabla N \qquad (3)$$

where $\hat{t}$ is a unit tangent vector of the ray at a point in space and the arclength s is measured along the curved ray trajectory (see Fig. 3). For an arbitrary inhomogeneous medium with index of refraction $N(\vec{r})$, the trajectory of a ray can be determined by solving the above equation numerically. For example, by finite differencing, we obtain the difference equation

$$N(\vec{r}+\Delta\vec{r})\,\hat{t}\,(\vec{r}+\Delta\vec{r}) = N(\vec{r})\,\hat{t}(\vec{r}) + \Delta s\;\nabla N(\vec{r}+\Delta\vec{r}/2\,) \qquad (4)$$

which allows us to solve for the subsequent ray trajectory once the initial direction $\hat{t}$ of a ray at point $\vec{r}$ is given. When the medium is homogeneous, the ray trajectory reduces to a straight line, as expected. From the above expression, we also observe that the ray trajectories are continuously being altered in the direction of the refractive index gradient. Therefore, the ray paths will tend to bend toward regions of higher refractive index. Since the refractive index of the plasma is always less than unity, it is expected that the rays will bend away from the plume.

Once the ray trajectory is determined, the phase variation along the ray path is given by Fermat's relationship:

$$[S(P_1) - S(P_2)] \;=\; \int_{P_1}^{P_2} N\;ds \qquad (5)$$

The complete geometrical optics field along the ray can also be determined. The field at point P_2 on the ray path is related to that at P_1 by the relationship

$$\vec{E}(P_2) = \hat{e}_2 \, E(P_1) \sqrt{N_1/N_2} \, (\mathbf{DF}) \, \exp\{-jk_0[S(P_2)-S(P_1)]\} \qquad (6)$$

The quantity **DF**, or the so-called divergence factor, can be interpreted physically as a factor which accounts for the spreading of the differential ray tube such that the energy carried by the ray tube remains constant (Fig. 3). The divergence factor is derivable from the first order transport equation and is given by

$$\mathbf{DF} = \exp\left\{ -\frac{1}{2} \int_{P_1}^{P_2} (\nabla \cdot \hat{t}) \, ds \right\} \qquad (7a)$$

or

$$\mathbf{DF} = \exp\left\{ -\frac{1}{2} \int_{P_1}^{P_2} \left(\frac{1}{R_1} + \frac{1}{R_2} \right) \, ds \right\} \qquad (7b)$$

where R_1 and R_2 are the two principal radii of curvature of the wavefront along the ray. Because of its simple geometrical interpretation, equation (7b) is better suited for numerical implementation of the divergence factor than (7a).

The polarization vector $\hat{e}_2$ is related to the polarization vector at P_1, $\hat{e}_1$, in the following manner:

$$\hat{e}_2 = \hat{n} \cos(\theta_0 - \hat{\theta}) + \hat{b} \sin(\theta_0 - \hat{\theta}) \qquad (8)$$

where

$$\theta_0 = \tan^{-1}\left(\frac{\beta_0}{\alpha_0}\right) \quad , \quad \hat{\theta} = \int_{P_1}^{P_2} \tau \, ds$$

$$\hat{e}_1 = \hat{n}\,\alpha_0 + \hat{b}\,\beta_0$$

and $$\tau = \frac{(\hat{t} \times \hat{t}') \cdot \hat{t}''}{|\hat{t} \times \hat{t}'|^2} \, .$$

In the above expressions, $\hat{n}$, $\hat{b}$ and $\hat{t}$ are respectively the normal, binormal and tangent vectors along the ray (see Fig. 4). τ is the "torsion" of the ray trajectory in space. It is a measure of the turning of the binormal vector. Note that the polarization vector depends on the torsion of the ray trajectory. For planar ray paths, the torsion is zero and therefore the electric field remains at a constant angle with respect to the normal and binormal vectors along the ray.

Based on the ray optics equations, a two-dimensional and a three-dimensional ray-tracing program have been developed for arbitrary inhomogeneous media. Results of the programs have been verified against the exact solution in "Maxwell's fisheye" which has a refractive index described by $N(r) = N_0 / [\ 1 + (r/a)^2\ ]$. The circular ray trajectories generated by the numerical routine agree very well with the exact solution. The divergence factor calculation is also checked against the exact solution derived by Bremmer and Lee [7] and found to be accurate. Shown in Fig. 5 is ray trajectory generated using the three-dimensional ray code for a "two-dimensional fisheye" medium which has refractive index profile $N(\rho) = N_0 / [\ 1 + (\rho/a)^2\ ]$. With a non-zero z-component in the initial ray direction, the ray trajectory spirals about the z-axis in a helix. Also shown as tick marks are the electric field vectors along the ray path.

4. VALIDATION OF RAY RESULTS

In order to validate the geometrical optics theory and its numerical implementation, several scattering problems are investigated. First, the two-dimensional scattering of a plane wave by an inhomogeneous circular cylinder with a continuous and radially-varying refractive index is considered (see Fig. 6). To establish a reference solution, the series expansion solution to scattering from a multi-layered circular cylinder [11] is implemented to approximate the exact solution. A smoothly varying refractive index profile

$$N(\rho) = \sqrt{\varepsilon_r(\rho)} = \begin{cases} \sqrt{b\,[1 - c\cos(\frac{\pi\rho}{a})]}\,, & \rho < a \\ 1\,, & \rho > a \end{cases} \qquad (9)$$

is chosen, where $b=[1+\varepsilon_r(0)]/2$ and $c=[1-\varepsilon_r(0)]/[1+\varepsilon_r(0)]$. To generate a numerical solution utilizing the two-dimensional ray tracing routine, a set of collimated rays from the incident plane wave direction are traced through the inhomogeneous dielectric. Shown in Fig. 7 is the ray trajectories inside the inhomogeneous cylinder for $\varepsilon_r(0)=0.5$. The rays tend to bend away from the center region which has a lower refractive index. Once the ray fields entering and exiting the scatterer are determined, the scattered far field can be found by carrying out the radiation integral one ray tube at a time. This "ray-tube integration" formulation is similar to those reported earlier [3],[12].

Figs. 8(a)-(d) are comparisons of the E-polarized scattering widths of a cylinder with $\varepsilon_r(0)=0.5$ calculated using the ray formulation and those obtained from the multi-layered solution for cylinders of different radii. Ten layers per wavelength is used in the multi-layered solution in order to simulate a smooth refractive index profile. It is observed that for scatterer diameter above 3 free space wavelengths, the agreement between the two results is very good in the forward scattering region. This is as expected since the geometrical optics theory should become more accurate as the frequency is increased. For angles far away from the forward($\phi=0°$) direction, the exact solution is more than 30 dB below the forward scattering strength. In this region, the accuracy of the ray results is limited by the numerical noise floor arising from the finite ray density used in the calculation. The same comparisons can be made for the H-polarized case. In fact, based on the ray formulation, it can be shown that the scattering pattern of the H-polarization is identical to that of the E-polarized case. From the exact solution, it is also found that as the scatterer size is increased beyond 3 λ, the scattering widths of the two polarizations become essentially identical. This is consistent with the commonly held notion that the scattering

pattern is not very sensitive to polarization in the high frequency regime. Fig. 9 shows the comparison of the scattering widths of a cylinder of diameter 6 λ calculated using the ray approach and those obtained from the multi-layered solution for $\epsilon_r(0)=3.0$. In this case the rays are attracted toward the center and caustic points exist inside the cylinder. Again the ray results agree very well with the multi-layered solution.

Next, the scattering from an inhomogeneous sphere is carried out as a three-dimensional validation example. A refractive index profile similar to (9) is chosen, except that the variable ρ is replaced by the three-dimensional radial varible r in the expression. The series expansion solution to scattering from a multi-layered sphere [13] is implemented to approximate the exact solution to the problem. The ray optics results are generated from the three-dimensional ray tracing code and a three-dimensional ray-tube integration scheme similar to that used in the two-dimensional case. The comparisons between the two results for a sphere of diameter 6 λ are shown in Figs. 10(a) and 10(b) for $\epsilon_r(0)=0.5$ and 3.0, respectively. Agreement between the ray results and the multi-layered solution is consistent with the two-dimensional cases.

5. REFLECTOR PERFORMANCE DEGRADATION

With the ray optics method validated, the effects of the arcjet plume on reflector performance are investigated. (Some preliminary results have been reported earlier in [14] and [15]). Shown in Fig. 11(a) is the three-dimensional geometry of the case under study. The reflector is assumed to have a diameter of 60 cm (20 λ at 10 GHz) and a 10-dB aperture edge taper. The initial ray bundle after reflection from the reflector surface is assumed to be perfectly collimated and has perfect linear polarization in the y-direction. Also shown in the figure are ray trajectories through a plume with parameter $a_1=1\text{x}10^{14}$ cm^{-1}. As expected the rays tend to bend away from the high electron density region near the nozzle. The direction, phase, amplitude and polarization of the ray field transmitted through the plume are computed on an exit aperture plane $z_a=50$ cm. The far field of the

reflector in the presence of the plume can be related to the transmitted field on the aperture plane through the standard radiation integral as follows:

$$\vec{E} = \frac{e^{-jkr}}{r} \left(\hat{\theta} A_\theta + \hat{\phi} A_\phi \right) \tag{10}$$

$$\begin{bmatrix} A_\theta \\ \\ A_\phi \end{bmatrix} = \left(\frac{jk}{4\pi}\right) \int \int_{z=z_a \text{ plane}} \exp[\, jk\, (\cos\phi \sin\theta\, x + \sin\phi \sin\theta\, y + \cos\theta\, z_a)]\; dxdy$$

$$\cdot \left\{ \begin{bmatrix} -\hat{\phi} \\ \\ \hat{\theta} \end{bmatrix} \times \vec{E}\,(\vec{r}) + \eta \begin{bmatrix} \hat{\theta} \\ \\ \hat{\phi} \end{bmatrix} \times \vec{H}\,(\vec{r}) \right\} \cdot \hat{z}$$

To evaluate the above aperture integral, we follow a "ray-tube integration" procedure similar to those used in Sec. 4 and sum up the contributions from all rays arriving on the aperture [3], [12]. Carrying out the ray-tube integration over the aperture plane results in

$$A_{\theta,\phi} = \left(\frac{jk}{4\pi}\right) \sum_{\text{ith ray}} (\text{Area})_{\text{proj}}\; \exp[\, jk(\cos\phi \sin\theta\, x_i + \sin\phi \sin\theta\, y_i + \cos\theta\, z_a)]$$

$$\cdot B_{\theta,\phi} \cdot S(\theta, \phi) \tag{11}$$

where

$$B_\theta = [\, \sin\phi\, E_{y,i} + \cos f\, E_{x,i}\,] + \eta\, [\, \cos\theta \cos\phi\, H_{y,i} - \cos\theta \sin\phi\, H_{x,i}\,]$$

$$B_\phi = [\, \cos\theta \cos\phi\, E_{y,i} - \cos\theta \sin\phi\, E_{x,i}\,] + \eta\, [\, -\sin\phi\, H_{y,i} - \cos\phi\, H_{x,i}\,]$$

$$S(\theta, \phi) = \frac{2J_1(u)}{u} \quad , \quad u = ka\sqrt{(\cos\phi \sin\theta - t_x)^2 + (\sin\phi \sin\theta - t_y)^2}$$

$(\text{Area})_{\text{proj}} = \pi a^2 = \dfrac{(\text{Area})_{\text{in}}}{|DF|^2} \left(\dfrac{1}{t_z}\right)$ = the projected area of the ray tube on the aperture plane,

$(\text{Area})_{in}$ is the initial ray tube size before the plasma.

In deriving (11), we have assumed that the ray direction is given by $\hat{t} = t_x \hat{x} + t_y \hat{y} + t_z \hat{z}$, and that the magnetic field is related to the electric field through $\vec{H} = (\hat{t} \times \vec{E}) / \eta$.

The reflector patterns along the two principal planes for the geometry in Fig. 11(a) are computed and plotted in Figs. 11(b) and (c). Small but noticeable degradations in the main beam and the sidelobe regions are observed. In particular, the main beam is found to squint away from boresight in the H-plane. This effect can be interpreted physically if we ignore, to the first order, the refraction of the rays through the plume. We can then argue that the rays traveling closer to the nozzle must experience a smaller total phase shift than those farther away from the nozzle due to the lower permittivity of the inner plume region. Consequently, the transmitted field on the exit aperture $z=z_a$ has a tilted phase distribution which leads to the main beam squinting away from the plume region. In this example, the beam (beamwidth=3.0°) experiences a 0.75° (0.25 BW) beam squint away from the boresight. This translates into a 0.94 dB gain loss. For very narrow beam antennas, this effect could become more serious. The E-plane pattern in Fig. 11(c) shows a higher sidelobe level than the H-plane pattern, and a noticeable cross polarization level due to the plume. Figs. 12(a) and (b) show the reflector far-field patterns under a higher power arcjet operating condtion ($a_1=3\text{x}10^{14}$ cm^{-1}). The deterioration of the reflector performance is more severe. The beam squint and boresight gain loss are respectively, 1.5° and 4.84 dB. Finally, it is worth noting that the values of a_1 used in the above examples are significantly higher than the measurements reported in [2]. These larger values, through extrapolation of the experimental data, should correspond to arcjets operating in the 3-kW range. For $a_1=3\text{x}10^{12}$ cm^{-1}, corresponding to the 1-kW class laboratory prototypes used in [2], the reflector pattern degradation is very small.

Next, a different plume configuration is studied where the plume is oriented horizontally along the y-axis and the nozzle position is located at (x=0, y=-30 cm, z=0), as

shown in Fig. 13(a). The reflector geometry and the arcjet power are kept identical to those of Fig. 12. The reflector patterns in the two principal planes are plotted in Figs. 13(b) and (c). In this case, the plume distribution has no symmetry along either the H- or the E-plane of the reflector and the beam squint phenomenon can be observed in both planes. In the H-plane, the beam squints toward the $+\theta$ direction, as expected. In the E-plane, it may first appear that the beam should squint away from the nozzle and toward the $+\theta$ direction. However, closer examination of the plume profile reveals that there is more plume blockage in the $y>0$ half of the aperture. Therefore, the beam squints toward the $-\theta$ direction. The gain loss at the boresight is 1.18 dB. By comparing the antenna patterns in Fig. 12 to those in Fig. 13, we notice that the overall pattern degradation is much less severe in the case presented in Fig. 13. We therefore conclude that the plume effect on reflector performance is strongly dependent on the actual plume-to-reflector configuration.

6. SUMMARY

The effect of an arcjet plume on the performance of satellite reflector antennas has been investigated. The arcjet plume is modeled as a weakly ionized plasma. Spatial permittivity distribution of the plume is approximated based on the cold plasma model and the available measurement data of the electron density profile. Geometrical optics is applied to determine the ray path as well as the transmitted field strength through the inhomogeneous plume. The scattered fields calculated from geometrical optics have been verified against the multi-layered solutions to radially inhomogeneous two-dimensional cylinders and three-dimensional spheres. The far field patterns of the reflector in the presence of the plume have been computed for various cases and the resulting degradations have been studied. As the electron density is increased (corresponding to higher arcjet power), a gradual degradation of the reflector pattern is observed. The most significant and interesting effect is a beam squinting phenomenon which results in antenna gain loss and pointing error. The amount of degradation is also shown to be strongly dependent on the

plume-to-reflector configuration. The capabilites developed in this work can be applied to model more realistic antenna configurations on satellites. The quantitative information generated will be crucial in determining realistic constraints on the location and maximum power output of the arcjet for spacecraft integration.

ACKNOWLEDGMENTS

The authors would like to thank L. M. Carney for supplying the electron density measurements used in this work and for helpful discussions on the plume characteristics.

REFERENCES

[1] S. C. Knowles, W. W. Smith, F. M. Curran and T. W. Haag, "Performance characterization of a low power hydrazine arcjet," AIAA paper 87-1057, May 1987.

[2] L. M. Carney, "An experimental investigation of an arcjet thruster exhaust using Langmuir probes," NASA Technical Memo 100258, Dec. 1988.

[3] H. Ling, R. Chou and S. W. Lee, "Shooting and bouncing rays: Calculating the RCS of an arbitrarily shaped cavity," *IEEE Trans. Antennas Propagat.*, vol. AP-37, pp. 194-205, Feb. 1989.

[4] M. Kline and I. W. Kay, *Electromagnetic Theory and Geometrical Optics*, Wiley, New York, 1965, Chap. 5.

[5] B. J. Birkner, "Modeling of a low-power arcjet thruster plasma plume for geometrical optics ray tracing," M.S. thesis, Univ. of Texas at Austin, August 1990.

[6] M. Born and E. Wolf, *Principles of Optics*, MacMillan, New York, 1964, Chap. 3.

[7] H. Bremmer and S. W. Lee, "Propagation of a geometrical optics field in an isotropic inhomgeneous medium", *Radio Sci.*, vol. 19, pp. 243-257, 1984

[8] K. G. Budden, *The Propagation of Radio Waves*, Cambridge, London, 1985, Chap. 14.

[9] A. J. Senol and G. L. Romine, "Three-dimensional refraction-diffraction of EM waves through rocket exhaust plumes," AIAA paper 84-1597, June 1984.

[10] H. Ling, G. A. Hallock, H. Kim and B. W. Birkner, "Near field interaction of microwave signals with a bounded plasma plume," Annual Report for NASA Grant NCC3-127, Jan. 1990.

[11] H. E. Bussey and J. H. Richmond, "Scattering by a lossy dielectric circular cylindrical multilayer -- numerical values," *IEEE Trans. Antennas Propagat.*, vol. AP-23, pp. 723-725, Sept. 1975.

[12] S. W. Lee, H. Ling and R. Chou, "Ray-tube integration in shooting and bouncing ray method," *Microwave Opt. Tech. Lett.*, vol. 1, pp. 286-289, Oct. 1988.

[13] J. R. Wait, "Electromagnetic scattering from a radially inhomogeneous sphere," *Appl. Sci. Res.*, series B, vol. 10, pp. 441-449, 1963.

[14] H. Ling, G. A. Hallock, H. Kim, B. W. Birkner and A. Zaman, "Reflector performance degradation due to an arcjet plume," *Proceedings of the 1989 Antenna Applications Symposium*, Allerton, IL, Sept. 1989.

[15] H. Ling, H. Kim, G. A. Hallock, B. W. Birkner and A. Zaman, "Effect of arcjet plume on satellite reflector performance," *1990 IEEE Antennas and Propagat. Symposium Digest.*, Dallas, TX, pp. 1876-1879, May 1990.

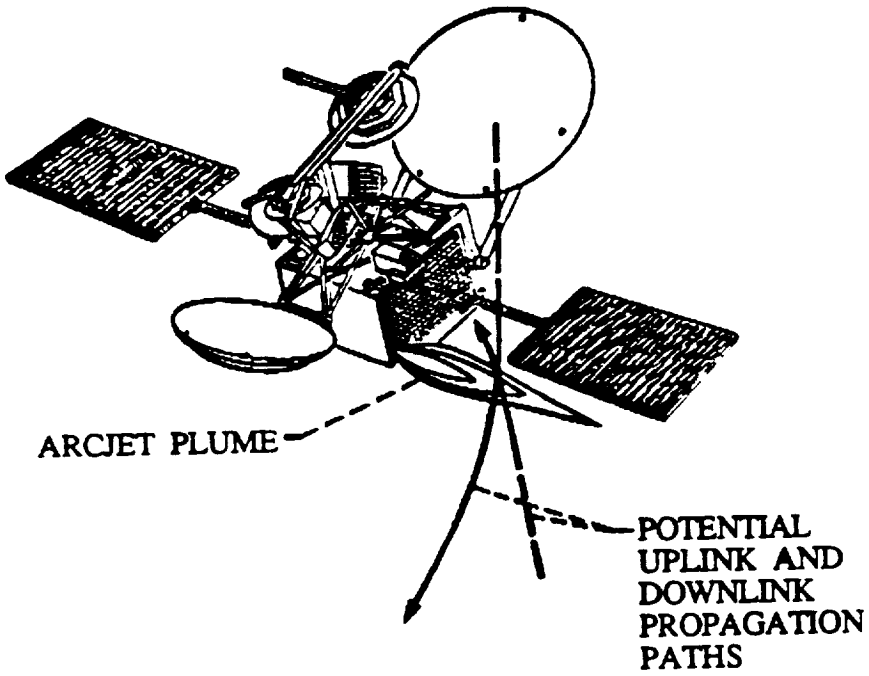

Fig. 1. Reflector performance degradation due to an arcjet plume.

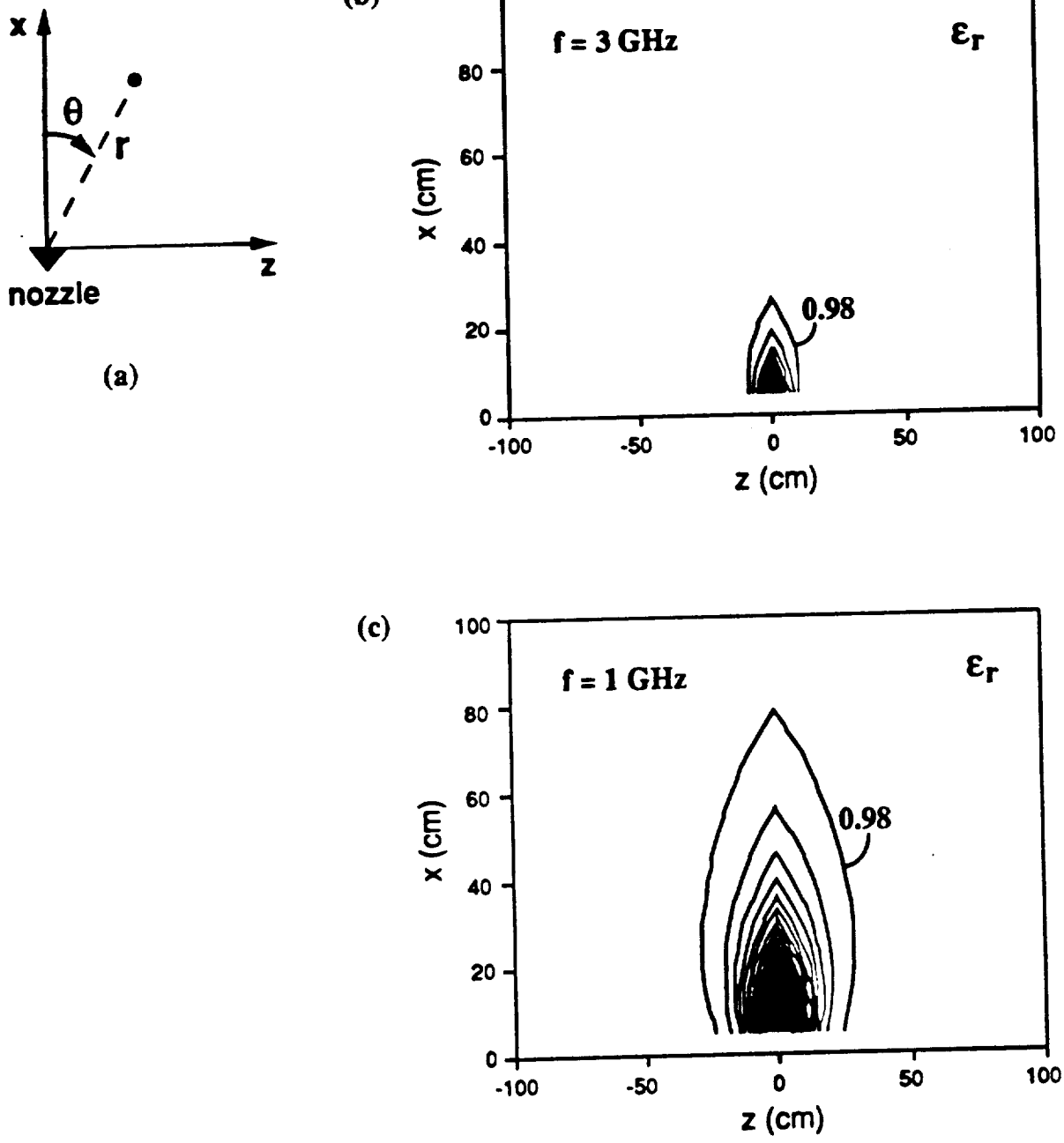

Fig. 2. (a) Coordinate geometry for describing the plume. (b) Relative dielectric constant profile of the plume at 3 GHz, and (c) 1 GHz. The contour levels are 0.02 apart.

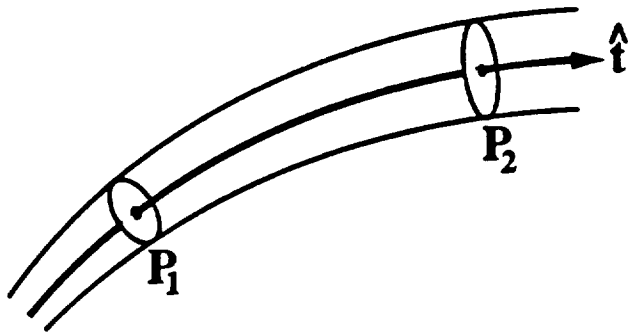

$$|DF|^2 = \frac{\text{Differential Ray Tube Area at } P_1}{\text{Differential Ray Tube Area at } P_2}$$

Fig. 3. Curved ray trajectory in an inhomogeneous medium. Ray tube spreading is accounted for by the divergence factor (DF).

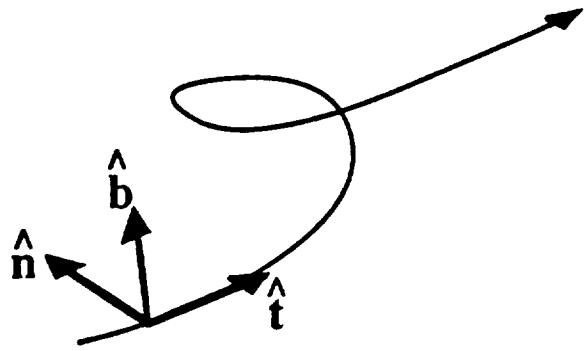

Fig. 4. Three unit vectors $\hat{n}$ (normal), $\hat{b}$ (binormal) and $\hat{t}$ (tangent) can be defined along the ray trajectory in space.

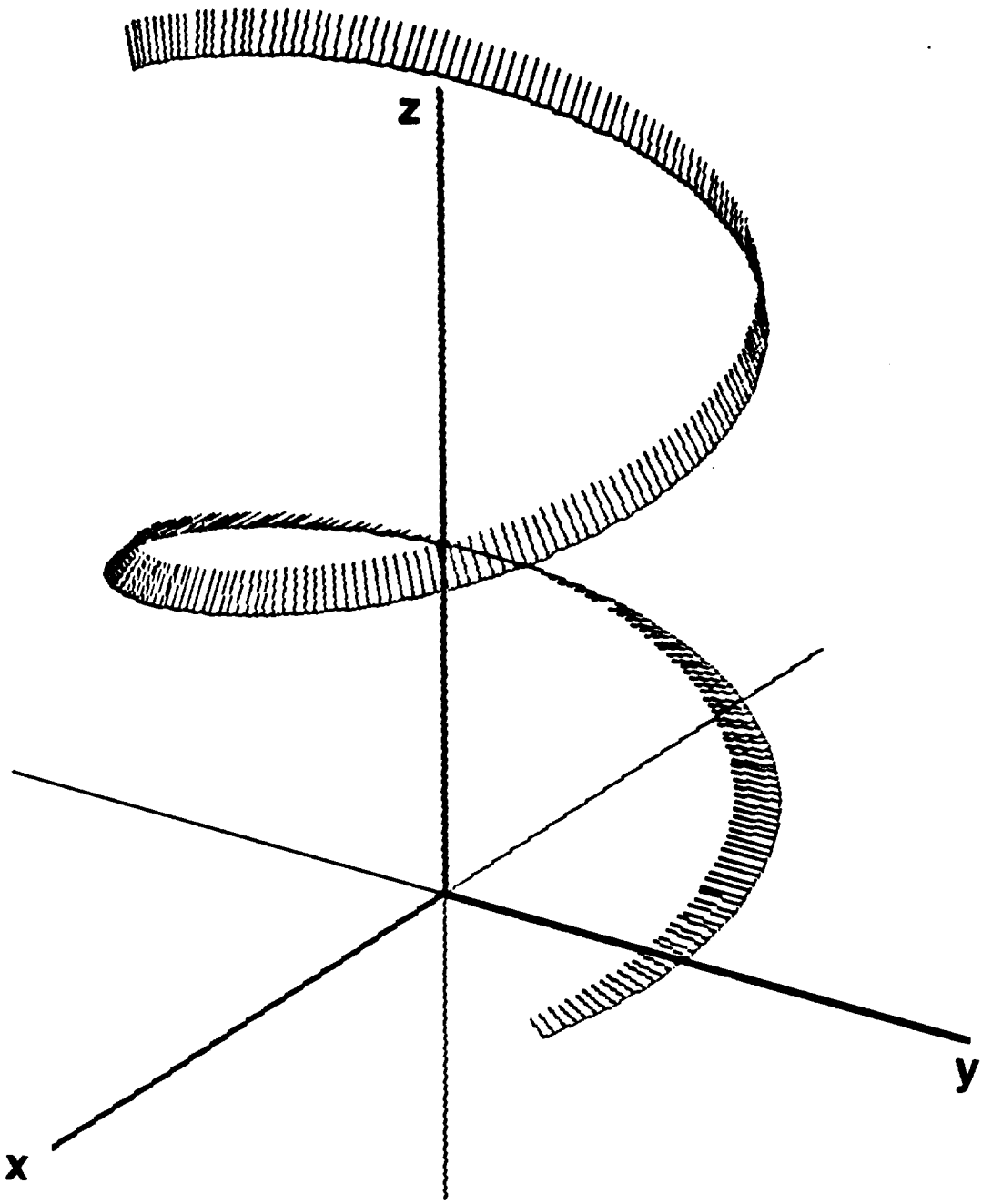

Fig. 5. Helical ray trajectory in a two-dimensional Maxwell's fisheye medium. The tick marks are the electric field vectors along the ray.

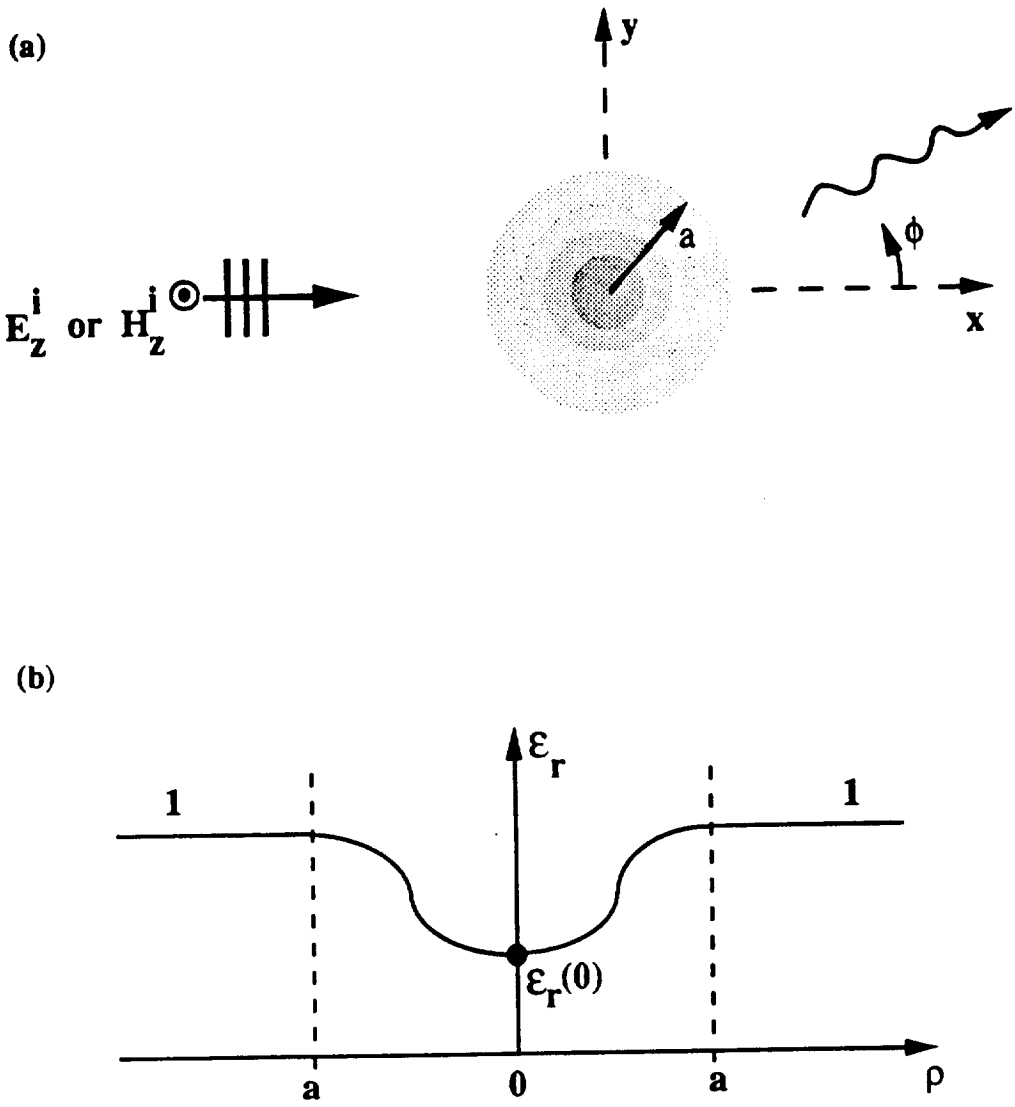

Fig. 6. Two-dimensional scattering of a plane wave by an inhomogeneous circular cylinder. (a) Problem geometry. (b) Refractive index profile.

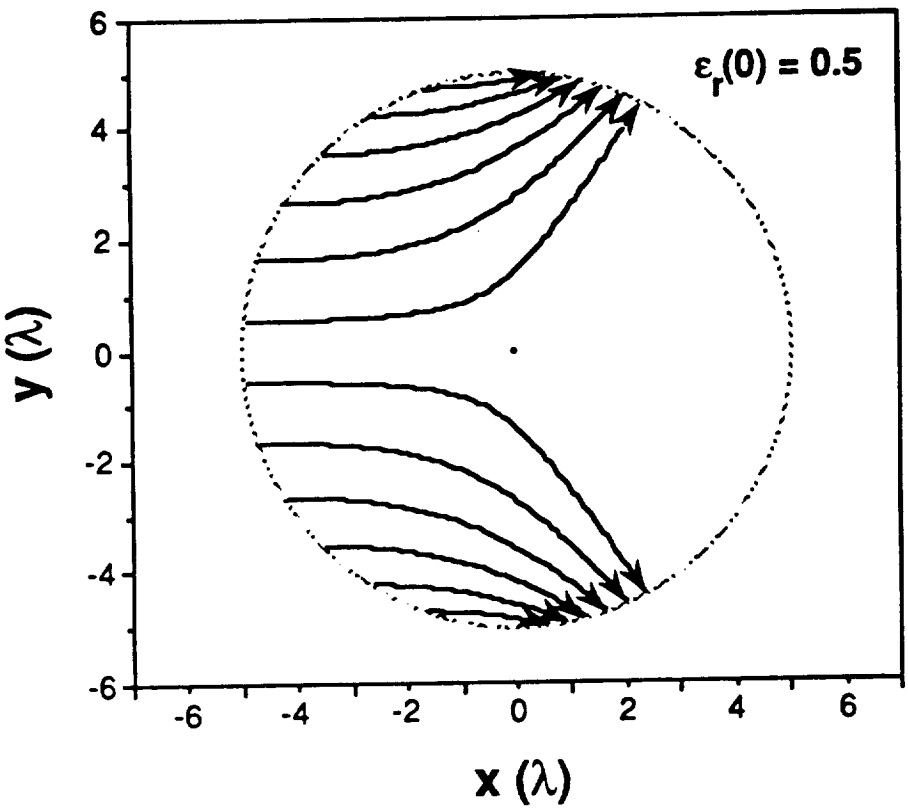

Fig. 7. Ray trajectories inside an inhomogeneous dielectric cylinder with diameter 10 λ and $\varepsilon_r(0)$=0.5.

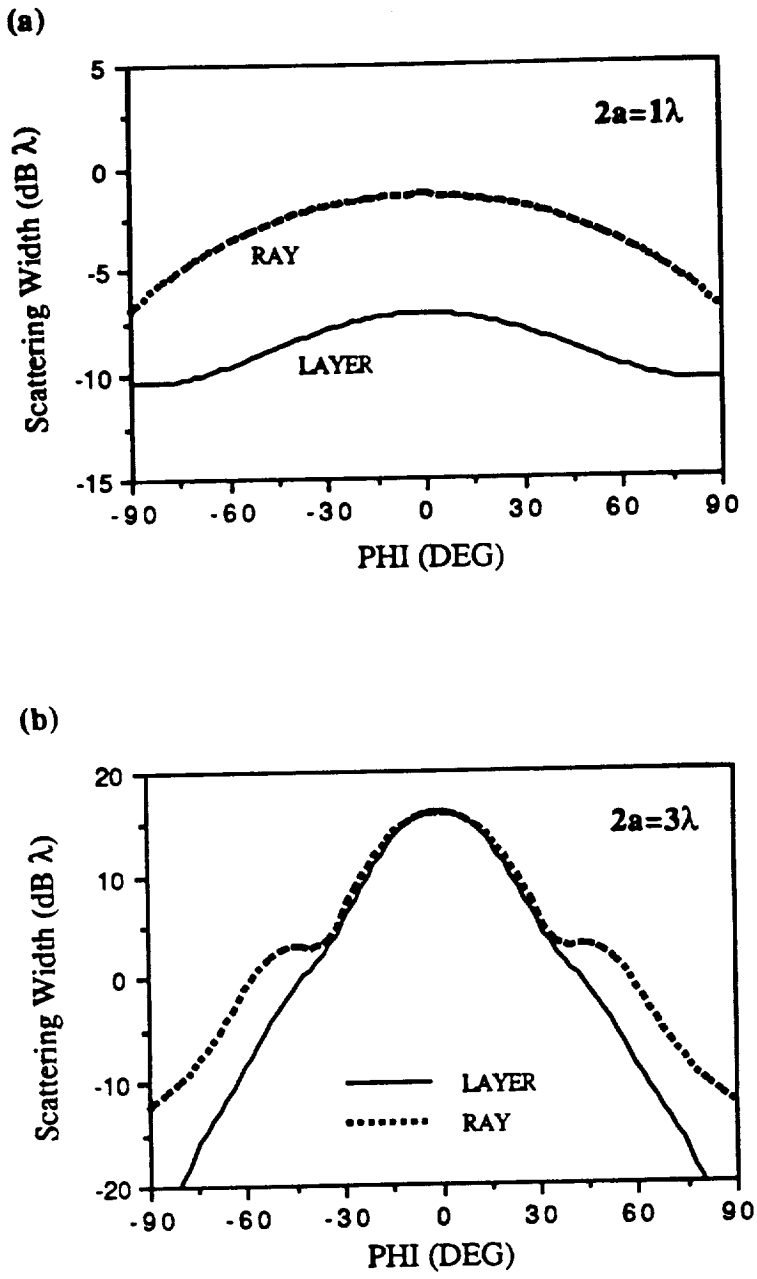

Fig. 8. Comparison of the scattering width of an inhomogeneous cylinder with $\varepsilon_r(0)=0.5$ calculated using ray optics and that obtained from the multi-layered solution. (a) $2a = 1\lambda$. (b) $2a = 3\lambda$.

(c)

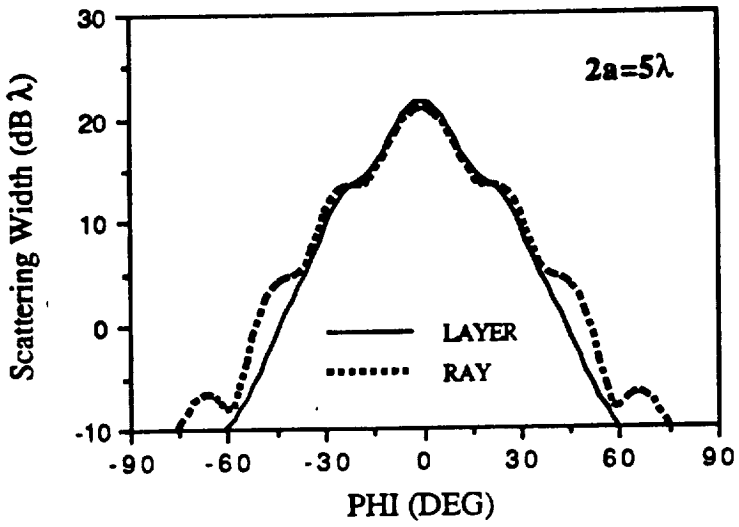

(d)

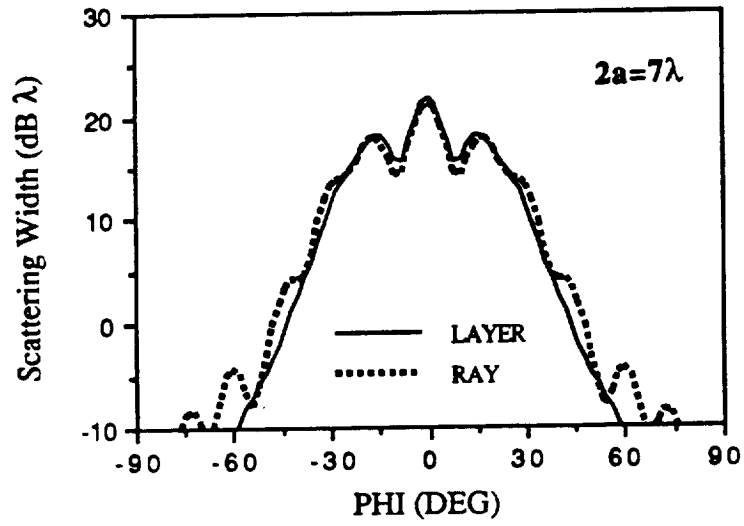

Fig. 8(Cont'd). (c) $2a = 5\lambda$. (d) $2a = 7\lambda$.

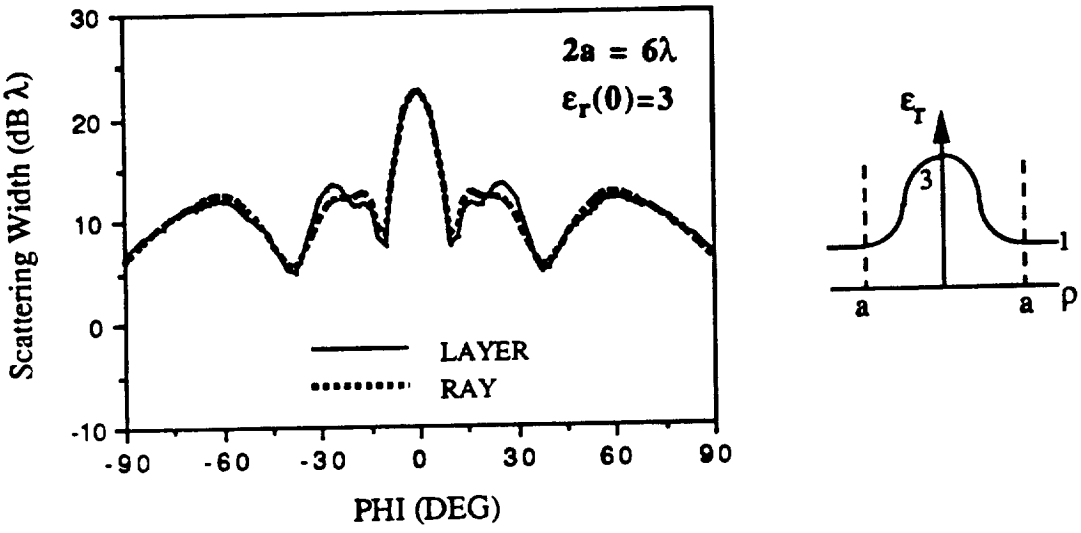

Fig. 9. Comparison of the scattering width of an inhomogeneous cylinder with $2a = 6\lambda$ and $\varepsilon_r(0)=3.0$ calculated using ray optics and that obtained from the multi-layered solution.

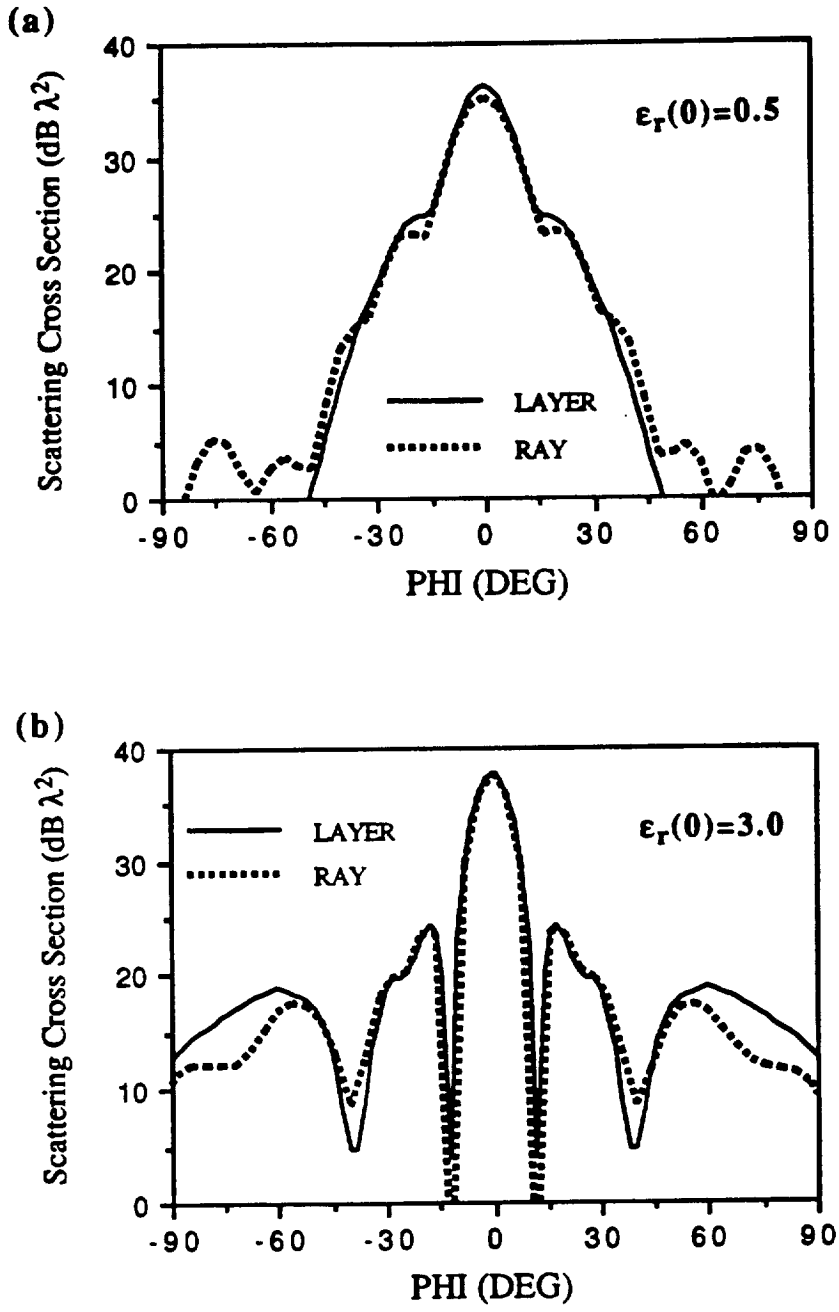

Fig. 10. Comparion of the scattering cross section of an inhomogeneous sphere of diameter 6λ calculated using ray optics and that obtained from the multi-layered solution. (a) $\varepsilon_r(0)=0.5$. (b) $\varepsilon_r(0)=3.0$.

(a)

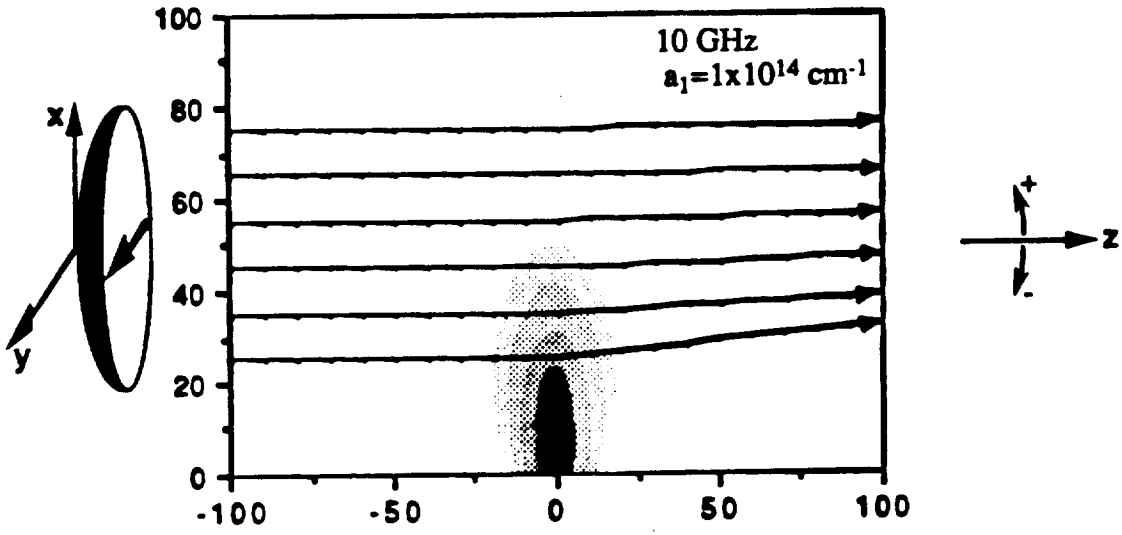

Fig. 11. Reflector pattern degradation due to a plasma plume (a_1=1x10^{14} cm^{-1}). (a) Reflector and plume configuration. The reflector has a diameter of 60 cm (20λ at 10 GHz) and an assumed aperture taper of 10 dB. The polarization is linear in y. (b) H-plane pattern. (c) E-plane pattern.

(b)

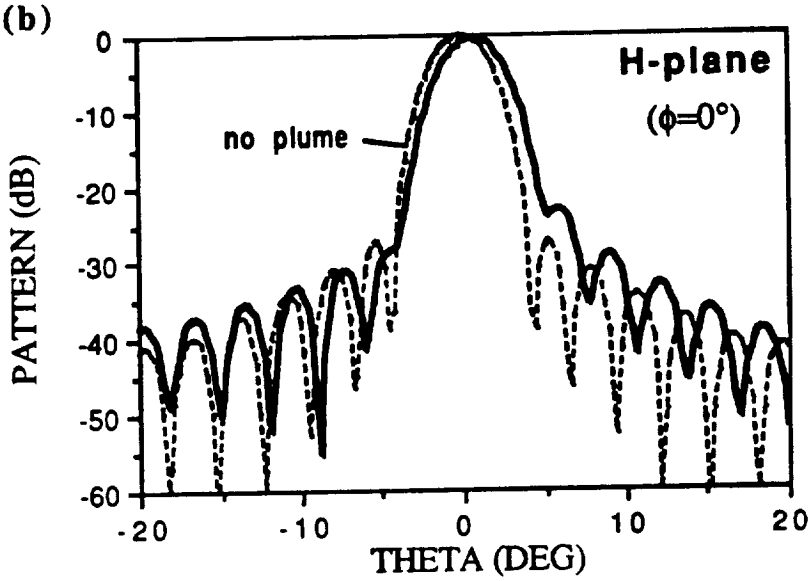
H-plane
(ϕ=0°)
no plume
PATTERN (dB)
0
-10
-20
-30
-40
-50
-60
-20
-10
0
10
20
THETA (DEG)

(c)

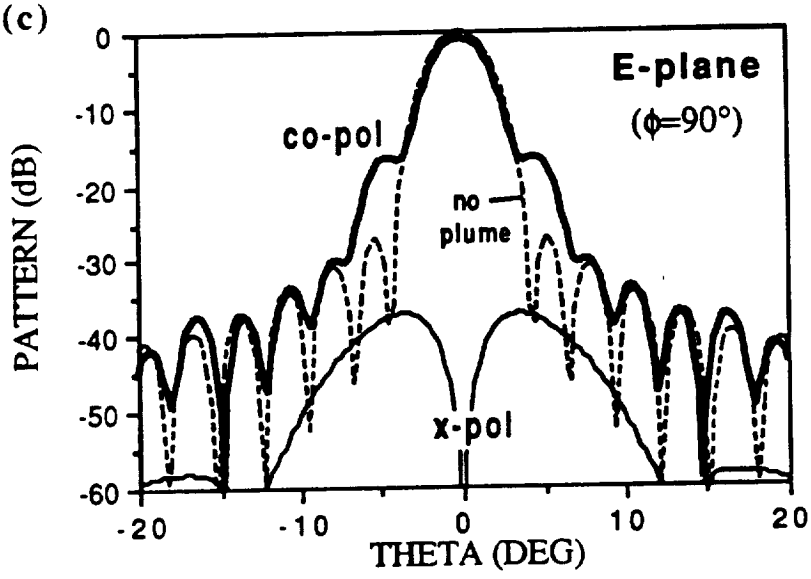
E-plane
(ϕ=90°)
co-pol
no
plume
x-pol
PATTERN (dB)
0
-10
-20
-30
-40
-50
-60
-20
-10
0
10
20
THETA (DEG)

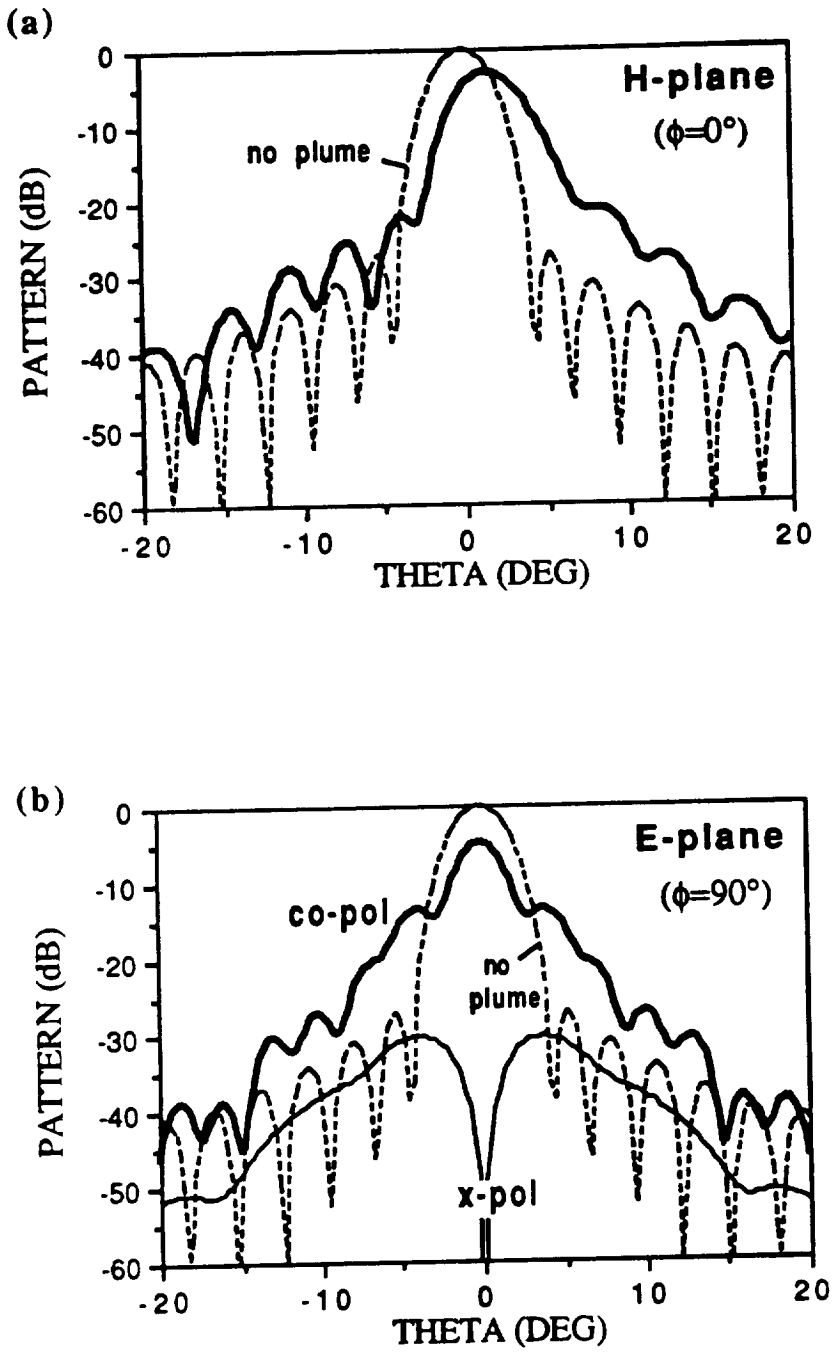

Fig. 12. Reflector pattern degradation due to a higher power arcjet plume (a_1=3x10^{14} cm^{-1}). (a) H-plane pattern. (b) E-plane pattern.

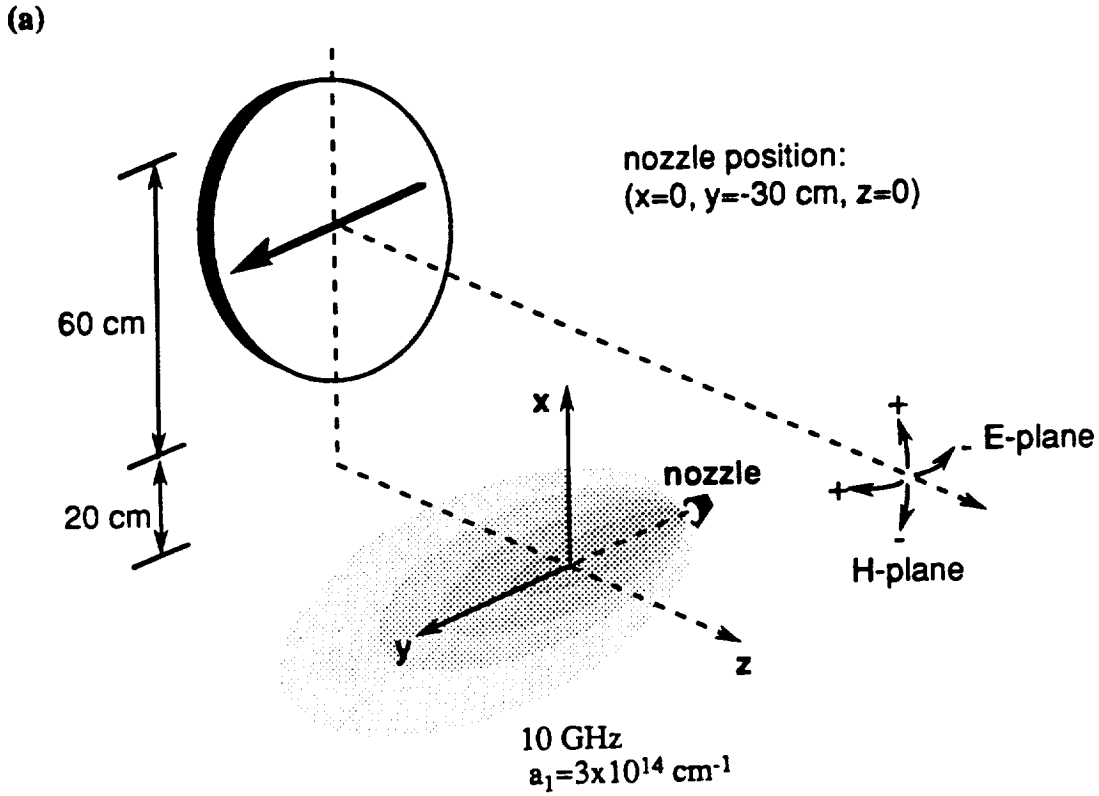

Fig. 13. Reflector pattern degradation due to a different plasma plume configuration with a_1=3x10^{14} cm^{-1}. (a) Reflector and plume geometry. The reflector has a diameter of 60 cm (20λ at 10 GHz) and an assumed aperture taper of 10 dB. The polarization is linear in y. The plume is oriented horizontally along y and the nozzle position is located at (0, -30cm, 0). (b) H-plane pattern. (c) E-plane pattern.

(b)

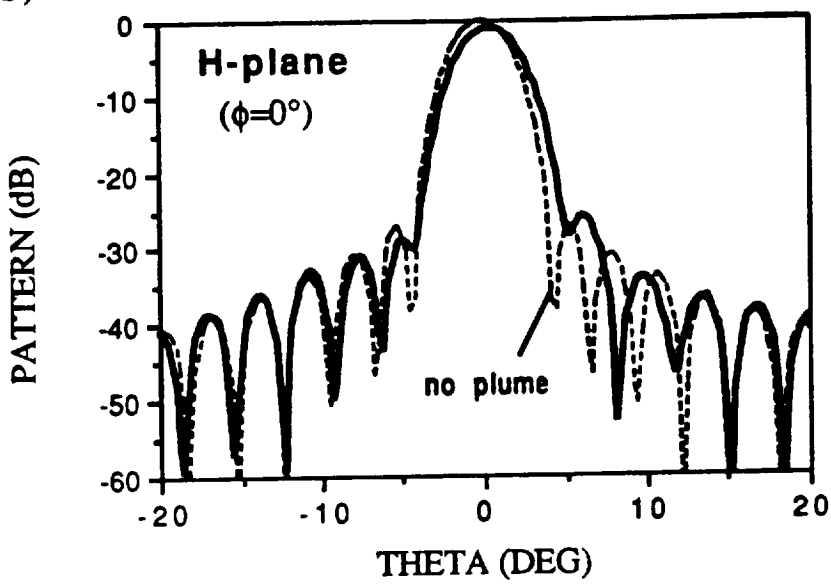
H-plane
(ϕ=0°)
no plume
PATTERN (dB)
THETA (DEG)
0
-10
-20
-30
-40
-50
-60
-20
-10
0
10
20

(c)

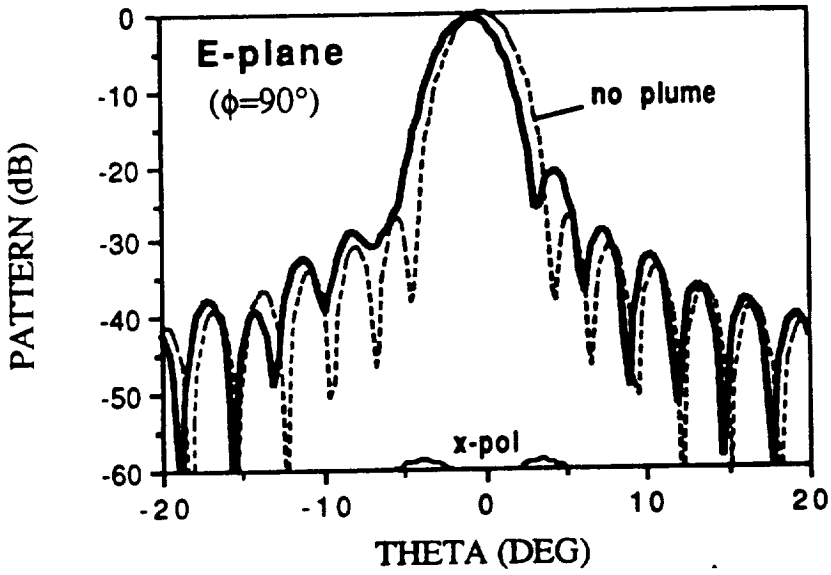
E-plane
(ϕ=90°)
no plume
x-pol
PATTERN (dB)
THETA (DEG)
0
-10
-20
-30
-40
-50
-60
-20
-10
0
10
20

APPENDIX 4.

1991 Transactions on Antennas and Propagation Paper (to be submitted)

HIGH FREQUENCY ELECTROMAGNETIC SCATTERING FROM AN INHOMOGENEOUS DIELECTRIC BODY BY RAY TRACING

Hyeongdong Kim and Hao Ling

Department of Electrical and Computer Engineering
The University of Texas at Austin
Austin, TX 78712-1084

Abstract - A ray formulation is presented for treating the electromagnetic scattering from electrically large, inhomogeneous objects. A dense grid of rays representing the incident plane wave is shot toward the inhomogeneous object. At the scatterer boundary, reflected rays and refracted rays are generated due to discontinuity of the medium parameters. The trajectory, amplitude, phase and polarization of the refracted rays are traced inside the inhomogeneous object based on geometrical optics. Whenever the rays cross the scatterer surface, additional reflected/refracted rays are generated and are tracked. This process is repeated until the intensities of the refracted/reflected rays become negligible. The contributions of the exiting rays to the total scattered field are calculated by using the equivalence principle in conjuction with a ray-tube integration scheme. The ray formulation is applied to calculate the bistatic scattering from cylinders and spheres. The numerical results of the ray formulation are compared with exact series solutions for homogeneous and inhomogeneous objects.

This work is supported by the National Science Foundation under Grant ECS-8657524 and in part by the NASA Lewis Research Center under Cooperative Agreement NCC3-127.

I. INTRODUCTION

The study of electromagnetic scattering from inhomogeneous objects has received a great deal of attention because of its importance in many practical areas such as dielectric lens design, radar signatures from aircraft and missile plumes and power deposition in biological tissues. Several numerical techniques are available to treat such problems. Among them are the method of moments solution using either surface integral [1] or volume integral equations [2], the unimoment method [3], and hybrid methods [4], [5] combining the finite element method with the integral equation approach. All of these "numerically exact" methods, however, are limited to the low frequency regime where the electrical size of the scatterer is small, due to the computation time involved and the amount of computer memory required. For electrically large scatterers, approximate methods such as high frequency ray techniques become more attractive.

Kouyoumjian et al. [6] used a modified geometrical optics (GO) approach to study the backscattering from electrically large, homogeneous dielectric objects. By tracing rays analytically inside homogeneous objects of special shape, good results were obtained in the backscattering direction. Chen [7] formulated the problem of bistatic scattering from homogeneous objects by considering diffracted rays as well as GO rays. However, no numerical results were reported in his work. In this paper, a ray approach is presented to characterize the scattering from electrically large, inhomogeneous objects. This work is motivated by our earlier study of space plasma effects on microwave reflector antenna performance [8]. Since the inhomogeneous plasma plume from an arcjet thruster is large in terms of the wavelength of the reflector antenna signal, ray theory is applicable. The ray tracing technique documented in this paper is a natural extension of the so-called "shooting and bouncing ray" (SBR) scheme, developed earlier for calculating the radar cross section of partially open inlet structures [9]. A dense grid of geometrical optic rays representing an

incident plane wave is shot toward the inhomogeneous object. At the scatterer boundary, reflected rays and refracted rays are generated due to discontinuity of the medium parameters (see Fig. 1). The trajectory, amplitude, phase and polarization of the refracted ray are traced inside the inhomogeneous object based on the laws of geometrical optics. Whenever the rays cross the scatterer surface, additional reflected/ refracted rays are generated and are tracked. This process is repeated until the intensities of the refracted/reflected rays become negligible and the ray tracing algorithm can be terminated. The contributions of all the exiting rays to the exterior scattered field are then calculated by using the equivalence principle in conjuction with a ray-tube integration scheme [10].

The organization of this paper is as follows. In Sec. 2, the ray formulation is presented. First, the propagation of the GO field in an arbitrary inhomogeneous medium and the GO reflection/refraction problem at a curved dielectric interface are discussed. Once information on the exiting rays are found, a ray tube integration scheme, which consists of summing the scattered fields from individual ray tubes, is considered in order to arrive at the scattered field in the exterior region. In Sec. 3, numerical results for various inhomogeneous objects are presented. They are compared against the available exact solutions. Finally, some conclusions are summarized in Sec. 4.

II. FORMULATION

The geometry of the scattering problem is shown in Fig. 1. An inhomogeneous object, which is defined by the constitutive parameters ε and μ (or refractive index $N=(\varepsilon_r\mu_r)^{1/2}$), is illuminated by an incident plane wave in free space. The refractive index of the scatterer is assumed to be smoothly varying, except at the scatterer boundary. The objective is to determine the scattered field using a ray tracing approach. To represent the incident plane wave, a large number of rays are shot toward the inhomogeneous object. The incident rays encounter the scatterer boundary and reflected rays and refracted rays are generated, e.g., at point 1 in Fig. 1. The refracted rays propagate inside the object and eventually encounter the scatterer boundary (point 2 in Fig. 1). Again reflected rays and refracted rays are generated, except this time the refracted rays exit the scatterer while the reflected rays bounce off the boundary and propagate inside the inhomogeneous object. The intensities of the reflected rays should become weaker after every bounce against the boundary and this process can be terminated after several bounces. To account for the ray reflection and refraction at the curved scatterer boundary, the geometrical optics solution described in [4] is summarized in Sec. 2.1. Next, ray tracing in an arbitrary inhomogeneous medium is implemented numerically. The relevant equations [3] for the ray trajectory, the associated phase, amplitude and polarization of the ray field are detailed in Sec. 2.2. Finally, whenever a ray exits the scatterer boundary, the contribution of the ray to the total scattered field is calculated by a ray-tube integration scheme [9,11]. The integration is taken over the projection of the ray tube on the scatterer boundary and the fields on the scatterer boundary is approximated by the ray fields. This scheme is described in Sec. 2.3.

2.1. GO Reflection/Refraction at the Curved Scatterer Boundary

When a ray is incident upon the scatterer boundary, a reflected ray and a refracted ray are generated due to the discontinuity in the medium parameters. To determine the fields associated with the reflected and refracted rays as they propagate away from the boundary, their initial values including the ray directions, amplitudes, polarizations and wavefront curvatures are needed at the impact point. Let $\hat{t}_i$, $\hat{t}_r$, $\hat{t}_t$ be the direction vectors of the incident, reflected and refracted rays, respectively. The plane defined by $\hat{t}_i$ and $\hat{n}$ is the plane of incidence and $\hat{v}$ is a unit vector perpendicular to that plane (see Fig. 2). $\hat{t}_r$, $\hat{t}_t$ can be determined by Snell's law as follows:

$$\begin{aligned} &\hat{t}_r \cdot \hat{u}) = \hat{t}_i \cdot \hat{n}\,,\ \hat{t}_r \cdot \hat{v} = 0\,,\ |\hat{t}_r| = 1 \\ &n_1\,(\hat{t}_r \cdot \hat{n}) = n_2\,(\hat{t}_i \cdot \hat{n})\,,\ \hat{t}_t \cdot \hat{v} = 0\,,\ |\hat{t}_t| = 1 \end{aligned} \tag{1}$$

For the amplitude and polarization calculation, Fresnel's formulas for a planar interface can be used for a curved interface under the high frequency approximation. The incident field is first decomposed into its perpendicular and parallel components as follows (refer to Fig. 2):

$$\vec{E}^i = (\vec{E}^i \cdot \hat{\phi}^i)\hat{\phi}^i + (\vec{E}^i \cdot \hat{\theta}^i)\hat{\theta}^i \tag{2}$$

The reflected and transmitted fields at the impact point on the boundary are then obtained by using the planar reflection and transmission coefficients:

$$\begin{aligned} \vec{E}^r &= R(\vec{E}^i \cdot \hat{\phi}^i)\hat{\phi}^r + R'(\vec{E}^i \cdot \hat{\theta}^i)\hat{\theta}^r \\ \vec{E}^t &= T(\vec{E}^i \cdot \hat{\phi}^i)\hat{\phi}^t + T'(\vec{E}^i \cdot \hat{\theta}^i)\hat{\theta}^t \end{aligned} \tag{3}$$

where

$$R = \frac{\sqrt{\frac{\mu_2}{\varepsilon_2}}\cos\theta_i - \sqrt{\frac{\mu_1}{\varepsilon_1}}\cos\theta_t}{\sqrt{\frac{\mu_2}{\varepsilon_2}}\cos\theta_i + \sqrt{\frac{\mu_1}{\varepsilon_1}}\cos\theta_t}$$

$$T = 1 + R$$

$$R' = \frac{\sqrt{\frac{\mu_1}{\varepsilon_1}}\cos\theta_i - \sqrt{\frac{\mu_2}{\varepsilon_2}}\cos\theta_t}{\sqrt{\frac{\mu_1}{\varepsilon_1}}\cos\theta_i + \sqrt{\frac{\mu_2}{\varepsilon_2}}\cos\theta_t}$$

$$T' = (1+R')\sqrt{\frac{\mu_2\varepsilon_1}{\varepsilon_2\mu_1}}$$

$$\hat{\theta}^i = \hat{u}\cos\theta_i - \hat{n}\sin\theta_i$$

$$\hat{\theta}^r = -\hat{u}\cos\theta_i - \hat{n}\sin\theta_i$$

$$\hat{\theta}^t = -\hat{u}\cos\theta_t - \hat{n}\sin\theta_t$$

$$\hat{\phi}^i = \hat{\phi}^r = \hat{\phi}^t = \hat{v}$$

θ_i and θ_t: incident angle and transmitted angle.

Information on the reflected and refracted wavefronts are necessary in order to determine the ray fields away from the scatterer boundary. The curvatures of the reflected and refracted wavefronts can be compactly represented by the wavefront curvature matrices, $\tilde{Q}^r$ and $\tilde{Q}^t$ [16], from which the principal radii of curvature and the principal directions can be extracted. The curvature matrices $\tilde{Q}^r$ and $\tilde{Q}^t$ can be determined by enforcing the phase matching condition on the scatterer boundary. This results in the following matrix equations, relating with the incident wavefront curvature matrix $\tilde{Q}^i$ and the boundary surface curvature matrix $\tilde{Q}^s$, to $\tilde{Q}^r$ and $\tilde{Q}^t$:

$$B_r^T\tilde{Q}^rB_r = B_i^T\tilde{Q}^iB_i - 2\cos\theta_i\tilde{Q}^s \qquad (4)$$

$$\frac{n_2}{n_1}B_t^T\tilde{Q}^tB_t = B_i^T\tilde{Q}^iB_i + (\frac{n_2}{n_1}\cos\theta_t - \cos\theta_i)\tilde{Q}^s$$

where

$$B_{i,t} = \begin{bmatrix} \hat{\theta}^{i,t}\cdot\hat{u} & \hat{\theta}^{i,t}\cdot\hat{v} \\ \hat{\phi}^{i,t}\cdot\hat{u} & \hat{\phi}^{i,t}\cdot\hat{v} \end{bmatrix} = \begin{bmatrix} \cos\theta_{i,t} & 0 \\ 0 & 1 \end{bmatrix}$$

$$B_r = \begin{bmatrix} \hat{\theta}^r\cdot\hat{u} & \hat{\theta}^r\cdot\hat{v} \\ \hat{\phi}^r\cdot\hat{u} & \hat{\phi}^r\cdot\hat{v} \end{bmatrix} = \begin{bmatrix} -\cos\theta_i & 0 \\ 0 & 1 \end{bmatrix}$$

The curvature matrices $\tilde{Q}^s$, $\tilde{Q}^i$, $\tilde{Q}^r$, $\tilde{Q}^t$ are described by the basis vector sets $(\hat{u}, \hat{v})$, $(\hat{\theta}^i, \hat{\phi}^i)$, $(\hat{\theta}^r, \hat{\phi}^r)$, $(\hat{\theta}^t, \hat{\phi}^t)$, respectively. Once $\tilde{Q}^r$ and $\tilde{Q}^t$ are determined from the above matrix equations, they may be diagonalized in the standard fashion to arrive at their eigenvectors (principal vectors) and eigenvalues (principal radii of curvature). These information are used subsequently to calculate the ray field inside the inhomogeneeous scatterer.

2.2. Ray Propagation in Inhomogeneous Media

The propagation of a ray field inside the inhomogeneous scatterer, including the ray trajectories and the associated phase, amplitude and polarization, is considered. The solution of geometrical optic fields in inhomogeneous media was first derived by Luneburg more than 30 years ago and has been documented in detail by Kline and Kay [13], Born and Wolf [14] and most recently, Bremmer and Lee [15]. It is important to point out that the ray optics field is a high-frequency approximation to the exact full-wave solution. In referring to high frequencies, the key is the relation of the scatterer size and curvature of the wavefront to wavelength. Therefore, the following summarized results concerning ray tracing are valid only when the medium properties, represented by ε and μ or $N=(\varepsilon_r\mu_r)^{1/2}$,

vary slowly and continuously over distances of several wavelengths. When the variation of the medium is not smooth, a full wave analysis is required. Ray optics also fails near focal points, or on caustic surfaces, where it predicts an infinite field.

The ray trajectory in space is governed by the vector differential equation:

$$\frac{d}{ds}(n\hat{t}) = \nabla n \tag{5}$$

where $\hat{t}$ is a unit tangent vector at a point along the ray. The arclength s is measured along the ray trajectory, and N is the refractive index. For an arbitrary inhomogeneous medium with a continuous index of refraction N, the trajectory of each ray can be traced by solving the above vector differential equation. At points where N is discontinuous, the differential equation does not apply. Instead, a reflected ray and a refracted ray are generated, as discussed earlier.

Once the ray trajectory is determined, the phase variation along the the ray is given by Fermat's relationship:

$$S(P_1) = S(P_2) + \int_{P_1}^{P_2} n\, ds \tag{6}$$

The complete ray optics field at point P_2 can be determined from the values at point P_1 by the following equation:

$$\vec{E}(P_2) = \hat{e}_2\, E(P_1) \sqrt{n_1 / n_2}\, (DF) \exp\{-jk_0[S(P_2)-S(P_1)]\} \tag{7}$$

The field amplitude for a lossless medium is governed by the quantity (DF), the so-called divergence factor, which accounts for the expansion of the differential ray tube so that the energy carried by the ray tube remains constant (see Fig. 3). The divergence factor is given by

$$DF = \exp\{-\frac{1}{2}\int_{P_1}^{P_2}(\frac{1}{R_1}+\frac{1}{R_2})\,ds\} \tag{8}$$

where R_1 and R_2 are the two principal radii of curvature of the wavefront along the ray. The directions in which the radii of curvature at a point on the wavefront have minimum and maximum values define the two principal directions.

The polarization vector $\hat{e}_2$ at P_2 is related to the polarization vector $\hat{e}_1$ at P_1 by the equation:

$$\hat{e}_2 = \hat{n}_2\cos(\theta_0-\hat{\theta}) + \hat{b}_2\sin(\theta_0-\hat{\theta}) \tag{9}$$

where

$$\theta_0 = \tan^{-1}(\frac{\beta_0}{\alpha_0}),\ \hat{\theta} = \int_{P_1}^{P_2}\tau\,ds$$

$$\hat{e}_1 = \hat{n}\alpha_0 + \hat{b}\beta_0\ ,\quad \tau = \frac{(\hat{t}\times\hat{t}')\cdot\hat{t}''}{|\hat{t}\times\hat{t}'|^2}$$

In the above equation, $\hat{n}$, $\hat{b}$ and $\hat{t}$ are respectively the normal, binormal and tangent vectors along the ray, and the prime represents the derivative with respect to the arclength s. τ is the torsion of the ray paths in space. For planar ray paths, the torsion is zero and the electric field remains at a constant angle with respect to the normal and binormal vectors along the ray.

2.3. Ray-Tube Integration

Once the total fields on the scatterer boundary ($\vec{E}$, $\vec{H}$) are calculated, the scattered field in the exterior region can be calculated based on the equivalence principle [12]. As shown in Fig. 4, the equivalent surface currents are related to the surface fields by $\vec{J}_s = \hat{n}\times\vec{H}$ and $\vec{M}_s = -\hat{n}\times\vec{E}$where $\hat{n}$ is the outward surface normal vector. They radiate in

free space to give rise to the scattered field. The scattered far field can be calculated by the following radiation integral:

$$\vec{E}^s = \frac{e^{-jkr}}{r}[\hat{\theta}A_\theta + \hat{\phi}A_\phi] \tag{10}$$

$$\begin{bmatrix} A_\theta \\ A_\phi \end{bmatrix} = \frac{jk}{4\pi}\int_{\substack{\text{Scatterer} \\ \text{Surface}}} e^{j\vec{k_0}\cdot\vec{r}'}\left(\begin{bmatrix} -\hat{\phi} \\ \hat{\theta} \end{bmatrix}\times\vec{E}(r') + Z_0\begin{bmatrix} \hat{\theta} \\ \hat{\phi} \end{bmatrix}\times\vec{H}(r')\right)\cdot\hat{n}\, ds'$$

where $\hat{\phi}, \hat{\theta}$ are unit vectors in the direction ϕ, θ and r' is the position vector of the scatterer surface. However, the fields on the scatterer boundary ($\vec{E}$, $\vec{H}$), calculated by ray tracing, are not available on a uniform grid of points over the surface. Direct integration of the above radiation integral, therefore, cannot be easily carried out and the ray-tube integration scheme described in [9,11] is used. Since the incident plane wave can be considered as a superposition of small ray tubes, the contribution of each ray tube to the scattered field is calculated separately. Whenever the ray tube is reflected/refracted at the scatterer boundary, the ray tube contribution to the scattered field is calculated.

Referring to Fig. 5, when a small tube of ray exits the scatterer, the field at $\vec{r}$ on the scatterer surface can be approximated as:

$$\vec{E}(\vec{r}) \cong \vec{E}(\vec{r}_a)\exp\{-jk\hat{t}\cdot(\vec{r}-\vec{r}_a)\} \tag{11}$$
$$\vec{H}(\vec{r}) \cong \vec{H}(\vec{r}_a)\exp\{-jk\hat{t}\cdot(\vec{r}-\vec{r}_a)\} = \frac{\hat{t}\times\vec{E}(\vec{r}_a)}{Z_0}\exp\{-jk\hat{t}\cdot(\vec{r}-\vec{r}_a)\}$$

where $\vec{r}_a$ describes the position perpendicular to the ray direction and $\hat{t}$ is the direction of the exit ray. In other words, the field on the scatterer boundary is assumed to have the same magnitude as the ray tube and linear phase variation across the ray tube projection on the surface. The radiation integral in (10) can be applied to calculate the scattered field contribution of this small ray tube:

$$\begin{bmatrix} A_\theta \\ A_\phi \end{bmatrix}_i = \frac{jk}{4\pi} \int_{\substack{\text{ray tube} \\ \text{projection} \\ \text{on S}}} e^{j\vec{k}\cdot\vec{r}'} \left(\begin{bmatrix} -\hat{\phi} \\ \hat{\theta} \end{bmatrix} \times \vec{E}_s(\vec{r}_a) + Z_0 \begin{bmatrix} \hat{\theta} \\ \hat{\phi} \end{bmatrix} \times \vec{H}_s(\vec{r}_a) \right) e^{-jk\hat{t}\cdot(\vec{r}'-\vec{r}_a)} \cdot \hat{n} \, ds' \tag{12}$$

$$\cong \frac{jk}{4\pi} e^{j\vec{k}\cdot\vec{r}_a} \left(\begin{bmatrix} -\hat{\phi} \\ \hat{\theta} \end{bmatrix} \times \vec{E}_s(r_a) + Z_0 \begin{bmatrix} \hat{\theta} \\ \hat{\phi} \end{bmatrix} \times \vec{H}_s(r_a) \right) \cdot \hat{n} \; (\Delta A) \; S(\theta,\phi)$$

where

$$S(\theta, \phi) = \frac{1}{(\Delta A)} \int_{\substack{\text{ray tube} \\ \text{projection}}} e^{jk(\hat{k}-\hat{t})\cdot(\vec{r}'-\vec{r}_a)} \, ds'$$

ΔA = Area of ray tube projection on surface S = (Ray tube area / cos ($\hat{n}$, $\hat{t}$))

This process is repeated as the ray tube undergoes multiple reflections with the scatterer boundary, until the remaining energy of the ray tube is negligible with respect to the energy carried by the incident ray tube. Finally,

$$\begin{bmatrix} A_\theta \\ A_\phi \end{bmatrix} = \sum_i \begin{bmatrix} A_\theta \\ A_\phi \end{bmatrix}_i \tag{13}$$

as the total scattered field is the superposition of the scattered field of all individual ray tubes

III. NUMERICAL RESULTS

Based on the ray formulation in Sec. 2, both a two-dimensional and a three-dimensional ray tracing code have been implemented. It is found from numerical experimentation that launching incident rays from a nonuniform grid (refer to Fig. 6) is more efficient computationally than using uniform ray density. A higher ray density should be used on the outer region of the scatterer so that the number of rays per unit perimeter (or in the three-dimensional case, per unit surface area) launched toward the scatterer boundary is fixed. Convergence test is performed and it is observed that more than four rays per wavelength of the scatterer perimeter are necessary for convergent results in the two-dimensional case. A representative convergence test for the backscattering from a circular cylinder is shown in Fig. 7.

Since the ray formulation is inherently a high-frequency approximation, it is instructive to investigate the lower bound of validity of the ray results. The ray formulation is applied to the scattering from homogeneous circular cylinders of different sizes and the results shown in Figs. 8 - 10. Both the TM and TE bistatic scattering patterns generated using the ray formulation are superimposed with the exact series solutions for cylinders with diameter 1λ, 4λ and 8λ. Note that the ray results, as expected, improve in accuracy as the size of the object increases. The lower limit of the scatterer size, to which the ray scattering formulation can be applied, is about three free-space wavelengths. It is also observed that while the agreement with the exact solution is very good for the TM polarization, the agreement is not as good for the TE case, particularly near $\phi = 150°$. It is not clear what causes the poor agreement, although the same observation can be made from Kouyoumjian's work [6].

The ray scattering formulation is next applied to two-dimensional radially inhomogeneous circular cylinders for both TM and TE incident waves. Since the exact series solution is available for radially multi-layered cylinders [18], the solution of the

radially inhomogeneous cylinder is obtained by modeling it as a cylinder of many layers with different refractive indices. More than 10 layers per wavelength are used to approximate the exact solution for the inhomogeneous cylinder. The ray formulation is applied to cylinders with a smoothly varying refractive index profile of the form:

$$N(\rho) = \sqrt{d + b(1 - c\cos\frac{\pi\rho}{a})} \tag{13}$$

where

$$b = \frac{1 + \varepsilon_r(0)}{2}, \quad c = \frac{1 - \varepsilon_r(0)}{1 + \varepsilon_r(0)}$$

Shown in Figs.11 - 13 are the comparisons of the ray results with the layered solutions for different $\varepsilon_r(0)$ with d=4. The diameter of the cylinders is chosen to be 6 λ. It is observed that the ray results agree well with the exact solutions for the TM cases. For the TE cases, the agreements are not as close as those for the TM cases. This could be caused by the GO reflection/refraction modeling at the scatterer boundary also noted earlier in the homogeneous case. As a more general application, the ray formulation is applied to an inhomogeneous cylinder with angular as well as radial variations in the refractive index. Fig. 14 shows the bistatic scattering patterns.

For three-dimensional cases, the ray formulation is applied to scattering from inhomogeneous spheres. The three-dimensional refractive index profile is assumed to have the same radial variation as that of the above two-dimensional inhomogeneous cylinder, except that the variable ρ in expression (13) is replaced by the three-dimensional radial variable r. For comparison, the exact solution is obtained by using the multi-layered model [19] of radially inhomogeneous spheres, as in the two-dimensional case. Shown in Fig. 15 are the E-plane bistatic scattering patterns for several three-dimensional scatterers. From the numerical results, it was found that the E-plane and the H-plane scattering patterns are almost the same, as expected for large scatterers. Fig. 15(a) shows a sphere without any discontinuity in the refractive index at the boundary. In this case, no reflection

is generated at the scatterer boundary and good agreement is obtained between the ray results and the exact solution. Figs. 15(b) and 15(c) are the results for, respectively, a homogeneous sphere and an inhomogeneous sphere with a sharp discontinuity at the boundary. The agreement between the ray results and the exact solutions is only good in the forward scattering region. It is also found that the agreement deteriorates as the refractive index of the scatterer increases. A possible reason for the discrepancies can be traced back to the reflection/refraction problem for the parallel (TE) polarization case. Since the three-dimensional results involve both polarizations, the same problem is manifested in the results. In addition, more accurate high-frequency analysis such as the geometrical theory of diffraction for materials should be included in the ray tracing. However, we can see that the approximate scattering patterns can be calculated by this ray formulation, and it is expected that the ray formulation will be more accurate for the larger scatterers.

As a final note, the present ray approach uses GO fields on the scatterer surface. If caustic points are located on or near the surface, GO fields are not accurate and the scattered field calculated based on the surface GO fields will not be accurate. This problem can be solved by choosing a Huygens' surface larger than the scatterer boundary so that the caustic points can be avoided. Another problem in the present formulation is the occurance of total internal reflection, when a ray is incident at an angle greater than the critical angle in the denser medium. Total internal reflection at a curved interface is a complicated phenomenon and the conventional Fresnel formulas should be modified. More detailed discussions are found in [20] - [22].

IV. CONCLUSION

A ray tracing scheme was presented to calculate the bistatic scattering patterns for electrically large, inhomogeneous objects. Inside the inhomogeneous object, the reflected and refracted ray bundles from the scatterer boundary were traced based on the laws of geometrical optics. From the fields and the "footprints" of the ray bundles on the scatterer boundary, the scattered field pattern was obtained by a ray-tube integration technique. To test the validity and accuracy of the ray tracing scheme, it was applied to the electromagnetic scattering of both two-dimensional and three-dimensional objects. It was shown that the ray results agree approximately with the exact series solutions. In the forward scattering region, the agreement is very good. As expected, it was observed that the accuracy of the ray scheme improved as the size of the object was increased. From numerical experiments, it was found that the ray tracing scheme is valid for objects greater than about three free-space wavelengths. Also, it was observed that the accuracy of the ray scheme deteriorates for objects of high refractive index. More accurate account of the scattering mechanisms at the object boundary using the geometrical theory of diffraction may alleviate the limitations of this geometrical optics scheme.

REFERENCES

[1] N. Morita, " Surface integral representation for electromagnetic scattering from dielectric cylinders," *IEEE Trans. Antennas Propagat.*, vol. AP-26, no. 2, pp. 261-266, Mar. 1978.

[2] J. H. Richmond, "Scattering by a dielectric cylinder of arbitrary crosssection shape," *IEEE Trans. Antennas Propagat.*, vol. AP-13, no. 3, pp.334-341, May 1965.

[3] K. K. Mei, "Unimoment method of solving antenna and scattering problems," *IEEE Trans. Antennas Propagat.*, vol. AP-22, no. 6, pp.760-766, Nov.1974

[4] K. D. Paulsen, D. R. Lynch and J. W. Strohbehn, " Three dimensional finite, boundary, and hybrid elements solutions of the Maxwell equations for lossy dielectric media," *IEEE Trans. Microwave Theory Tech.*, vol. MTT-36, no. 4, pp. 682-693, April 1988.

[5] X. Yuan, "Coupling of finite element and moment methods for electromagnetic scattering from inhomogeneous objects," *IEEE Trans. Antennas Propagat.*, vol. AP-38, no. 3, pp. 386-393, Mar. 1990.

[6] R. G. Kouyoumjian, L. Peters, Jr. and D. T. Thomas, "A modified geometrical optics method for scattering by dielectric bodies," *IRE Trans. Antennas Propagat.*, vol. 11, no. 6, pp. 690-703, Nov. 1963.

[7] Y. M. Chen, "Diffraction by a smooth transparent object," *J. Math. Phys*, vol. 5, no. 6, June 1964.

[8] H. Ling, G. A. Hallock, H. Kim and B. W. Birkner, "Near field interaction of microwave signals with a bounded plasma plume," annual report submitted to NASA/Lewis Research Center under Grant No. NCC3-127, Jan. 1990.

[9] H. Ling, R. C. Chou and S.W. Lee, "Shooting and bouncing rays: calculating the RCS of an arbitrarily shaped cavity," *IEEE Trans. Antennas Propagat.*, vol. AP-37, pp. 194-205, 1989.

[10] S. W. Lee, H. Ling and R. Chou, "Ray tube integration in shooting and bouncing ray method," *Microwave Opt. Tech. Lett.*, vol. 1, no.8, pp. 285-289, 1988.

[10] C. A. Balanis, *Advanced Engineering Electromagnetics*. New York: John Wiley & Sons, 1989.

[12] R. F. Harrington, *Time-harmonic electromagnetic fields*. New York: McGraw-Hill, 1961, Chap. 3.

[13] M. Kline and I. W. Kay, *Electromagnetic theory and geometrical optics*. New York: Wiley, 1965, Chap. 5.

[14] M. Born and E. Wolf, *Principles of optics*. New York: MacMillan, 1964, Chap. 3.

[15] H. Bremmer and S. W. Lee, "Propagation of a geometrical optics field in an isotropic inhomogeneous medium," *Radio Sci.*, vol. 19, pp. 243-257, 1984.

[16] S. W. Lee, M. S. Sheshadri, V. Jamnejad and R. Mittra, "Reflection at a curved dielectric interface: geometrical optics solution," *IEEE Trans. Microwave Theory Tech.*, vol. MTT-30, pp. 12-19, Jan. 1982.

[17] G. A. Deschamps, "Ray techniques in electromagnetics," *Proc. IEEE*, vol. 60, pp. 1022-1035, Sept. 1972.

[18] H. E. Bussey and J. H. Richmond, "Scattering by a lossy dielectric circular cylindrical multi-layer, numerical values," *IEEE Trans. Antennas Propagat.*, vol. AP-23, pp. 723-725, Sept. 1975.

[19] J. R. Wait, "Electromagnetic scattering from a radially inhomogeneous sphere," *Appl. Sci. Res.*, section B, vol. 10, pp. 441-450, 1963.

[20] A. W. Snyder and J. D. Love, "Reflection at curved dielectric interface electromagnetic tunneling," *IEEE Trans. Microwave Theory Tech.*, vol. MTT 13, pp. 134-141, 1975.

[21] E. Heyman and L. B. Felsen, "High frequency fields in the presence of a curved dielectric interface," *IEEE Trans. Antennas Propagat.*, vol. AP-32, pp. 969-978, Sept. 1984.

[22] E. Heyman, "On the tunneling hypothesis for ray reflection and transmission at a concave dielectric boundary," *IEEE Trans. Antennas Propagat.*, vol. AP-32, pp. 978-986, Sept. 1984.

Figure Captions

Fig. 1. The geometry of ray scheme.

Fig. 2. Local coordinate system of ray tube at the surface scatterer.

Fig. 3. Calculation of divergence factor for amplitude variation.

Fig. 4. The geometry of scattering problem. (a) original problem. (b) equivalent problem.

Fig. 5.The calculation of the total field on the Huygen surface (at $\vec{r}$) from the ray tube field (at $\vec{r}_a$).

Fig. 6. Non-uniform ray density for effective convergence.

Fig. 7. Convergence test of back scattering field as the number of rays per perimeter length in wavelength increases.

Fig. 8. The scattering pattern of homogeneous circular with 1 λ diameter. (a) TM. (b) TE.

Fig. 9. The scattering pattern of homogeneous circular with 4 λ diameter. (a) TM. (b) TE.

Fig. 10. The scattering pattern of homogeneous circular with 8 λ diameter. (a) TM. (b) TE.

Fig. 11. The scattering pattern of inhomogeneous circular cylinder with $2a=6\lambda$, $\varepsilon_r(0)=3$ and $\varepsilon_r(a)=4$. (a) TM. (b) TE.

Fig. 12. The scattering pattern of inhomogeneous circular cylinder with $2a=6\lambda$, $\varepsilon_r(0)=6$ and $\varepsilon_r(a)=4$. (a) TM. (b) TE.

Fig. 13. The scattering pattern of inhomogeneous circular cylinder with $2a=6\lambda$, $\varepsilon_r(0)=8$ and $\varepsilon_r(a)=4$. (a) TM. (b) TE.

Fig. 14. The scattering pattern of angularly inhomogeneous circular cylinder. (a) TM. (b) TE.

Fig. 15. The scattering pattern of spheres. (a) inhomogeneous with discontinuous boundary. (a) homogeneous. (c) inhomogeneous discontinuous boundary.

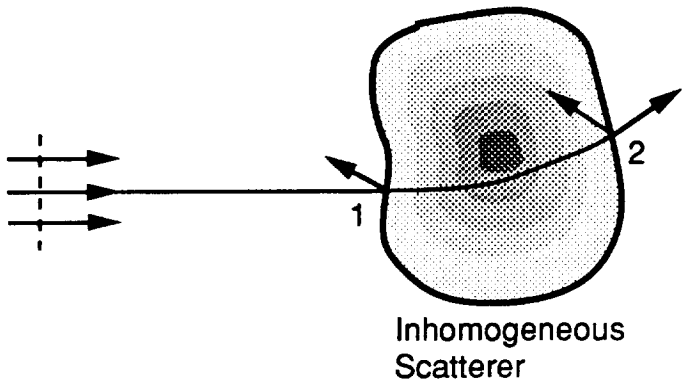

Fig. 1 The geometry of ray scheme

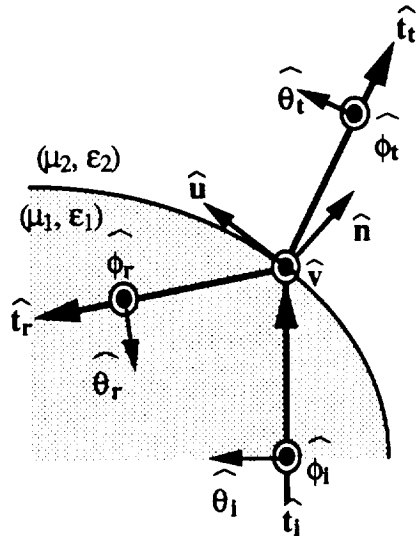

Fig. 2 Local coordinate system of ray tube at the scatterer surface

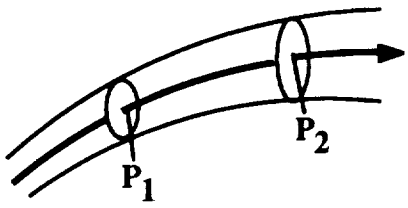

$$\left| DF \right|^2 = \frac{\text{Differential Ray Tube Area at } P_1}{\text{Differential Ray Tube Area at } P_2}$$

Fig. 3. Calculation of divergence factor for amplitude variation

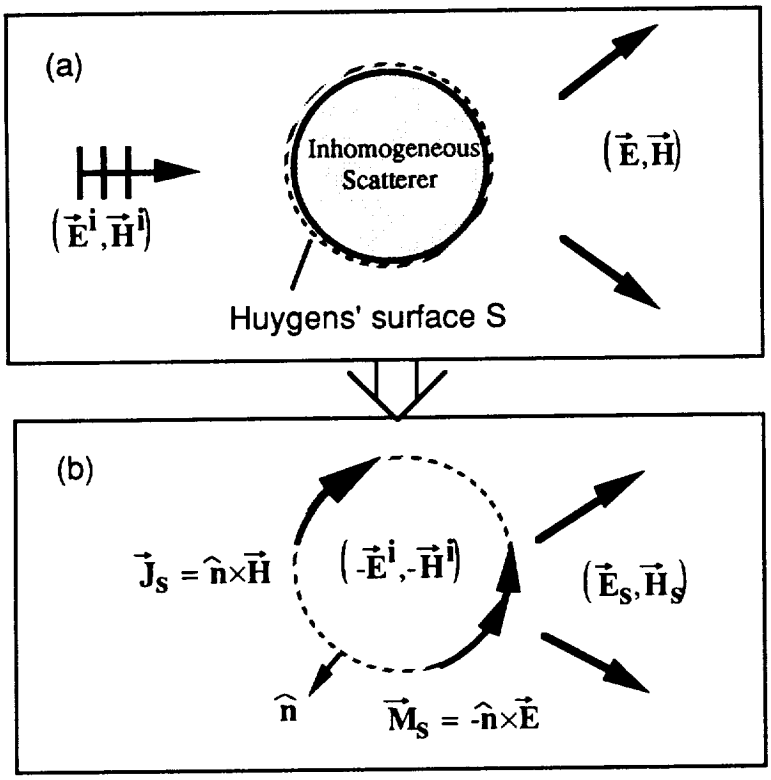

Fig. 4. The geometry of scattering problem
(a) Original problem. (b) Equivalent problem.

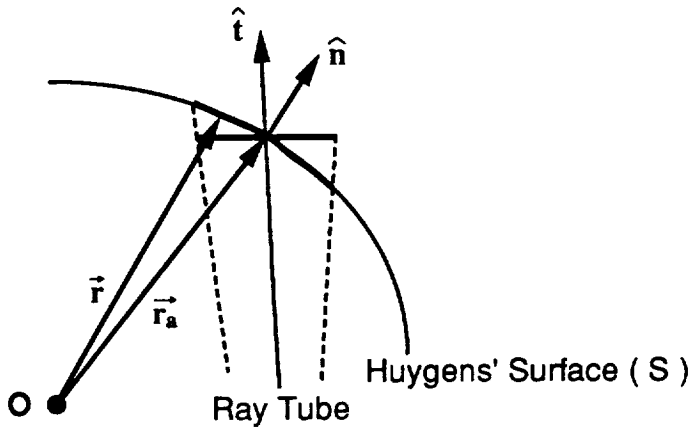

Fig. 5. The calculation of the field on the Huygens' surface from the ray tube field

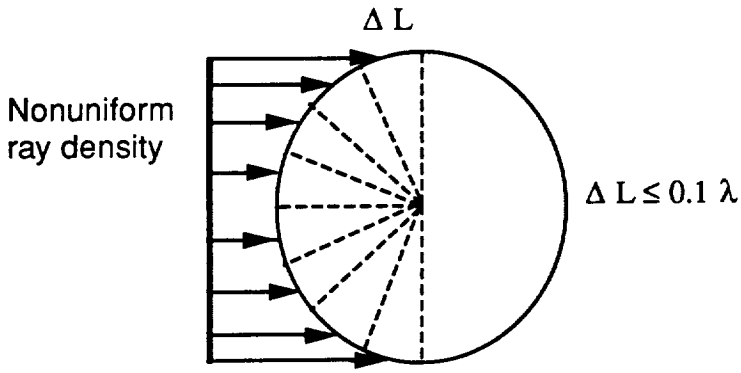

Fig. 6. Nonuniform ray density for effective convergence

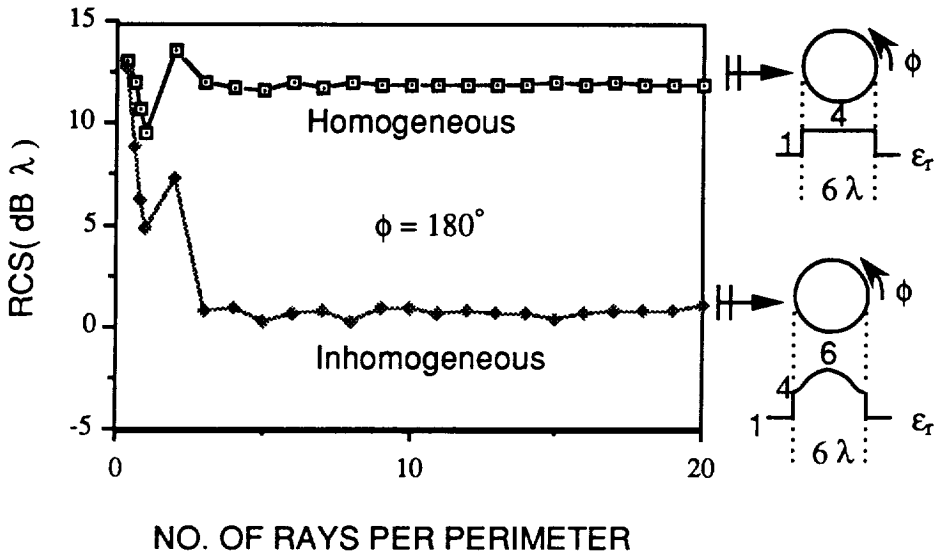

Fig. 7. Convergence test of back scattering field of cylinders as the number of rays per perimeter length in wavelegth increases

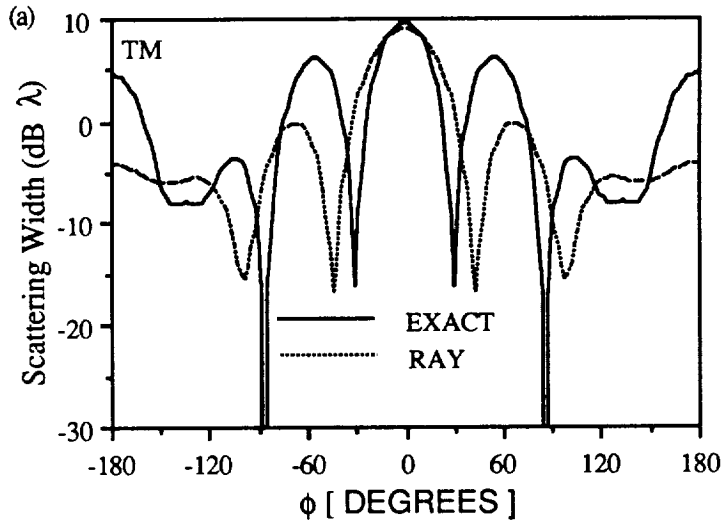
(a)
TM
Scattering Width (dB λ)
10
0
-10
-20
-30
EXACT
RAY
-180
-120
-60
0
60
120
180
ϕ [DEGREES]

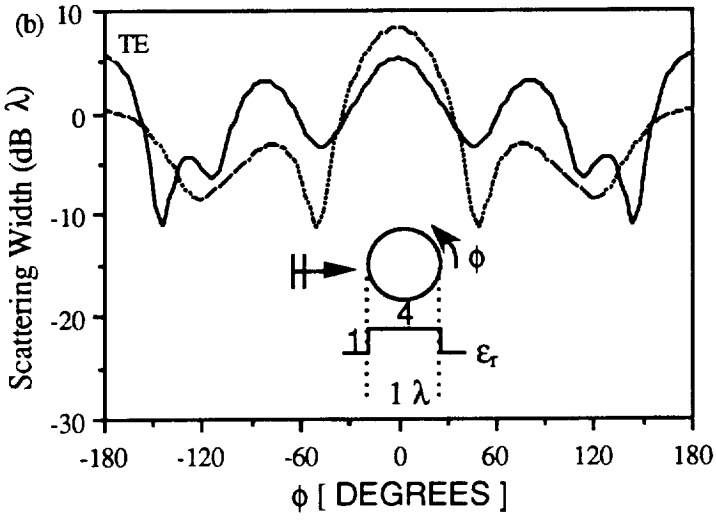
(b)
TE
Scattering Width (dB λ)
10
0
-10
-20
-30
ϕ
4
1
ε_r
1 λ
-180
-120
-60
0
60
120
180
ϕ [DEGREES]

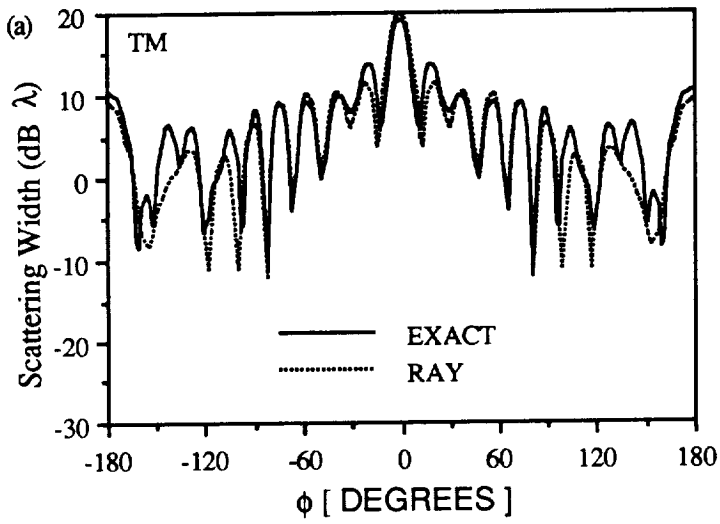
(a)
TM
Scattering Width (dB λ)
20
10
0
-10
-20
-30
EXACT
RAY
-180
-120
-60
0
60
120
180
ϕ [DEGREES]

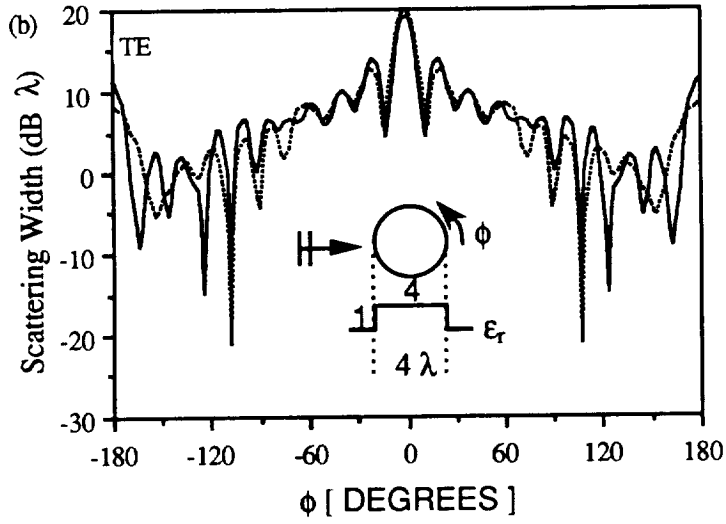
(b)
TE
Scattering Width (dB λ)
20
10
0
-10
-20
-30
ϕ
4
1
εr
4 λ
-180
-120
-60
0
60
120
180
ϕ [DEGREES]

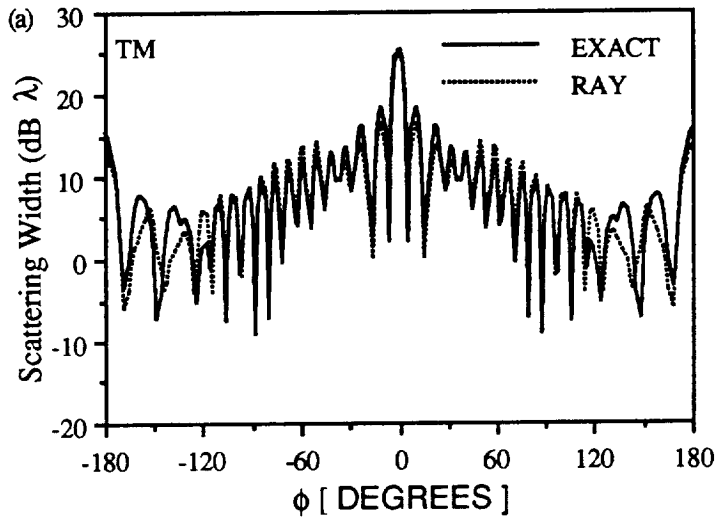
(a)
TM
EXACT
RAY
Scattering Width (dB λ)
30
20
10
0
-10
-20
-180
-120
-60
0
60
120
180
ϕ [DEGREES]

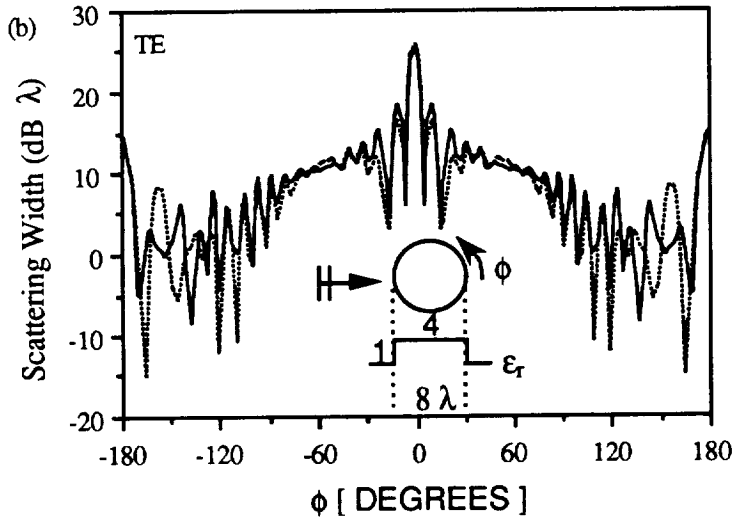
(b)
TE
Scattering Width (dB λ)
30
20
10
0
-10
-20
-180
-120
-60
0
60
120
180
ϕ [DEGREES]
ϕ
4
1
εr
8 λ

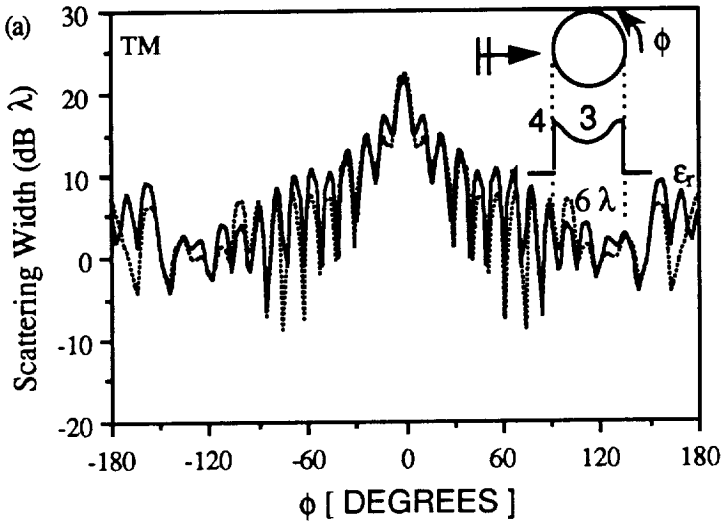
(a)
TM
30
20
10
0
-10
-20
Scattering Width (dB λ)
-180
-120
-60
0
60
120
180
ϕ [DEGREES]
ϕ
4
3
6 λ
εr

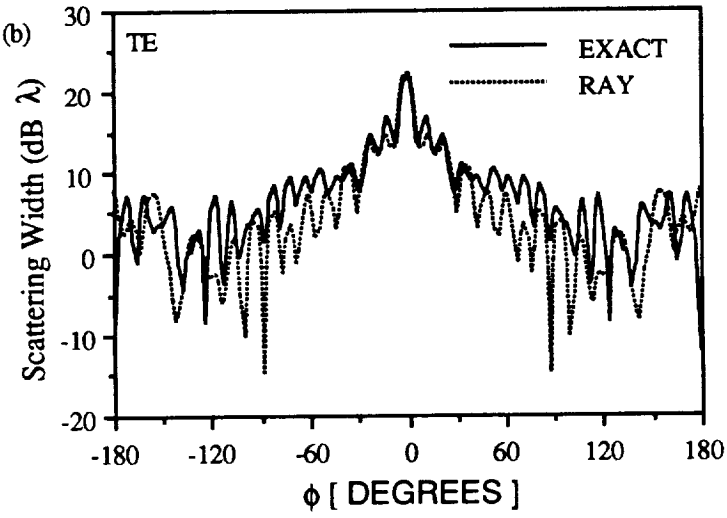
(b)
TE
EXACT
RAY
30
20
10
0
-10
-20
Scattering Width (dB λ)
-180
-120
-60
0
60
120
180
ϕ [DEGREES]

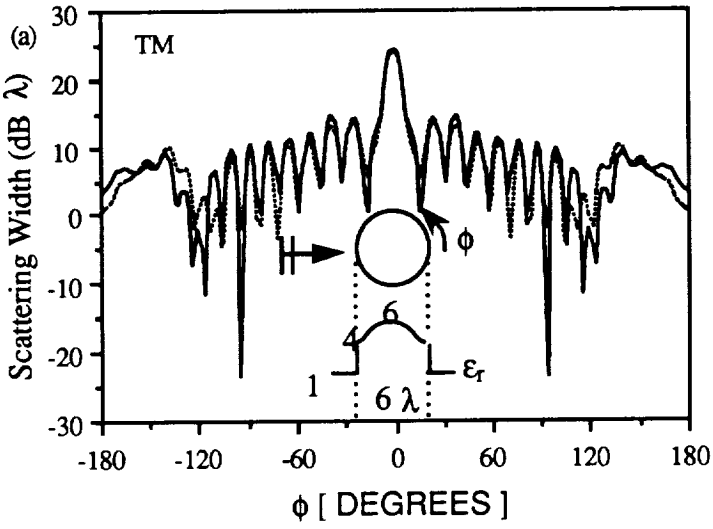
(a)
TM
Scattering Width (dB λ)
30
20
10
0
-10
-20
-30
-180
-120
-60
0
60
120
180
ϕ [DEGREES]
ϕ
6
4
1
6 λ
εr

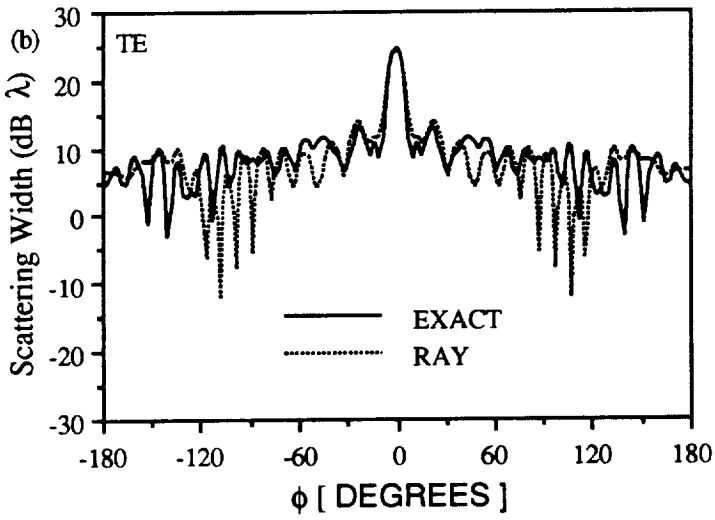
(b)
TE
Scattering Width (dB λ)
30
20
10
0
-10
-20
-30
-180
-120
-60
0
60
120
180
ϕ [DEGREES]
EXACT
RAY

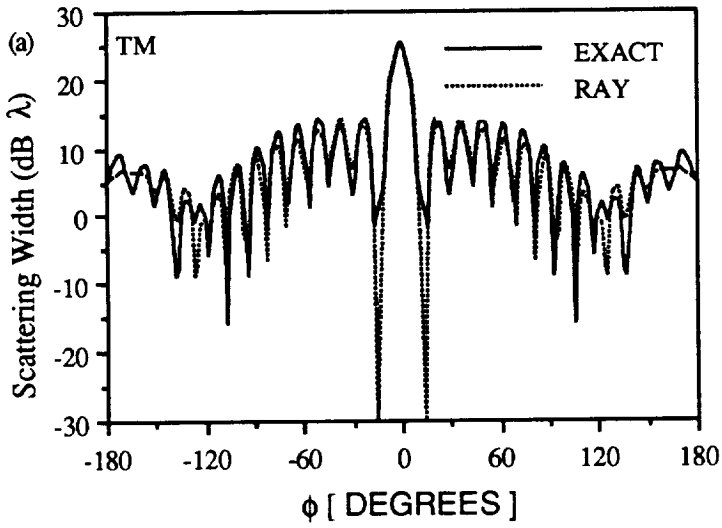
(a)
TM
EXACT
RAY
Scattering Width (dB λ)
30
20
10
0
-10
-20
-30
-180
-120
-60
0
60
120
180
φ [DEGREES]

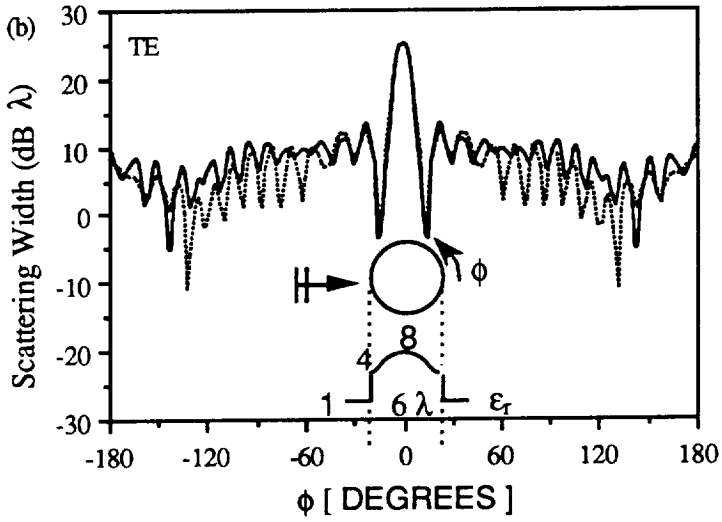
(b)
TE
Scattering Width (dB λ)
30
20
10
0
-10
-20
-30
φ
4
8
1
6 λ
εr
-180
-120
-60
0
60
120
180
φ [DEGREES]

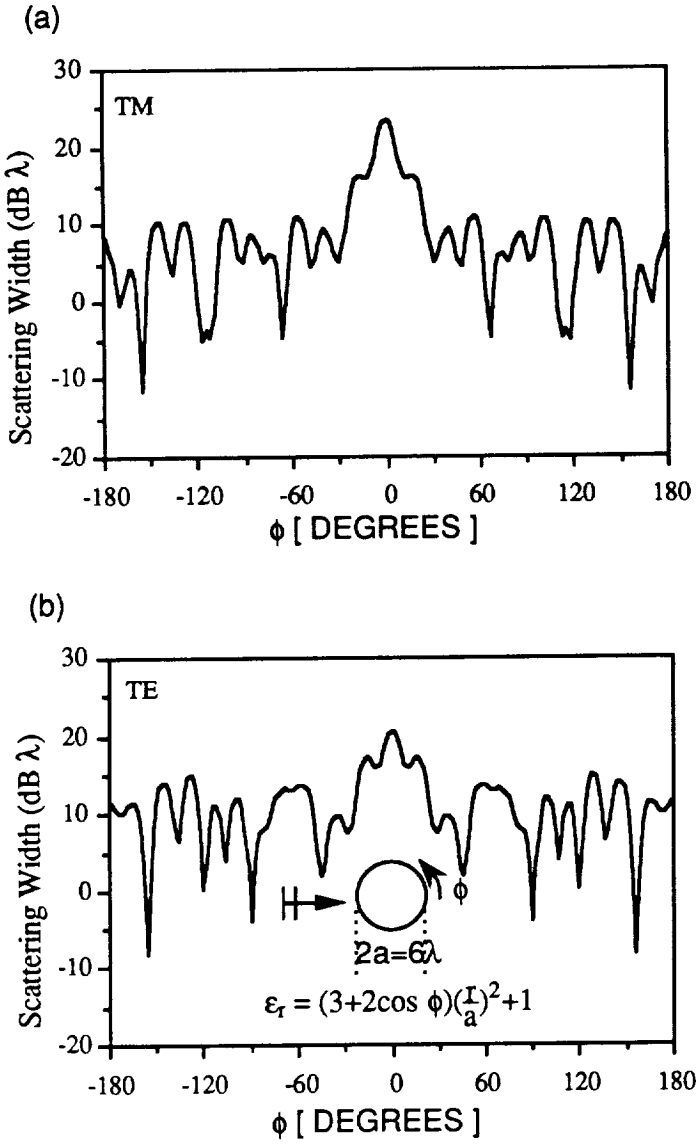

Fig. 14. The scattering pattern of angularly inhomogeneous circular cylinder. (a) TM. (b) TE.

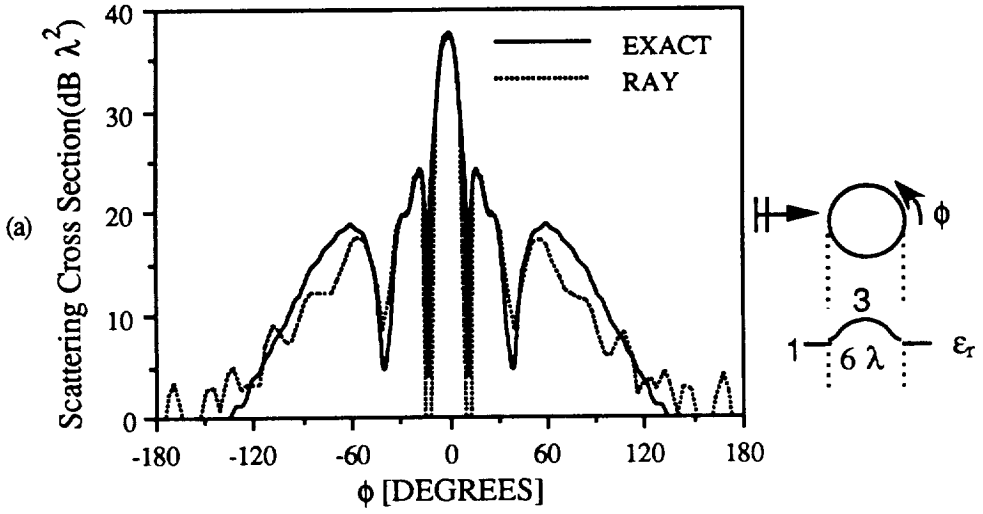
(a)
Scattering Cross Section(dB λ²)
EXACT
RAY
φ [DEGREES]
φ
3
1
6 λ
εr

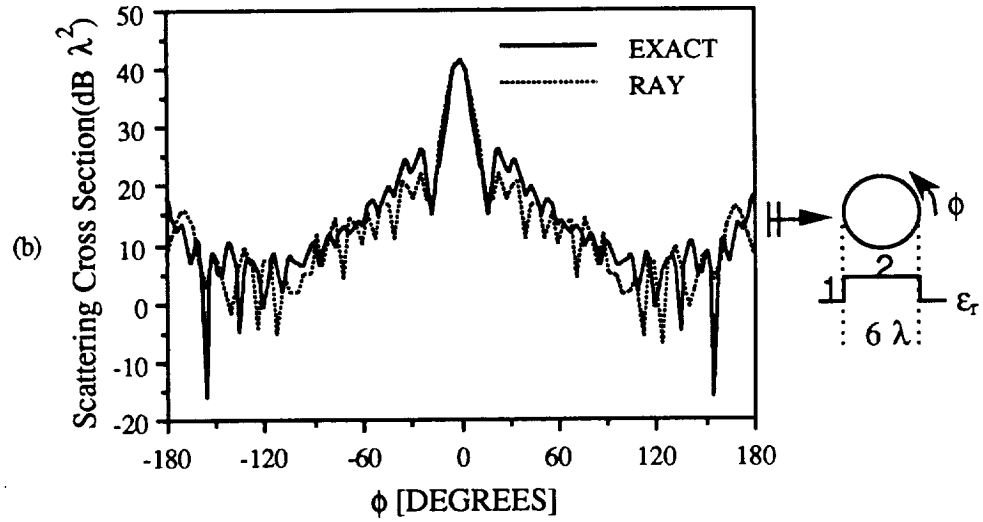
(b)
Scattering Cross Section(dB λ²)
EXACT
RAY
φ [DEGREES]
φ
2
1
6 λ
εr

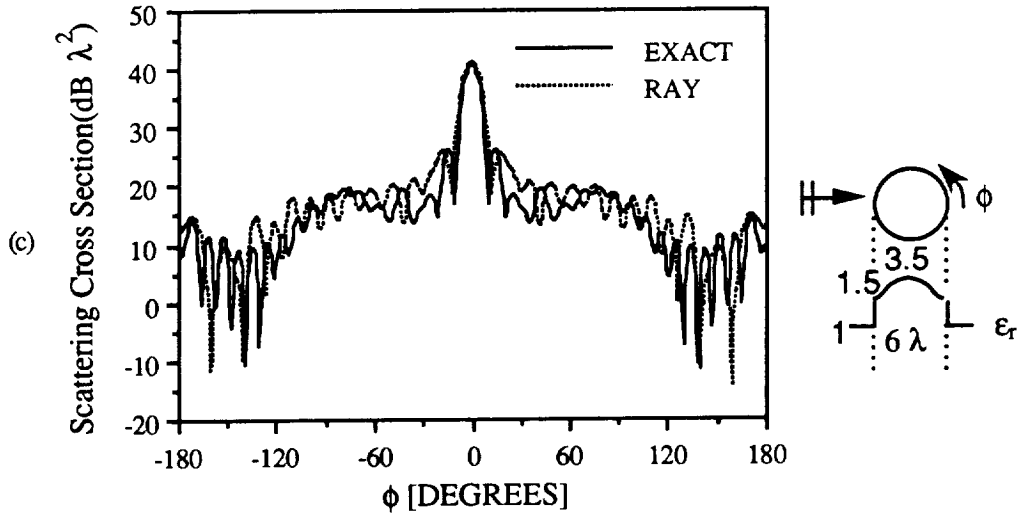
(c)
Scattering Cross Section(dB λ²)
EXACT
RAY
φ [DEGREES]
φ
3.5
1.5
1
6 λ
εr